Jordan Journal of

PHYSICS

An International Peer-Reviewed Research Journal

Volume 5, No. 2, 2012, 1433 H

Jordan Journal of Physics (*JJP*): An International Peer-Reviewed Research Journal established by the Higher Research Committee, Ministry of Higher Education & Scientific Research, Jordan, and published quarterly by the Deanship of Research & Graduate Studies, Yarmouk University, Irbid, Jordan.

Manuscripts should be submitted to:

Prof. Ibrahim O. Abu Al-Jarayesh
Editor-in-Chief, Jordan Journal of Physics
Deanship of Research and Graduate Studies
Yarmouk University-Irbid-Jordan
Tel. 00 962 2 7211111 Ext. 2075
E-mail: *jjp@yu.edu.jo*
Website: *http://Journals.yu.edu.jo/jjp*

Jordan Journal of
PHYSICS
An International Peer-Reviewed Research Journal

Volume 5, No. 2, 2012, 1433 H

INTERNATIONAL ADVISORY BOARD

Prof. Dr. Ahmad Saleh
Department of Physics, Yarmouk University, Irbid, Jordan.
salema@yu.edu.jo

Prof. Dr. Aurore Savoy-Navarro
LPNHE Universite de Paris 6/IN2P3-CNRS, Tour 33, RdC 4, Place Jussieu, F 75252, Paris Cedex 05, France.
auore@lpnhep.in2p3.fr

Prof. Dr. Bernard Barbara
Laboratoire Louis Neel, Salle/Room: D 108, 25, Avenue des Martyrs BP 166, 38042-Grenoble Cedex 9, France.
Barbara@grenoble.cnrs.fr

Prof. Dr. Bruno Guiderdoni
Observatoire Astronomique de Lyon, g, avenue Ch. Antre-F-69561, Saint Genis Laval Cedex, France.
Bruno.guiderdoni@olos.univ-lyon1.fr

Prof. Dr. Buford Price
Physics Department, University of California, Berkeley, CA 94720, U. S. A.
bprice@berkeley.edu

Prof. Dr. Colin Cough
School of Physics and Astronomy, University of Birmingham, B15 2TT, U. K.
c.gough@bham.ac.uk

Prof. Dr. Desmond Cook
Department of Physics, Condensed Matter and Materials Physics Research Group, Old Dominion University, Norfolk, Virginia 23529, U. S. A.
Dcook@physics.odu.edu

Prof. Dr. Evgeny Sheshin
MIPT, Institutskij per. 9, Dogoprudnyi 141700, Russia.
sheshin@lafeet.mipt.ru

Prof. Dr. Hans Ott
Laboratorium Fuer Festkorperphysik, ETH Honggerberg, CH-8093 Zurich, Switzerland.
ott@solid.phys.ethz.ch

Prof. Dr. Herwig Schopper
President SESAME Council, Chairman Scientific Board UNESCO IBSP Programme, CERN, 1211 Geneva, Switzerland.
Herwig.Schopper@cern.ch

Prof. Dr. Humam Ghassib
Department of Physics, Jordan University, Amman, Jordan.
humam@atf.org.jo

Prof. Dr. Ingo Hofmann
GSI Darmstadt, Planckstr. 1, 64291, Darmstadt, Germany.
i.hofmann@gsi.de

Prof. Dr. Jozef Lipka
Department of Nuclear Physics and Technology, Slovak University of Technology, Bratislava, llkovicova 3, 812 19 Bratislava, Slovakia.
Lipka@elf.stuba.sk

Prof. Dr. Khalid Touqan
Chairman of Jordan Atomic Energy Commission, Amman, Jordan.

Prof. Dr. Mark J. Hagmann
Desert Electronics Research Corporation, 762 Lacey Way, North Salt Lake 84064, Utah, U. S. A.
MHagmann@NewPathResearch.Com.

Prof. Dr. Nasr Zubeidey
President*: Al-Zaytoonah University of Jordan, Amman, Jordan.*
President@alzaytoonah.edu.jo

Prof. Dr. Patrick Roudeau
Laboratoire de I'Accelerateur, Lineaire (LAL), Universite Paris-Sud 11, Batiment 200, 91898 Orsay Cedex, France.
roudeau@mail.cern.ch

Prof. Dr. Paul Chu
Department of Physics, University of Houston, Houston, Texas 77204-5005, U. S. A.
Ching-Wu.Chu@mail.uh.edu

Prof. Dr. Peter Dowben
Nebraska Center for Materials and Nanoscience, Department of Physics and Astronomy, 255 Behlen Laboratory (10th and R Streets), 116 Brace Lab., P. O. Box 880111, Lincoln, NE 68588-0111, U. S. A.
pdowben@unl.edu

Prof. Dr. Peter Mulser
Instiute fuer Physik, T.U. Darmstadt, Hochschulstr. 4a, 64289 Darmstadt, Germany.
Peter.mulser@physik.tu-darmstadt.de

Prof. Dr. Rasheed Azzam
Department of Electrical Engineering, University of New Orleans New Orleans, Louisiana 70148, U. S. A.
razzam@uno.edu

Dr. Richard G. Forbes
University of Surrey, FEPS (X1), Guildford, Surrey GU2 7XH, U. K.
R.Forbes@surrey.ac.uk

Prof. Dr. Roy Chantrell
Physics Department, York University, York, YO10 5DD, U. K.
Rc502@york.ac.uk

Prof. Dr. Shawqi Al-Dallal
Department of Physics, Faculty of Science, University of Bahrain, Manamah, Kingdom of Bahrain.

Prof. Dr. Susamu Taketomi
Matsumoto Yushi-Seiyaku Co. Ltd., Shibukawa-Cho, Yao City, Osaka 581-0075, Japan.
staketomi@hotmail.com

Prof. Dr. Wolfgang Nolting
Institute of Physics / Chair: Solid State Theory, Humboldt-University at Berlin, Newtonstr. 15 D-12489 Berlin, Germany
Wolfgang.nolting@physik.hu-berlin.de

The Hashemite Kingdom of Jordan

Yarmouk University

Jordan Journal of
PHYSICS

An International Peer-Reviewed Research Journal

Volume 5, No. 2, 2012, 1433 H

Instructions to Authors

Instructions to authors concerning manuscript organization and format apply to hardcopy submission by mail, and also to electronic online submission via the Journal homepage website (http://jjp.yu.edu.jo).

Manuscript Submission

1- **Hardcopy**: The original and three copies of the manuscript, together with a covering letter from the corresponding author, should be submitted to the Editor-in-Chief:

Professor Ibrahim O. Abu Al-Jarayesh
Editor-in-Chief, Jordan Journal of Physics
Deanship of Scientific Research and Graduate Studies
Yarmouk University, Irbid, Jordan.
Tel: 00962-2-7211111, Ext. 2075
Fax: 00962-2-7211121
E-mail: jjp@yu.edu.jo

2- **Online**: Follow the instructions at the journal homepage website.

Original *Research Articles*, *Communications* and *Technical Notes* are subject to critical review by minimum of two competent referees. Authors are encouraged to suggest names of competent reviewers. *Feature Articles* in active Physics research fields, in which the author's own contribution and its relationship to other work in the field constitute the main body of the article, appear as a result of an invitation from the Editorial Board, and will be so designated. The author of a *Feature Article* will be asked to provide a clear, concise and critical status report of the field as an introduction to the article. *Review Articles* on active and rapidly changing Physics research fields will also be published. Authors of *Review Articles* are encouraged to submit two-page proposals to the Editor-in-Chief for approval. Manuscripts submitted in *Arabic* should be accompanied by an Abstract and Keywords in English.

Organization of the Manuscript

Manuscripts should be typed double spaced on one side of A4 sheets (21.6 x 27.9 cm) with 3.71 cm margins, using Microsoft Word 2000 or a later version thereof. The author should adhere to the following order of presentation: Article Title, Author(s), Full Address and E-mail, Abstract, PACS and Keywords, Main Text, Acknowledgment. Only the first letters of words in the Title, Headings and Subheadings are capitalized. Headings should be in **bold** while subheadings in *italic* fonts.

Title Page: Includes the title of the article, authors' first names, middle initials and surnames and affiliations. The affiliation should comprise the department, institution (university or company), city, zip code and state and should be typed as a footnote to the author's name. The name and complete mailing address, telephone and fax numbers, and e-mail address of the author responsible for correspondence (designated with an asterisk) should also be included for official use. The title should be carefully, concisely and clearly constructed to highlight the emphasis and content of the manuscript, which is very important for information retrieval.

Abstract: A one paragraph abstract not exceeding 200 words is required, which should be arranged to highlight the purpose, methods used, results and major findings**.**

Keywords: A list of 4-6 keywords, which expresses the precise content of the manuscript for indexing purposes, should follow the abstract.

PACS: Authors should supply one or more relevant PACS-2006 classification codes, (available at http://www.aip.org/pacs/pacs06/pacs06-toc.html)

Introduction: Should present the purpose of the submitted work and its relationship to earlier work in the field, but it should not be an extensive review of the literature (e.g., should not exceed 1 ½ typed pages).

Experimental Methods: Should be sufficiently informative to allow competent reproduction of the experimental procedures presented; yet concise enough not to be repetitive of earlier published procedures.

Results: should present the results clearly and concisely.

Discussion: Should be concise and focus on the interpretation of the results.

Conclusion: Should be a brief account of the major findings of the study not exceeding one typed page.

Acknowledgments: Including those for grant and financial support if any, should be typed in one paragraph directly preceding the References.

References: References should be typed double spaced and numbered sequentially in the order in which they are cited in the text. References should be cited in the text by the appropriate Arabic numerals, enclosed in square brackets. Titles of journals are abbreviated according to list of scientific periodicals. The style and punctuation should conform to the following examples:

1. Journal Article:

a) Heisenberg, W., Z. Phys. 49 (1928) 619.
b) Bednorz, J. G. and Müller, K. A., Z. Phys. B64 (1986) 189
c) Bardeen, J., Cooper, L.N. and Schrieffer, J. R., Phys. Rev. 106 (1957) 162.
d) Asad, J. H., Hijjawi, R. S., Sakaji, A. and Khalifeh, J. M., Int. J. Theor. Phys. 44(4) (2005), 3977.

2. Books with Authors, but no Editors:

a) Kittel, C., "Introduction to Solid State Physics", 8th Ed. (John Wiley and Sons, New York, 2005), chapter 16.
b) Chikazumi, S., C. D. Graham, JR, "Physics of Ferromagnetism", 2nd Ed. (Oxford University Press, Oxford, 1997).

3. Books with Authors and Editors:

a) Allen, P. B. "Dynamical Properties of Solids", Ed. (1), G. K. Horton and A. A. Maradudin (North-Holland, Amsterdam, 1980), p137.
b) Chantrell, R. W. and O'Grady, K., "Magnetic Properities of Fine Particles" Eds. J. L. Dormann and D. Fiorani (North-Holland, Amsterdam, 1992), p103.

4. Technical Report:

Purcell, J. "The Superconducting Magnet System for the 12-Foot Bubble Chamber", report ANL/HEP6813, Argonne Natt. Lab., Argonne, III, (1968).

5. Patent:

Bigham, C. B., Schneider, H. R., US patent 3 925 676 (1975).

6. Thesis:

Mahmood, S. H., Ph.D. Thesis, Michigan State University, (1986), USA (Unpublished).

7. Conference or Symposium Proceedings:

Blandin, A. and Lederer, P. Proc. Intern. Conf. on Magnetism, Nottingham (1964), P.71.

8. Internet Source:

Should include authors' names (if any), title, internet website, URL, and date of access.

9. Prepublication online articles (already accepted for publication):

Should include authors' names (if any), title of digital database, database website, URL, and date of access.

For other types of referenced works, provide sufficient information to enable readers to access them.

Tables: Tables should be numbered with Arabic numerals and referred to by number in the Text (e.g., Table 1). Each table should be typed on a separate page with the legend above the table, while explanatory footnotes, which are indicated by superscript lowercase letters, should be typed below the table.

Illustrations: Figures, drawings, diagrams, charts and photographs are to be numbered in a consecutive series of Arabic numerals in the order in which they are cited in the text. Computer-generated illustrations and good-quality digital photographic prints are accepted. They should be black and white originals (not photocopies) provided on separate pages and identified with their corresponding numbers. Actual size graphics should be provided, which need no further manipulation, with lettering (Arial or Helvetica) not smaller than 8 points, lines no thinner than 0.5 point, and each of uniform density. All colors should be removed from graphics except for those graphics to be considered for publication in color. If graphics are to be submitted digitally, they should conform to the following minimum resolution requirements: 1200 dpi for black and white line art, 600 dpi for grayscale art, and 300 dpi for color art. All graphic files must be saved as TIFF images, and all illustrations must be submitted in the actual size at which they should appear in the journal. Note that good quality hardcopy original illustrations are required for both online and mail submissions of manuscripts.

Text Footnotes: The use of text footnotes is to be avoided. When their use is absolutely necessary, they should be typed at the bottom of the page to which they refer, and should be cited in the text by a superscript asterisk or multiples thereof. Place a line above the footnote, so that it is set off from the text.

Supplementary Material: Authors are encouraged to provide all supplementary materials that may facilitate the review process, including any detailed mathematical derivations that may not appear in whole in the manuscript.

Revised Manuscript and Computer Disks

Following the acceptance of a manuscript for publication and the incorporation of all required revisions, authors should submit an original and one more copy of the final disk containing the complete manuscript typed double spaced in Microsoft Word for Windows 2000 or a later version thereof. All graphic files must be saved as PDF, JPG, or TIFF images.

Allen, P.B., "…………….", in: Horton, G.K., and Muradudin, A. A., (eds.), "Dynamical…….", (North……..), pp….

Reprints

Twenty (20) reprints free of charge are provided to the corresponding author. For orders of more reprints, a reprint order form and prices will be sent with the article proofs, which should be returned directly to the Editor for processing.

Copyright

Submission is an admission by the authors that the manuscript has neither been previously published nor is being considered for publication elsewhere. A statement transferring copyright from the authors to Yarmouk University is required before the manuscript can be accepted for publication. The necessary form for such transfer is supplied by the Editor-in-Chief. Reproduction of any part of the contents of a published work is forbidden without a written permission by the Editor-in-Chief.

Disclaimer

Opinions expressed in this Journal are those of the authors and neither necessarily reflects the opinions of the Editorial Board or the University, nor the policy of the Higher Scientific Research Committee or the Ministry of Higher Education and Scientific Research. The publisher shoulders no responsibility or liability whatsoever for the use or misuse of the information published by JJP.

Indexing

JJP is currently applying for indexing and abstracting to all related International Services.

Jordan Journal of
PHYSICS
An International Peer-Reviewed Research Journal

Volume 5, No. 2, 2012, 1433 H

Table of Contents:

Review Article — Pages

English Articles — Pages

Arabic Article — Pages

Volume 5, Number 2, 2012. pp. 53-66

Jordan Journal of Physics

REVIEW ARTICLE

Corrosion Products Study of VVER-440 Secondary Circuit

V. Slugen, J. Lipka, J. Dekan and I. Toth

Department of Nuclear Physics and Technology, Slovak University of Technology Bratislava, Ilkovicova 3, 812 19 Bratislava, Slovakia.

Received on: 22/2/2011; Accepted on: 29/3/2011

Abstract: The variability of the properties and the composition of the corrosion products of the stainless CrNi and mild steels in dependence on the conditions (temperature, acidity, … etc.) are of such range that, in practice, it is impossible to determine the properties of the corrosion products for an actual case from the theoretical data only. Since the decontamination processes for the materials of the water-cooled reactor (VVER-440) secondary circuits are in the progress of development, it is necessary to draw the needed information by the measurement and analysis of the real specimens. The corrosion layers were separated by scraping the rust off the surface and the powder samples were studied by transmission Mössbauer spectroscopy. It should be noted that the gamma spectroscopic measurements give no evidence of the presence of low-energy gamma radiation emitted from the samples. The ^{57}Co in Rh matrix was used as the radioactive Mössbauer source. Measured spectra were fitted using NORMOS SITE program. According to the results obtained from Mössbauer spectra, it is possible to establish that the main component of secondary circuit's corrosion products is magnetite Fe_3O_4. Next components are hematite alfa-Fe_2O_3 and hydroxide akagenite beta-FeOOH, which is characterized by significant paramagnetic doublet in the middle of the spectra. The sextets corresponding to base materials (martenzite and austenite steels) were identified in all measured spectra. Corrosion distribution and phase composition in form of "corrosion maps" at steam generators as well as other secondary circuit components were created for VVER-440 nuclear power plant in Jaslovske Bohunice (Slovakia). Our study was focused on the ratio magnetite/hematite and ways for operational optimization.

Keywords: Corrosion; VVER; Mössbauer spectroscopy; NPP lifetime.

I. Introduction

Steam generators (SG) are generally among the most important components at all nuclear power plants (NPP) with close impact to safe and long-term operation. The Russian water cooled and water moderated reactors (VVER) are unique because of the horizontal position of SGs. There are several advantages (large amount of cooling water in case of loss of coolant accidents, good accessibility, large heat exchange surface, … etc) but also some disadvantages, which are important to take into account during the operation and maintenance. Material degradation and corrosion-erosion processes are serious risks for long-term reliable operation. In the period of about 10-15 year ago, the feed water pipelines were changed at all SGs in all 4 Bohunice units (V-1 and V-2, in total at 24 SGs). New design of this pipeline system was performed, too. Actually, it takes time to evaluate the changes.

The variability of the properties and the composition of the corrosion products of the stainless Cr-Ni and mild steels in dependence on the NPP operating conditions (temperature, acidity, … etc.) are of such range that, in practice, it is impossible to determine the properties of the corrosion products for an actual

Corresponding Author: J. Lipka **Email**: jozef.lipka@stuba.sk

case from the theoretical data only. Since the decontamination processes for the materials of the VVER-440 secondary circuits are in the progress of development, it is necessary to draw the needed information by the measurement and analysis of the real specimens [1].

II. Mössbauer spectroscopy advantages

The phenomenon of the emission and absorption of a γ-ray photon without energy losses due to recoil of the nucleus and without thermal broadening is known as the Mössbauer effect. Its unique feature is in the production of monochromatic electromagnetic radiation with a very narrowly defined energy spectrum that allows resolving minute energy differences [2, 3].

Mössbauer spectroscopy (MS) is a powerful analytical technique because of its specificity for one single element and because of its extremely high sensitivity to changes in the atomic configuration in the near vicinity of the probe isotopes (in this case ^{57}Fe). MS measures hyperfine interactions and these provide valuable and often unique information about the magnetic and electronic state of the iron species, their chemical bonding to co-ordinating ligands, the local crystal symmetry at the iron sites, structural defects, lattice-dynamical properties, elastic stresses, … etc. [1, 4]. Hyperfine interactions include the electric monopole interaction, i.e., the isomer shift, the electric quadrupole interaction, i.e., the quadrupole splitting and the magnetic dipole or nuclear Zeeman interaction, i.e., hyperfine magnetic splitting. These interactions often enable detailed insight into the structural and magnetic environment of the Mössbauer isotope. Indeed, more than four decades after its discovery (1958), Mössbauer spectroscopy still continues to develop as a sophistic scientific technique and it is often the most effective way of characterizing the range of structures, phases and metastable states.

In general, a Mössbauer spectrum shows different components if the probe atoms are located at lattice positions, which are chemically or crystalographically unequivalent. From the parameters that characterize a particular Mössbauer sub-spectrum, it can, for instance, be established whether the corresponding probe atoms reside in sites which are not affected by structural lattice defects or whether they are located at defect-correlated positions. Each compound or phase, which contains iron, has typical parameters of its Mössabuer spectrum. It means that the method is suitable for quantitative as well as qualitative analysis. Mössbauer spectroscopy is non-destructive and requires relative small quantities of samples (~100 mg) [5-8].

Application of Mössbauer spectroscopy for precise analysis of phase composition of corrosion products was performed from selected areas of primary and secondary circuit and SG. Interpretation of measured results, having in vision the long-term operation and nuclear safety, is neither easy nor straightforward. Thank our more than 25 years of experience in this area, there exists already a base for the relevant evaluation of results. Optimization of operating chemical regimes as well as regimes at decontamination and passivation seems to be an excellent output.

All steam generators at four VVER-440 units in Bohunice were gradually changed. The basic design from 1977 was improved after 1994 by a new feed water pipeline system. There was also a change in the type of steel of these pipelines. Instead of conventional carbon steel, the austenite steel was used in distribution boxes as well as feed water pipelines.

All components in the Bohunice innovated feed water pipeline system were made of austenitic steel according to Czechoslovak norm ČSN, class 17. Advantages of the new construction are not only higher resistance against corrosion, but also much more comfortable visual inspection. Innovations can be seen in Figs. 3-5. Actually, experiences from the past 10 years after upgrade were evaluated.

III. Experimental

For the experimental measurements, several specimens containing corrosion products were taken from different parts of all of the 4 NPP Bohunice units. In the first step, the corrosion process at the steam generators was studied. The corrosion layers were separated by scraping the rust off the surface and the powder samples were studied by transmission Mössbauer spectroscopy. It should be noted that the gamma spectroscopic measurements give no evidence of the presence of low-energy gamma radiation emitted from the samples. Later, the corrosion products were collected also from different parts of secondary circuit components and several filter deposits were analyzed as well.

The room temperature Mössabuer study was performed at two different steam generator materials using conventional transmission Mössbauer spectrometer with the source ^{57}Co in Rh matrix. Spectra were fitted using NORMOS program.

The original STN 12022 material used at the 4th (SG46) over 13 years was compared to STN 17247 steel used at the 3rd unit (SG35) for about 5 years (1994-1998). The chemical composition of both materials is shown in Table 1.

Samples of corrosion products scrapped from different parts of the steam generators SG 35 and SG46 were analyzed. The scrapped corrosion particles were homogenized by granulation and sieved in the wire of 50μm.

TABLE 1. Chemical composition of the investigated base materials.

Steam generator	Type of the steel	Chemical composition [weight %]							
		C	Mn	Si	Cr	Ni	Ti	P	Cu
SG35	STN 17247	max. 0,08	max. 0,08	max. 1,0	17,0 -19,0	9,5 - 12,0	min. 5x%C	max. 0,045	-
SG46	STN 12022 (GOST 20K)	0,16-0,24	0,35-0,65	0,15-0,30	max. 0,25	max. 0,25	-	0,04	max. 0,3

IV. Results from Mössbauer spectroscopy analyses

The advanced evaluation of phase analyses of corrosion products from different parts of VVER-440 steam generators via Mössbauer spectroscopy is our active and unique contribution in this area. The scientific works go over 25 years. The first period (mostly 80-ies) was important for proper Mössbauer technique improving. The benefit from this period is mostly in experience collection, optimization of measurement condition and evaluation programs improvement [5]. Unfortunately, not all specimens were well defined. Having in mind also different levels of techniques and evaluation procedures, it would be not serious to compare results from this period to results obtained from measurements after 1998.

IV.1. Comparison of the phase composition of corrosion products taken from the NPP Bohunice before and after changes in the feed water pipeline system, 1998-1999

In the period 1998-1999, we focused our study on the comparison of the phase composition of corrosion products taken from the NPP Bohunice before and after changes in the feed water pipeline system.

Schematic drawings of VVER steam generators (SGs) with indicated places of scrapped corrosion specimens are presented in Fig.1.

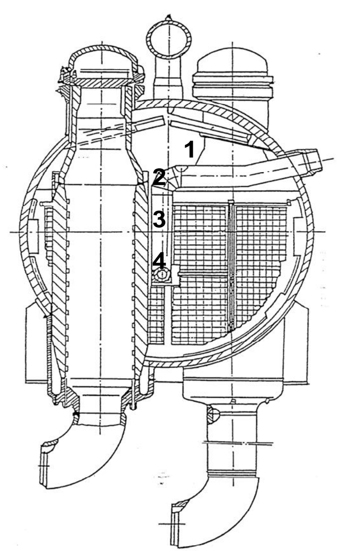

FIG. 1. Cross-section of SG46 (Numbers indicate the places, where the specimens were scrapped).

Serious damages were observed in the region of T-junction (position 4 in Fig.1) as well as of pipe-collector and outlet nozzles on many VVER440 SGs after approximately ten years of operation [9, 17]. Therefore, the former feed water-distributing system has been replaced by an advanced feed water distributing system of EBO design at SGs of NPP Jaslovske Bohunice [18, 19]. The advanced system consists of a V-shaped junction connected to the left and the right part water distributing chambers both located above the tube bundle and few feed water boxes with water ejectors inserted into the tube bundle and connected to the distributing chamber by distributing pipelines.

After five year operation in the SG 35 in the NPP outage one feed water box and the corresponding distributing pipelines were replaced by new ones with the aim to analyze their overall stage and corrosion products on the walls. For comparison, some parts of the former feed water distributing system from the SG 46 were cut out and analyzed.

More than 50 specimens were collected from the NPP Bohunice secondary circuit in 1998-2000. The investigation was focused mainly on the corrosion process going on in steam generators SG35 with new design and SG46 with old design. Nevertheless, additional measurements performed on the corrosion products from SG31 and SG32 confirmed that the corrosion process in all 6 steam generators of one reactor unit is the same and the corrosion layers are on the same places altogether identical.

All measured specimens comprise iron in magnetic and many times also in paramagnetic phases. Magnetic phases consist in form of nearly stoichiometric magnetite (γ-Fe_3O_4), hematite (α-Fe_2O_3), and in some cases also iron carbides. The paramagnetic fractions are presented in Mössbauer spectra by doublets and singlets. Its parameters are close to hydro-oxide (FeOOH) parameters or to parameters of small so-called superparamagnetic particles of iron oxides (hydroxides) with the mean diameter of about 10 nm (see Table 2 and Table 3).

MS confirmed its excellent ability to identify steel specimens phase composition in spite of their sawdust form and relative small amount (~ 100 mg). Our experiences with such measurements were published in [16, 20-22]. MS confirmed an austenitic structure of STN 17247 steel and ferrite structure of STN 12022 steel.

Results confirmed that during operation time a very weak oxidation surrounding was in the observed steam generator SG35 after 5 years of operation time and the corrosion specimens were fully without base material particles.

Magnetite was identified as dominant component in all studied specimens (see Table 2). Mössbauer spectrum of the steam generators (both SG35 and SG46) surface layer is the superposition of two sextets with hyperfine magnetic field H_{efA} = 49,4T and H_{efB} = 45.8T. Sextet H_{efA} corresponds to the Fe^{3+} ions in tetrahedral (A) sites and sextet H_{efB} corresponds to Fe^{2+} and Fe^{3+} ions in octahedral (B) sites in magnetite spinel structure (Fe_3O_4).

TABLE 2. MS parameters of corrosion products taken from the steam generator SG35.

	Magnetite					Doublet			Singlet	
Sample	H_A	A_{rel}	H_B	A_{rel}	r_{AB}	IS	QS	A_{rel}	IS	A_{rel}
	(T)	(%)	(T)	(%)	(a.u.)	(mm/s)	(mm/s)	(%)	(mm/s)	(%)
L754	49.0	35.0	45.9	65.0	0.538					
L755	49.0	35.3	45.9	64.7	0.546					
L757	49.0	34.8	45.9	65.2	0.534					
L758	49.0	34.1	45.9	62.3	0.547				-0.20	3.6
L789	49.0	34.4	46.0	65.6	0.535					
L790	49.0	34.9	46.0	64.3	0.543				-0.18	0.8
L759	49.0	35.4	45.9	63.9	0.534				-0.20	0.7
L777	49.0	35.0	45.9	65.0	0.538					
L786	49.0	35.2	46.0	64.8	0.545					
L787	49.1	36.5	46.0	56.1	0.651	0.22	0.67	2.0	-0.20	5.4
L760	49.0	34.1	45.9	64.3	0.530				-0.17	1.6
L761	49.0	35.0	45.9	63.9	0.547				-0.23	1.1
L762	49.1	34.8	46.0	56.4	0.617				-0.20	8.8
L779	49.0	33.4	45.9	62.9	0.531				0.10	3.7
Accuracy	±0,1	±0,5	±0,1	±0,5		±0,04	±0,04	±0,5	±0,04	±0,5

In contrast to magnetite, whose spectrum is characterized by two sextets, the hematite phase present in the powders produces one sextet. The relatively narrow line width (Γ) of the α-Fe_2O_3 (mainly 0, 24 ÷ 0, 26 mm/s) indicates the presence of a well-crystallized phase with few, if any, substitutions of other elements for Fe. However, in some spectra (mainly from filter deposits studied later) both the lower hyperfine field and the larger width (about 0.33 – 0.34 mm/s) could indicate a poorer crystallinity and/or a higher degree of substitution. These findings are in good agreement with those obtained by E. De Grave [23].

For the ideal stoichiometric Fe_3O_4, the quantity r_{AB} (ratio between A and B sub-component areas) is equal to 0.535. In the case that magnetite is the dominant (sole) phase in the specimen, the deviation from the ideal value of r_{AB} is minimal (see Table 3). Significant deviations could be explained by a small degree of oxidation of magnetite, resulting in the presence of vacancies or substitution by non/magnetic irons in the octahedral sub-lattice. Slight substitution of other elements (Mg, Ni, Cu, …) for Fe in the magnetite lattice is not unlikely, and this has a similar effect on the A- to B-site area ratio. Therefore, it is not feasible to conclude anything quantitatively about the degree of oxidation. Qualitatively, it can be inferred that this degree must be very low.

During visual inspection of the removed feed water dispersion box (1998, Fig. 2.), 2 disturbing undefined metallic particles, fixed in one of the outlet nozzles, were found. Both were homogenized and analyzed by MS. It has been shown that these high-corroded parts (“loose parts” found in the outlet nozzle of the ejector) originate not from the 17247 steel but high probably from GOST 20K steel (probably some particles from the corrosion deposit from the bottom part of the steam generator moved by flow and ejection effect into the nozzle).

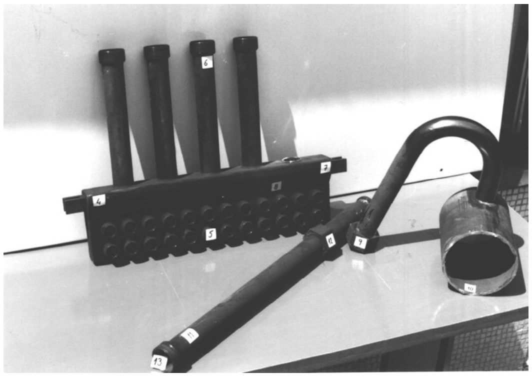

FIG. 2. Position of corrosion product scraps from the feed water dispersion box (SG35).

TABLE 3. MS parameters of corrosion products taken from the steam generator SG46.

CODE	Hematite		Magnetite				Base material				Doublet 1		Doublet 2	
	H1	A_{rel}	H_A	A_{rel}	H_B	A_{rel}	H4	A_{rel}	H5	A_{rel}	IS1	A_{rel}	IS2	A_{rel}
	(T)	%	(T)	%	(T)	%	(T)	%	(T)	%	(mm/s)	%	(mm/s	%
M005			49.0	35.4	45.8	64.6								
M006			49.1	36.5	45.9	63.5								
M007	50.0	16.9	49.2	25.6	45.8	38.2	33.0	1.6					0.84	17.7
M008			49.0	35.6	45.9	64.1								
M009	51.5	13.4	49.1	32.1	45.9	54.5								
M010			49.1	36.5	45.8	63.5								
M012	51.5	12.5	49.2	31.9	46.0	55.6								
M013			48.8	25.3	45.7	40.5	33.0	30.2	30.8	4.0				
M014			49.0	9.9	45.8	13.6	33.0	66.6	30.7	9.9				
M015			48.5	6.0	45.6	8.6	33.0	73.1	30.6	12.3				
Accuracy	±0,1	±0,5	±0,1	±0,5	±0,1	±0,5	±0,1	±0,5	±0,1	±0,5	±0,1	±0,5	±0,1	±0,5

Mössbauer measurements on the corrosion specimens scrapped from different positions of the feed water distributing system (see Fig.10) have shown that the outside layer consists exclusively from magnetite but the inside layer contains also hematite. Its amount decreases in successive steps towards into the steam generator. The origin of this result is probably the fact that outside the system there is boiling water at a temperature of approximately 260 °C with higher salt concentration and inside there is the feed water at a temperature up to 225 °C. Changes in the inside temperature in the region (158-225 °C) can occur in dependence on the operation regime of high-pressure pumps in the NPP secondary circuit.

The most corroded areas of the former feed water distributing system are welds in the T-junction (see Fig. 3). Due to dynamic effects of the feed water flow with local dynamic overpressures of 20 to 30 kPa or local dynamic forces up to 1000 N (in the water at the pressure of about 4,4 MPa) on the inner pipe wall in the region of T-junction, the content of corrosion products was reduced and moved into the whole secondary circuit. Particles of the feed water tube of SG46 base material were identified also in sediments.

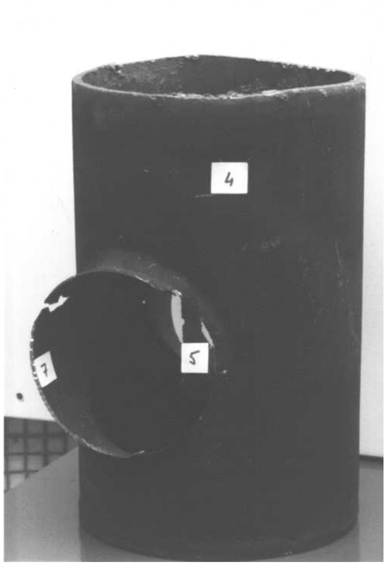

FIG. 3. Position of corrosion product scraps from the feed water dispersion tube (SG46).

IV.2. Results from visual inspection of heterogenic weld at SG16 from April 2002

In the period 2002-2003, we focused on the "Phase analyses of corrosion induced damage of feed water pipelines of SG 16 near the heterogenic weld". In the frame of this study, visual inspections as well as original "in situ" specimens scrapping were performed. Conclusions from visual inspections (performed at 19.4.2002 and 29.4.2002 at SG16) were as follows:

SG16 was dried under the level of primary pipelines bundle. The whole SG was decontaminated as there were lead plates on the upper part of the pipelines bundle due to maximal shielding effect. During the visual inspection of SG16 internal surface as well as hot and cold collectors (after 23 years of operation), no defects or cracks were identified. SG16 was in excellent status with minimal thickness of corrosion layer or other deposits. For comparison to our previous experiences from visual inspections from 1998, SG16 was in better condition than SG35 or SG46 (14 and 13 years in operation, respectively). Beside this, the radiation situation after decommissioning procedures was twice better.

Visual inspection on 29.4.2002 was focused on heterogenic weld, which connects the feed water pipeline from carbon steel (GOST 20K) to the new feed water pipeline system designed from austenitic steel (CSN17248). Several specimens were taken for MS analysis from the weld as well as the surrounding area in the from of powder or small particles (samples description is in Table 4). The heterogenic weld was well polished.

After visual inspection, the evaluation of corrosion phase composition of specimens close to heterogenic weld was performed. Places, where specimens were taken are shown in Fig. 4. Specimens description and MS results are summarized in Tables 4 and 5.

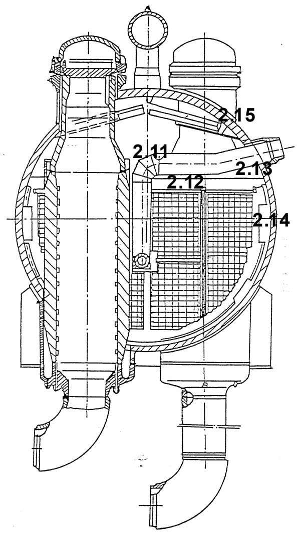

FIG. 4. SG16 cross-section with indicated places where specimens were taken.

TABLE 4. Specimens description.

Number of sample	Sample description
2.11	Heterogenic weld.
2.12	Feed water pipeline (GOST 20), 10 cm from the heterogenic weld.
2.13	Feed water pipeline (GOST 20), about 40 cm from the heterogenic weld, just close to the SG16 internal body surface.
2.14	Internal body surface, about 1 m under the place of feed water pipeline inlet.
2.15	Internal body surface, about 50 cm over the place of feed water pipeline inlet.

TABLE 5. Mössbauer spectra parameters.

	Haematite				Magnetite					
Sample	H_1 (T)	QS_1 (mm/s)	IS_1 (mm/s)	A_{rel1} (%)	H_2 (T)	IS_2 (mm/s)	A_{rel2} (%)	H_3 (T)	IS_3 (mm/s)	A_{rel3} (%)
2.11	51,9	-0,18	0,25	8,0	49,0	0,17	3,8	45,9	0,57	8,0
2.12	51,6	-0,21	0,26	75,9	49,0	0,16	9,1	45,8	0,56	14,1
2.13	51,6	-0,21	0,26	77,2	49,0	0,17	9,2	45,9	0,57	12,9
2.14	51,6	-0,21	0,26	41,1	49,0	0,16	22,0	45,8	0,55	36,9
2.15	51,8	-0,21	0,26	51,7	49,1	0,17	18,3	45,9	0,54	29,2
Accuracy	±0,1	±0,04	±0,04	±2	±0,1	±0,04	±0,1	±0,1	±0,04	±2

	Metallic iron			Doublet/singlet		
Sample	H_4 (T)	IS_4 (mm/s)	A_{rel4} (%)	QS_4 (mm/s)	IS_4 (mm/s)	A_{rel4} (%)
2.11	33,0	-0,11	12,8	-	-0,19	67,4
2.12	-	-	-	0,40	0,21	0,9
2.13	-	-	-	0,40	0,21	0,7
2.14	-	-	-	-	-	-
2.15	-	-	-	0,40	0,21	0,8

IV.3. Measurement of corrosion products at NPP Jaslovske Bohunice, 2007-2008

In 2007 – 2008, six samples for Mössbauer effect experiments collected from different parts of NPP Bohunice unit, were prepared by crushing to powder pieces (Table 5). These samples consist of corrosion products taken from the small coolant circuit of pumps (sample no. 3.1), deposits scraped from filters after filtration of SG - feed water during operation (sample no. 3.2), corrosion products taken from SG42 pipelines - low level (sample no. 3.3), mixture of corrosion products, ionex, sand taken from filter of condenser to TG 42 (sample no. 3.4), deposit from filters after refiltering 340 l of feed water of SG S3-09 during passivation on 27. and 28. 5. 08 (sample no. 3.5) and finally deposit from filters after refiltering 367 l of feed water of SG S4-09 during passivation on 27. and 28. 5. 08 (sample no. 3.6). All samples were measured at room temperature in transmission geometry using a $^{57}Co(Rh)$ source. Calibration was performed with α-Fe. Hyperfine parameters of the spectra including spectral area (A_{rel}), isomer shift (*IS*), quadrupole splitting (*QS*), as well as hyperfine magnetic field (B_{hf}), were refined using the CONFIT fitting software [24], the accuracy values in their determination are of ±0.5 % for relative area A_{rel}, ±0.04 mm/s for Isomer Shift and Quadrupole splitting and ±0.5 T for hyperfine field, correspondingly. Hyperfine parameters for the identified components (hematite, magnetite, goethite, lepidocrocite, feroxyhyte) are taken from [25].

All measured spectra contain iron in magnetic and many times also in paramagnetic phases. Magnetic phases contains iron in nonstoichiometric magnetite $Fe_{3-x}M_xO_4$, where M_x represents impurities and vacancies which substitute iron in octahedral (B) sites. Another magnetic fraction is hematite α-Fe_2O_3. In one sample also the magnetic hydroxide (goethite α-FeOOH) was identified.

Paramagnetic fractions are presented in the spectra by quadrupole doublets (QS). Their parameters are close to those of hydroxides; e.g. lepidocrocite γ –FeOOH or to small so-called superparamagnetic particles of iron oxides or hydroxides with the mean diameter of about 10 nm. It should be noted that there is no problem to distinguish among different magnetically ordered phases when they are present in a well crystallized form with low degree (or without) substitution. Both the substitution and the presence of small superparamagnetic particles make the situation more complicated [26]. In such cases, it is necessary to perform other supplementary measurements at different temperatures down to liquid nitrogen or liquid helium temperatures without and with an external magnetic field [27].

Mössbauer spectrum (Fig. 5) of sample no. 3.1 (corrosion products taken from small coolant circuit of pumps) consists of three magnetically split components, where the component with hyperfine field B_{hf} = 35.8 T was identified as goethite (α-FeOOH). Hyperfine parameters of the remaining two magnetically split components are assigned to A – sites and B – sites of magnetite (Fe_3O_4). One paramagnetic spectral component has appeared. According to water environment and pH [28], this component should be assigned to hydroxide (feroxyhyte δ-FeOOH).

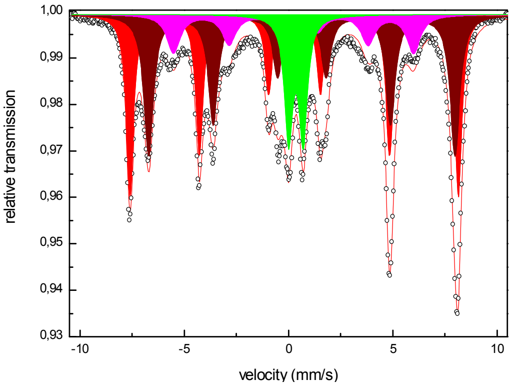

FIG. 5. Mössbauer spectrum of sample no. 3.1. A-site (red), B-site (dark red) magnetite, goethite (pink) and hydroxide (green) were identified.

Sample no. 3.2 (deposits scraped from filters after filtration of SG - feed water during operation) also consists of three magnetically split components, where two of them were assigned to magnetite (Fe_3O_4) as in previous spectra, and the remaining magnetically split component was identified as hematite (α-Fe_2O_3). Paramagnetic part of the spectra was formed by one doublet, which was hyperfine parameters assigned to hydroxide (lepidocrocite γ-FeOOH). The spectrum is shown in Fig. 6.

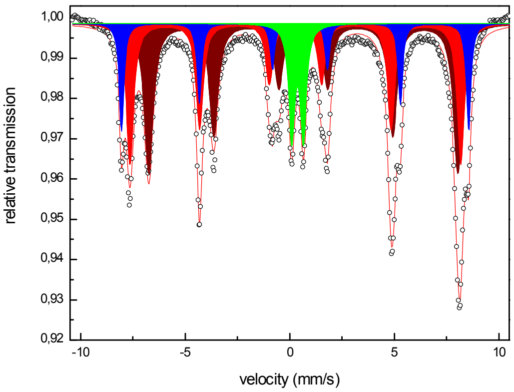

FIG. 6. Mössbauer spectrum of sample no.3. 2. A-site (red), B-site (dark red) magnetite, haematite (blue) and hydroxide (green) were identified.

The spectrum (Fig. 7) of sample no. 3.3 (corrosion products taken from SG42 pipelines - low level) consists only of two magnetically split components with hyperfine parameters assigned to A – sites and B – sites of nearly stoichiometric magnetite (Fe_3O_4) with a relative area ratio β = 1.85.

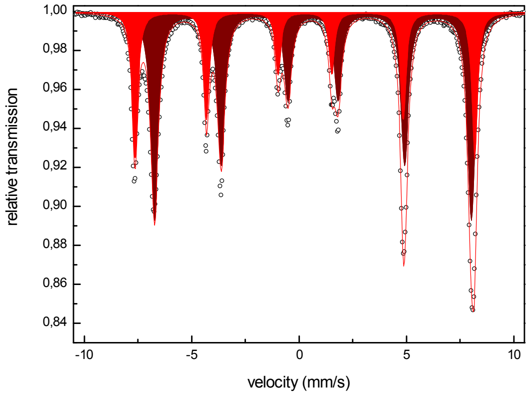

FIG. 7. Mössbauer spectrum of sample no. 3.3. A-site (red) and B-site (dark red) magnetite were identified.

Sample no. 3.4 (mixture of corrosion products, ionex, sand taken from filter of condenser to TG 42) also consists of one magnetically split component which corresponds to hematite (α-Fe_2O_3) and two magnetically split components which were assigned to magnetite (Fe_3O_4) as in previous spectra, and the remaining paramagnetic component was identified as hydroxide. Spectrum of sample no. 3.4 is shown in Fig. 8.

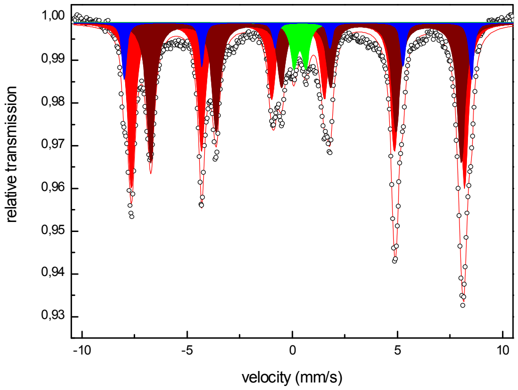

FIG.8. Mössbauer spectrum of sample no. 3.4. Haematite (blue), A-site (red), B-site (dark red) magnetite and hydroxide (green) were identified.

Both sample no. 3.5 (deposit from filters after refiltering 340 l of feed water of SG S3-09 during passivation on 27. and 28. 5. 08) and sample no. 3.6 (deposit from filters after refiltering 367 l of feed water of SG S4-09 during passivation on 27. and 28. 5. 08) consist of three magnetically split components, identified as hematite (α-Fe_2O_3) and magnetite (Fe_3O_4) and the remaining paramagnetic component in both spectra was assigned to hydroxide (lepidocrocite γ-FeOOH). Spectra of samples no. 3.5 and 3.6 are shown in Figs. 9 and 10.

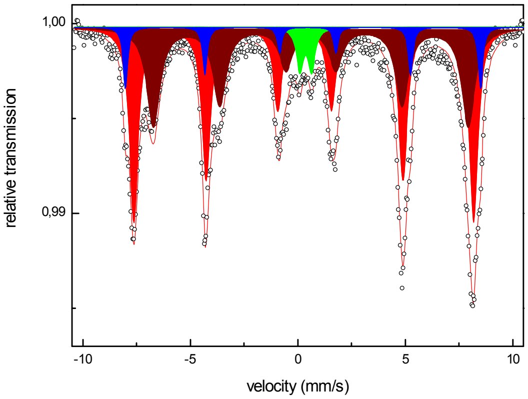

FIG. 9. Mössbauer spectrum of sample no.3.5. Haematite (blue), A-site (red), B-site (dark red) magnetite and hydroxide (green) were identified.

Based on the comparison of results from specimens 3.5 and 3.6, it can be concluded that longer passivation leads more to magnetite fraction (from 88% to 91%) in the corrosion products composition. As it was mentioned above, all hydroxides could be also small superparamagnetic particles.

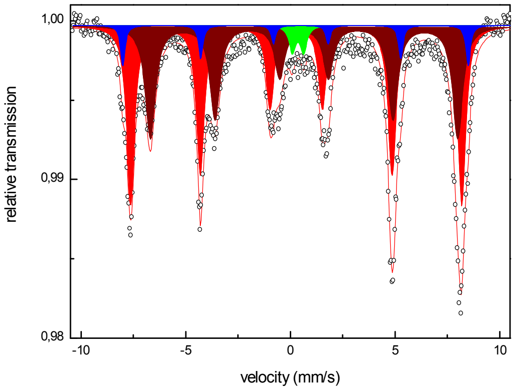

FIG. 10. Mössbauer spectrum of sample no. 3.6. Haematite (blue), A-site (red), B-site (dark red) magnetite and hydroxide (green) were identified.

The refined spectral parameters of individual components including spectral area (A_{rel}), isomer shift (*IS*), quadrupole splitting (*QS*), as well as hyperfine magnetic field (B_{hf}) are listed in Table 6 for room (300 K) temperature Mössbauer effect experiments. Hyperfine parameters for identified components (hematite, magnetite, goethite, lepidocrocite, feroxyhyte) are listed in [25].

Major fraction in all samples consists of magnetically ordered iron oxides, mainly magnetite (apart from samples no. 3.1 and 3.2, where also goethite and hematite appeared, respectively). Magnetite crystallizes in the cubic inverse spinel structure. The oxygen ions form a closed packed cubic structure with Fe ions localized in two different sites, octahedral and tetrahedral. The tetrahedral sites (A) are occupied by trivalent Fe ions. Tri - and divalent Fe ions occupying the octahedral sites (B) are randomly arranged at room temperature because of an electron hopping. At room temperature, when the electron hopping process is fast, the Mössbauer spectrum is characterized by two sextets. The one with the hyperfine magnetic field B_{hf} = 48.8 T and the isomer shift IS = 0.27 mm/s relative to α-Fe corresponds to the Fe^{3+} ions at the tetrahedral A - sites. The second one with B_{hf} = 45.7 T and IS = 0.65 mm/s is the $Fe^{2.5+}$ - like average signal from the cations at the octahedral B - sites. Fe^{2+} and Fe^{3+} are indistinguishable due to a fast electron transfer (electron hopping), which is faster (~1 ns) than the ^{57}Fe excited state lifetime (98 ns). The magnetite unit cell contains eight Fe^{3+} ions and eight Fe^{2+} and Fe^{3+} ions, 16 in total at the B - sites, therefore, the intensity ratio β = I(B)/I(A) of the two spectral components is a sensitive measure of stoichiometry. Assuming that the room temperature ratio of the recoil-free fractions fB/ fA for the B - and A - sites is 0.97 [29], the intensity ratio β for perfect stoichiometry should be 1.94. In non-stoichiometric magnetite, under an excess of oxygen, cation vacancies and substitutions at the B - sites are created. The vacancies screen the charge transfer and isolate the hopping process. For each vacancy, five Fe^{3+} ions in octahedral sites become trapped. In the Mössbauer spectrum, these trapped Fe^{3+} ions at the octahedral sites and Fe^{3+} ions at the tetrahedral sites are indistinguishable without applying an external magnetic field. Therefore, in the spectrum of non-stoichiometric magnetite, intensity transfer from the $Fe^{2.5+}$ to Fe^{3+}-like components is observed. Therefore, the intensity ratio β decreases markedly with the oxidation process, until the stoichiometry reaches the γ-Fe_2O_3 phase. It should be noted that in our samples the intensity ratio β is far from 1.94 (for perfect stoichiometry), it varies from 0.97 up to 1.85.

TABLE 6. Spectral parameters of individual components including spectral area (A_{rel}), isomer shift (IS), quadrupole splitting (QS), as well as hyperfine magnetic field (B_{hf}) for each sample with the corresponding components.

Sample	Components	Area [%]	Isomer shift [mm/s]	Quadrupole shift/splitting [mm/s]	Hyperfine field [T]
Sample no. 3.1 Small coolant circuit of pumps 17. 10. 2007	magnetite A-site	36.3	0.28	0.00	48.90
	magnetite B-site	37.2	0.64	0.00	45.60
	goethite	14.4	0.36	-0.25	35.80
	hydroxide	12.1	0.36	0.70	-
Sample no. 3.2. Deposites scraped from filters after filtration of SG - feed water during operation	hematite	15.8	0.38	-0.23	51.56
	magnetite A-site	32.6	0.28	0.00	49.14
	magnetite B-site	41.8	0.65	0.00	45.91
	hydroxide	9.7	0.38	0.56	-
Sample no. 3.3. SG42 pipelines - low level	magnetite A-site	34.6	0.28	0.00	49.14
	magnetite B-site	65.4	0.65	0.00	45.83
Sample no. 3.4. Mixture of corrosion products, ionex, sand taken from filter of condenser to TG 42	hematite	9.2	0.38	-0.22	51.29
	magnetite A-site	45.4	0.28	0.00	49.20
	magnetite B-site	40.7	0.66	0.00	45.87
	hydroxide	4.7	0.37	0.56	-
Sample no. 3.5. Deposit from filters after refiltering 340 l of feed water of SG S3-09 during pasivation 27. and 28. 5. 08	hematite	8.3	0.36	-0.22	51.33
	magnetite A-site	49.3	0.30	0.00	49.11
	magnetite B-site	38.5	0.61	0.00	45.51
	hydroxide	3.9	0.37	0.55	-
Sample no. 3.6. Deposit from filters after refiltering 367 l of feed water of SG S4-09 during pasivation 27. and 28. 5. 08	hematite	6.4	0.38	-0.25	51.26
	magnetite A-site	50.3	0.29	0.00	49.14
	magnetite B-site	40.7	0.66	0.00	45.61
	hydroxide	2.6	0.37	0.54	-

IV.4. Measurements of corrosion products from thermal loop in Nuclear Research Institute Řež, Czech Republic, 2010

Corrosion layers taken from testing pipelines of thermal loop in Nuclear Research Institute Řež (Czech Republic) were analyzed using Mössbauer spectroscopy. Thermal loop is used for chemical regimes evaluation of steam-water cycles and simulates the local environment of primary circuits of VVERs.

Corrosion layers from cut pieces of pipelines were scraped and powdered (Fig. 11.), then measured at room temperature in transmission geometry using a ^{57}Co(Rh) source. Calibration was performed with α-Fe. Hyperfine parameters of the spectra including spectral area (A_{rel}), isomer shift (*IS*), quadrupole splitting (*QS*), as well as hyperfine magnetic field (B_{hf}), were refined using the CONFIT fitting software [24], the accuracy values in their determination are of ±0.5 % for relative area A_{rel}, ±0.04 mm/s for isomer shift and Quadrupole splitting and ±0.5 T for hyperfine field, correspondingly.

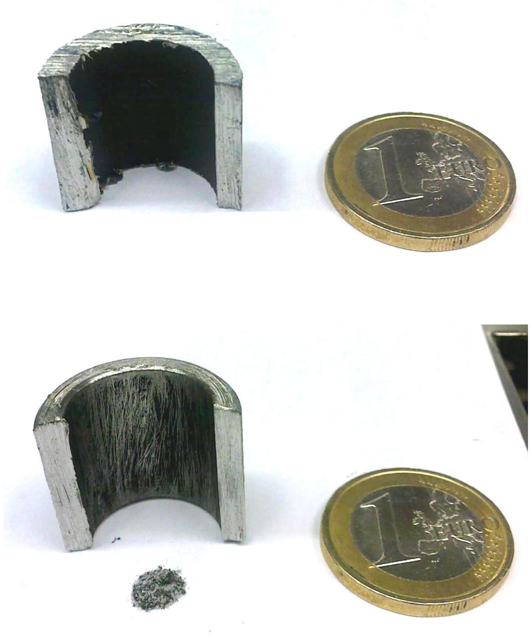

FIG. 11. Cut piece of pipeline (up), with scraped corrosion layer (bottom).

Measured spectra of scraped layers mostly consist of one singlet and magnetically split components with significant hyperfine field distribution. Singlet represents the austenitic fraction of base steel material of pipelines, magnetically split components with hyperfine field distribution were identified as martensitic fraction of base steel material. In some spectra, a small fraction of two magnetically ordered components has appeared. According to their spectral parameters, these components were assigned to magnetite A - and B - sites (Fig. 12).

From corrosion point of view, no other than magnetite component was revealed, which indicates a suitable local environment in the thermal loop of the research reactor in Řež.

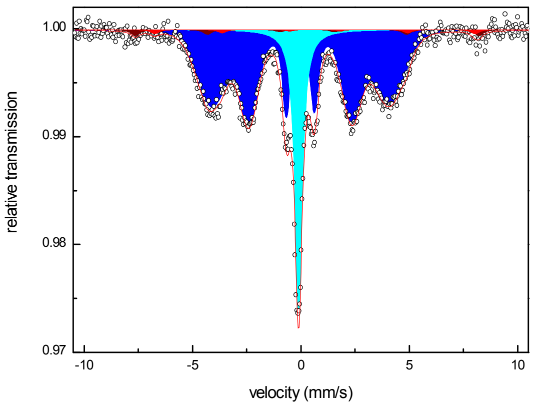

FIG. 12. MS spectrum of scraped corrosion layer. Austenitic fraction (light blue) and martensitic fraction (blue) came from base steel material, a small amount of magnetite (red, dark red) can also be seen.

V. Conclusions

Material degradation and corrosion are serious risks for long-term and reliable operation of NPP. The paper summarizes results of long-term measurements (1984-2008) of corrosion products phase composition using Mössbauer spectroscopy.

The first period (mostly results achieved in the 80-ies) was important for proper Mössbauer technique improving [5]. The benefit from this period came via experience collection, optimization of measurement conditions and evaluation programs improvement. Unfortunately, the specimens were not well defined, and having in mind also different levels of techniques and evaluation procedures, it would be not serious to compare results from this period to results obtained from measurements after 1998.

The replacement of STN 12022 steel (in Russian NPP marked as GOST 20K) used in the steam generator feed water systems is necessary and very important from the operational as well as nuclear safety point of view. Steel STN 17 247 proved 5 years in operation at SG35 seems to be the optimal solution of this problem. Nevertheless, periodical inspection of the feed water tubes corrosion (after 10, 15 and 20 years) was recommended.

Based on the results of visual inspection performed on April 19, 2002 at SG16 (NPP V1), it was confirmed, that the steam generator was in well condition also after 23 years of operation. Specimens taken from the internal body surface of PG16 confirmed that hematite concentration increases in the vertical direction (from the bottom part to the top one).

Results from 2008 confirm good operational experiences and suitable chemical regimes (reduction environment), which results mostly from the creation of magnetite (on the level of 70% or higher) and small portions of hematite, ghoetite or hydroxides.

Regular observation of the corrosion-erosion processes is essential for keeping NPP operation on a high safety level. The output from performed material analyses influences the optimization of operating chemical regimes as well as it can be used in the optimization of regimes at decontamination and passivation of pipelines or secondary circuit components. It can be concluded that longer passivation time leads more to magnetite fraction in the corrosion products composition.

Differences in hematite and magnetite contents in corrosion layers taken from hot and cold collectors at SG11 in 2004 have shown that there is a significant lower presence of magnetite in case of hot collector. This fact can be devoted from 2 parallel factors: (i) difference in temperature (about 298°C – HC) and (about 223°C - CC) and mostly due to (ii) higher dynamics of secondary water flowing in the neighbourhood of hot collector, which high probably remove the corrosion layer from the collector surface.

With the aim to summarize our results in the form suitable for daily use in the operational conditions, a “corrosion map” was created (see Fig. 13). Corrosion products phase composition (limited to magnetite and hematite only) is presented in the form of circular diagrams.

Basically, the corrosion of new feed water pipelines system (from austenitic steel) in combination to operation regimes (as at SG35 since 1998) goes to magnetite. In specimens taken from positions 5 to 14 (see Fig. 13 – right corner), the hematite presence is mostly on the internal surface of SG body (constructed from “carbon steel” according to GOST 20K). Its concentration increases towards the top of the body and is much significant in the same part of SG where flowing water via erosion removes the corrosion layer better than from the dry part of the internal surface or the upper part of the pipeline.

The long-term study of phase composition of corrosion products at VVER reactors is one of the preconditions to the safe operation over the projected NPP lifetime. The long-term observation of corrosion situation by Mössbauer spectroscopy is in favour of utility and is not costly. Based on the achieved results, the following points could be established as an outlook for the next period:

1. In collaboration with NPP-Bohunice experts for operation as well as for chemical regimes, several new additional samples from not studied places should be extracted and measured by Mössbauer spectroscopy with the aim to complete the existing “corrosion map”.
2. Optimization of chemical regimes (having in mind the measured phase composition of measured corrosion specimens from the past) could be discussed and perhaps improved.
3. Optimization and re-evaluation of chemical solutions used in cleaning and/or decommissioning processes during NPP operation can be considered.

In connection to planned NPP Mochovce 3, 4, commissioning announced officially for 2013, it is recommended that all feed water pipelines and water distribution systems in steam generators should be immediately replaced before putting in operation by new ones constructed from austenitic steels. The Bohunice design with feed water distribution boxes is highly recommended.

Acknowledgement

This project was supported by VEGA 7/0129/09 and by SE, a.s. Company.

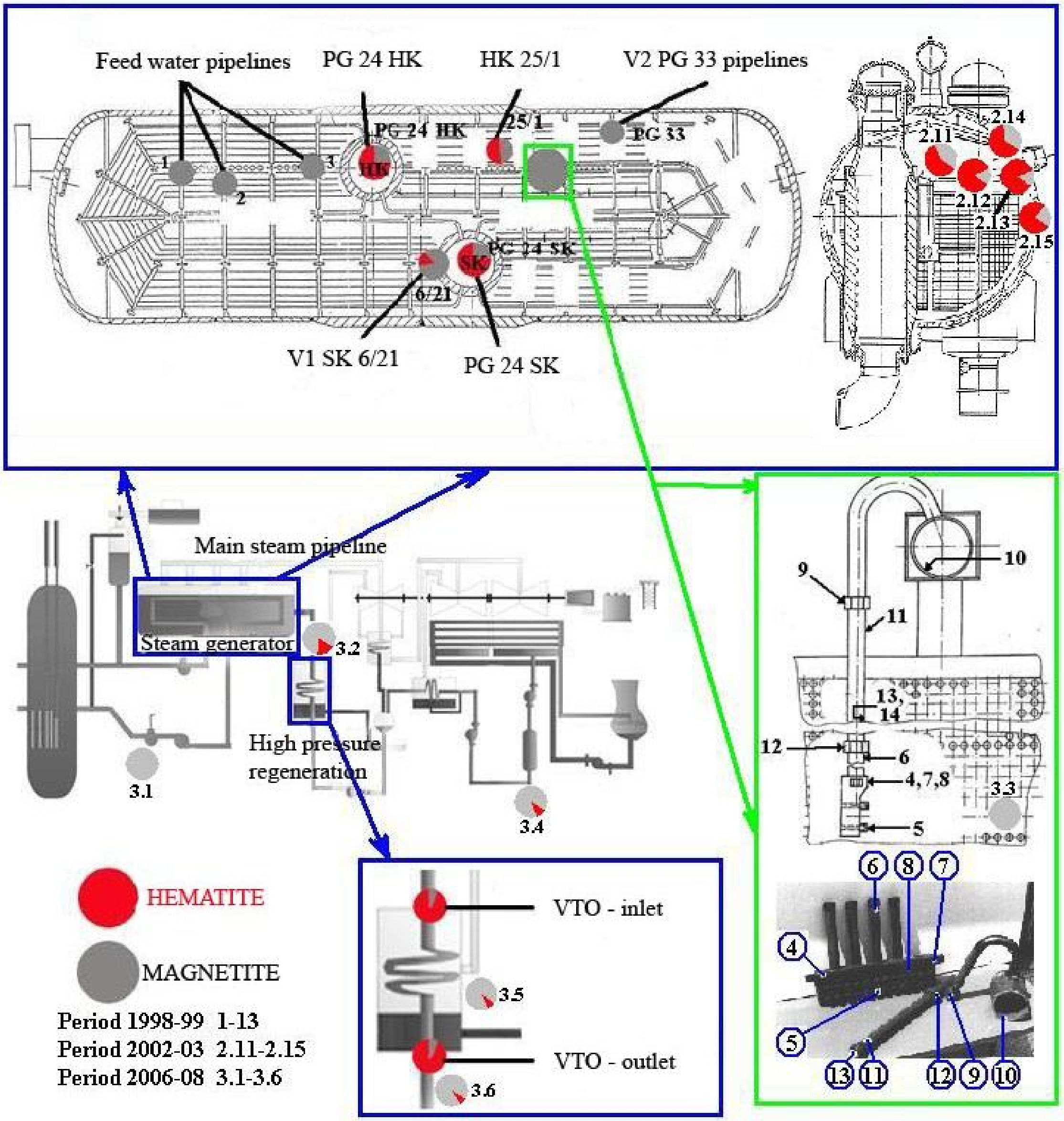

FIG. 13. "Corrosion map" of NPP V-2 Bohunice (Slovakia) performed according to results from period 1998-2008.

References

[1] Cohen, L., Application of Mössbauer Spectroscopy. Volume II. ed. Academic Press, (USA, New York, 1980).

[2] Gibb, T.C., Principles in Mössbauer Spectroscopy, Chapman and Hall, London, (1971).

[3] Greenwood, N.N. and Gibb, T.C., Mössbauer Spectroscopy, Chapman and Hall, London, (1971).

[4] Brauer, G., Matz W. and Fetzer, C., Hyperfine Interactions, 56 (1990) 1563.

[5] Lipka, J., Blazek, J., Majersky, D., Miglierini, M., Seberini, M., Cirak, J., Toth I. and Gröne, R., Hyperfine Interactions, 57 (1990) 1969.

[6] Phythian, W.J. and English, C.A., J. Nucl. Mater., 205 (1993) 162.

[7] Belozerski, G.N., Mössbauer studies of surface layers, Elsevier, (1993).

[8] Slugen, V., Mössbauer Spectroscopy in Material Science, Kluwer Academic Publishers, Netherlands, (1999) 119-130.

[9] Savolainen, S. and Elsing, B., Exchange of Feed Water Pipeline at NPP Loviisa., Proceedings of the 3rd seminar about horizontal steam generators, Lappeenranta, Finland, 18.20.10.(1994).

[10] Technical Descripcion of SG PGV-4E, T-1e, (B-9e/241/), (1978) (in Slovak).

[11] Safety Report V-1, Chapter IV.3 Primary Circuit, Normative Documentation A-01/1,2, (1978) (in Slovak).

[12] Steamgenerator Technical Report DTC 1.01.2 - 1.unit V1, Documentation to Real Status to 30.4.1994 (in Slovak).

[13] Brauer, G., Matz W. and Fetzer, C., Hyperfine Interactions, 56 (1990) 1563.

[14] Belozerski, G.N., Mössbauer Studies of Surface Layers, Elsevier, (1993).

[15] Slugen, V., Mössbauer Spectroscopy in Material Science, Kluwer Academic Publishers, Netherlands, (1999) 119-130.

[16] Savicki, J. A. and Brett, M. E., Nucl. Instrum. Meth. In Phys. Res., B76 (1993) 254.

[17] Cech, J. and Baumeister, P., Proc. of 2nd International Symposium on Safety and Reliability Systems of PWRs and VVERs, Brno, (1997) 248.

[18] Matal, O., Gratzl, K., Klinga, J., Tischler J. and Mihálik, M., Proc. of the 3rd International Symposium on Horizontal Steam Generators, Lappeenranta, Finland (1994).

[19] Matal, O., Simo, T. and Sousek, P., Proc. of 3rd International Symposium on Safety and Reliability Systems of PWRs and VVERs, Brno, (1999).

[20] Slugen, V. and Magula, V., Nuclear Engineering and Design, 186/3 (1998) 323.

[21] Varga, K. et al., Journal of Nuclear Materials, 348 (2006) 181.

[22] Slugen, V., Segers, D., de Bakker, P., DeGrave, E., Magula, V., Van Hoecke, T. and Van Vayenberge, B., Journal of Nuclear Materials, 274 (1999) 273.

[23] De Grave, E., Report 96/REP/EDG/10, RUG Gent 1996.

[24] Kučera, J., Veselý, V. and Žák, T., Mössbauer Spectra Convolution Fit for Windows 98/2K, (2004), Ver. 4.161.

[25] Cornell, R. M. and Schwertmann, U., The Iron Oxides, (1996), ISBN 3-527-28576-8.

[26] Lipka, J. and Miglierini, M., Journal of Electrical Engineering, 45 (1994) 15.

[27] Morup, S., Topsoe, H. and Lipka, J., Journal de Physique, 37 (1976) 287.

[28] Kritsky, V. G., Water Chemistry and Corrosion of Nuclear Power Plant Structural Materials, (1999), ISBN 0-89448-565-2.

[29] Korecki, J. et al., Thin Solid Films, 412 (2002) 14.

Volume 5, Number 2, 2012. pp. 67-75

Jordan Journal of Physics

ARTICLE

The Influence of Electrode Angle on the Minimization of the Aberration Coefficients of the Two Electrodes Electrostatic Immersion Lens

M.A. Al-Khashab and **A.A. Ahmad**

Physics Department, College of Science, Mosul University, Mosul, Iraq.

Received on: 30/4/2011; Accepted on: 26/2/2012

Abstract: This paper deals with the electron optical properties of a set of asymmetrical electrostatic immersion lenses with two electrodes which have been designed using different angles (θ) of the outer lens electrodes as well as air gaps (S) between the electrodes of each lens. It was found that the angle of the outer electrode and the air gap have a clear effect on the electron optical performance of such lenses. In addition to that, it was noticed that the better electron optical properties occurred when the angle of the outer electrode equals ($\theta = 0^o$) and the air gap equals (S = 11 mm). The results of the preferable design of the present work were compared with those in published papers in terms of the optical properties. It was found that the results are in good agreement with each other.

Keywords: Asymmetrical electrostatic immersion lens; Angle of the outer electrode; Air gap.

Introduction

A wide variety of electrostatic lenses has been used for focusing charged particles [1, 2]. The appearance and physical properties of lenses which were previously designed for different applications are totally different in geometrical shape. It is difficult to develop a general optimal lens design for all applications. A systematic investigation on a suitable lens is possible only if we are able to identify the most characteristic parameters and investigate their influence on the optical properties of different lenses. It is also evident that one can only hope to find such simple geometrical parameters in terms of the axial potential distribution [3].

Two-element electrostatic lenses have been used in low energy electron spectrometers in order to increase sensitivity and resolution [4]. Coaxial cylinder electrostatic lenses are mainly used for accelerating or decelerating the electron or ion beams. Firestein and Vine gave in 1963 useful design criteria for overlapping two cylindrical lenses [5]. This configuration gives the least spherical aberration in which the cylinder at high potential has the smallest diameter. Details of the optical properties for several types of two-element coaxial cylinder electrostatic lenses were found in many references such as [3, 6]. It is well known that a two-element lens system cannot keep the image position constant while varying the ratio of final to initial electron energy. Details of the properties of several types of electrostatic lenses can be found in [7]. The focal properties of multi-electrode electrostatic lenses have been obtained by [8] using electrostatic immersion lenses and by [9] using unipotential electrostatic lenses. Moreover, (Abd-Hujazie, 2006), (Frosien et al., 2009), (Al-Jumayli, 2010), (Al-Khashab and Hujazie, 2010) and (Al-Khashab and Hujazie, 2011) [10-14] used two electrodes electrostatic immersion lenses for different geometry and distance between two electrodes.

The imaging properties of electrostatic lenses and their aberration are less well known. The properties of the lens approximation have been much less systematically studied, partly because

Corresponding Author: A.A. Ahmad **Email**: alaahakeim74@yahoo.com

of premature loss of interest in electrostatic optics. Electrostatic lenses are difficult to characterize. Even for a simple lens, there are several geometrical parameters involved (thickness of electrodes, electrode air gap distances and diameters and the electrode shapes) that affect the potential distribution. For the above reasons, the production of the universal curves for the electrostatic lenses is not of similar manner like the universal curves of magnetic lenses [15]. The final design would usually be based on trial and error, different electrode geometries and voltages are tried until acceptable results are achieved.

The aim of this paper is to achieve an improved design for the electrostatic immersion lens suitable for an objective lens. The work tackles the influence of the outer electrode angle as well as the influence of the electrodes air gap on the performance of these lenses which have been investigated under the same optical conditions.

The Consideration of Asymmetrical Electrostatic Lens Design

Intensive studies on asymmetrical electrostatic immersion lenses have been carried out on a family of identical lenses which are designed to consist of two coaxial electrodes overlapping each other. The inner electrode I(in) is in the form of a cylinder, while the outer electrode II(out) is in the form of a conical shape. The studies have been carried out through two principal parts:

In the first part, a set of the asymmetrical electrostatic lenses are designed with a constant geometry of the inner electrode while different angles of the outer electrode have been changed to find the preferred lens design.

In the second part, the effect of the air gap between the two electrodes on the electron optical properties has been studied for the lenses which possess a preferred design of outer electrode angle obtained from the former part.

The cross-section of the lens geometry and the design parameters are shown in Fig. 1. The lens model is asymmetrical in shape; namely (two coaxial cylinders) and consists of two electrodes in the form of an overlapping system. Therefore, the geometry of the inner electrode I(in) in the form of a cylinder remains constant, and the outer electrode II(out) like a conical shape makes an angle θ with the horizontal direction. The air gap (S) between the electrodes is chosen to be (7mm).

The investigation has required extensive calculation based on several physical and mathematical concepts. The design work and calculation are accordingly handled with the aid of a personal computer, so that several computer programs are being employed in order to understand the behavior of electrostatic lens system. A technique for calculating the equipotential lines due to the effect of the outer electrode angle as well as the electrodes air gap on the electrostatic lens is also presented. Each shape is illustrated by a typical computer result on graphical screen. It should be born in mind that the optical properties of the lenses have been investigated under zero magnification conditions.

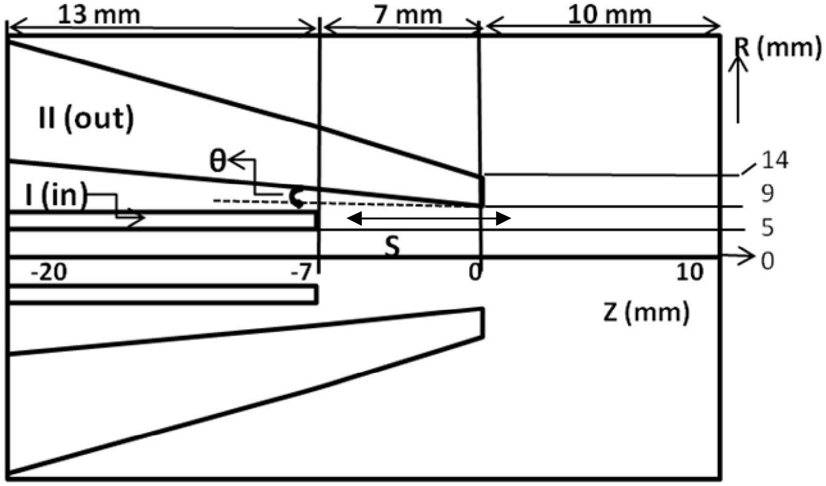

FIG. 1. Schematic diagram of the cross-section of the asymmetrical two-coaxial electrodes electrostatic lens design, showing the inner I(in) and outer II(out) electrodes.

The Effect of Outer Electrode Angle Design

In order to investigate the effect of the outer electrode angle on the two-electrode electrostatic lens designed, the inner electrode represented by I(in) was chosen of a constant geometry at a voltage of ($V_{I(in)} =$ 8000 V). However, the outer electrode like a conical shape represented by II(out) was chosen with different angles θ (0^o - 40^o) and at a constant voltage of ($V_{II(out)}$ = 100 V). These lenses have been studied under zero magnification conditions.

In order to investigate the performance of the electrostatic lens with the variation of the outer electrode angle, five configurations of the lens model of an identical geometry are chosen. Different angles in the range (0^o - 40^o) and a constant air gap which equals (7mm) were selected. The calculation of the properties of any electrostatic lens requires knowing the axial potential distribution V_z along the optical axis Z. The values of V_z for the electrostatic lenses are computed with the aid of program E11 [16], using the finite element method. The analysis is based on dividing the upper half of the cross-section for each of the lenses into quadrilateral areas so as to make the lens geometry correctly specified. The total number of the meshes was chosen to be constant for all lenses designed with a size which is equal to (15 radial x 20 axial). Fig. 2 shows the axial potential distribution V_z as a function of Z for the previous lenses of angles (0^o - 40^o), where the voltages of the inner and outer electrodes equal ($V_{I(in)}$ = 8000 V) and ($V_{II(out)}$ = 100V), respectively. Therefore, the region from (Z = - 20 mm to - 6 mm) is given in the above figure and is called a divergent region. In this region, the longitudinal component of the electric field accelerates the electrons. Thus, the diverging power diminishes as the divergence action lasts for a shorter time, while the region from (Z = - 2mm to 10mm) is called a converging region. The longitudinal component of electric field retards the electrons, and the converging power increases. Consequently, the converging effect exceeds the diverging effect and the whole lens becomes convergent [17].

In order to demonstrate the performance of the previous lenses at different outer electrode angles, the trajectory ray R(z) inside the lenses has been computed by program E21 [16] for calculating the optical properties of these lenses by solving the paraxial ray equation, using the fourth order-Runge-Kutta formula [18]. Figure 3 indicates the trajectories of the electrons inside the lenses at constant inner and outer electrode voltages as mentioned above and at a constant air gap (S = 7 mm). This figure shows that the lens that possesses the outer electrode of ($\theta = 0^o$) has acquired a minimum value of the working distance (W.D.) in the image plane at (Z_i = 7.2 mm), which in turn, gives an acceptable performance in comparison with other electrostatic lenses.

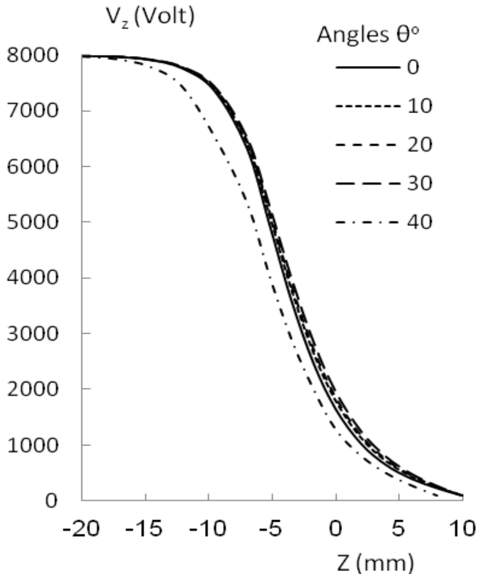

FIG. 2. The axial potential distribution of the electrostatic lenses of different angles (θ) at voltages $V_{I(in)}$=8000 and $V_{II(out)}$=100V.

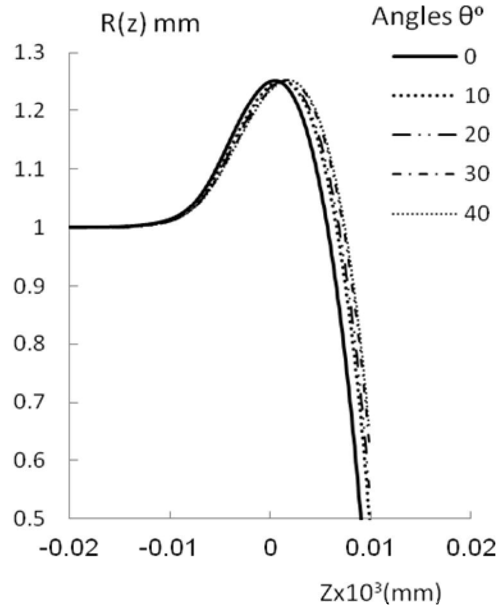

FIG. 3. The trajectories of the electrons inside the electrostatic lenses of different angles (θ) at constant voltages VI(in)=8000 and VII(out)=100V.

In order to study the effect of the outer electrode angles θ(0^o - 40^o) on the above lenses, it is important to compute the equipotential lines of the electrons inside the structure of these lenses. The trajectory of equipotential lines of the electrons of the previous lenses has been calculated by using program E31 [16] and modified by [10]. Fig. 4 illustrates the trajectories of equipotential lines for the above lenses at constant mentioned conditions. It is noticed that the equipotential lines are more converging toward the optical axis as in the lens of (θ= 0^o) compared to those in the other lenses whose equipotential lines are more diverging away from the optical axis. Therefore, the focusing of the electrons is displacing away from the specimen position. This behavior is important for reducing the beam voltage reaching the specimen surface. This is one of the important parameters to protect the specimen from damage.

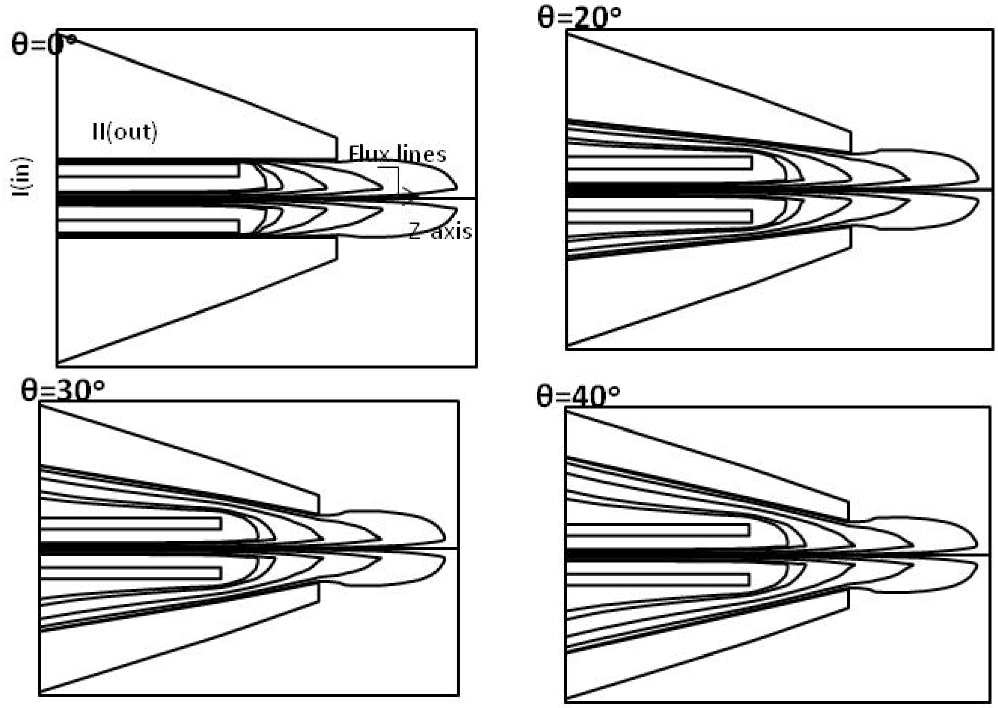

FIG. 4. The equipotential lines of the electrostatic lenses of different angles, at constant voltages ($V_{I(in)}$ = 8000 V) and $V_{II(out)}$ = 100 V).The air gap between the two electrodes (S = 7 mm).

Before a commitment is made as to which angle of the lenses is the most suitable, the objective focal properties must be investigated.

In order to evaluate the effect of outer electrode angle on the electron optical properties of the previous lenses, the objective focal properties have been calculated by program E21 [16].

The most important optical properties of an objective lens are: the objective focal length f_e, spherical and chromatic aberration coefficients C_s and C_c, respectively. When the relative aberration coefficients are considered, the results will be independent of any scaling factor. The variation of the relative spherical and chromatic aberration coefficients (C_s/f_e, C_c/f_e) of the electrostatic lenses as a function of the outer electrode angle is shown in Fig. 5. It is noticeable that both curves are similar in shape and their values increase slowly with increasing the angle in the region where θ(0^o - 20^o), but the rate of the values increases a little bit more in the region where θ > 20^o. It is clear from the above mentioned figure that the lenses of outer electrode angles (θ = 0^o) and (θ = 20^o) have relatively lower aberration coefficients than other lenses of higher angles. So, the above angles (0^o, 20^o) can be regarded to present the best design adopted in the next part of the investigations.

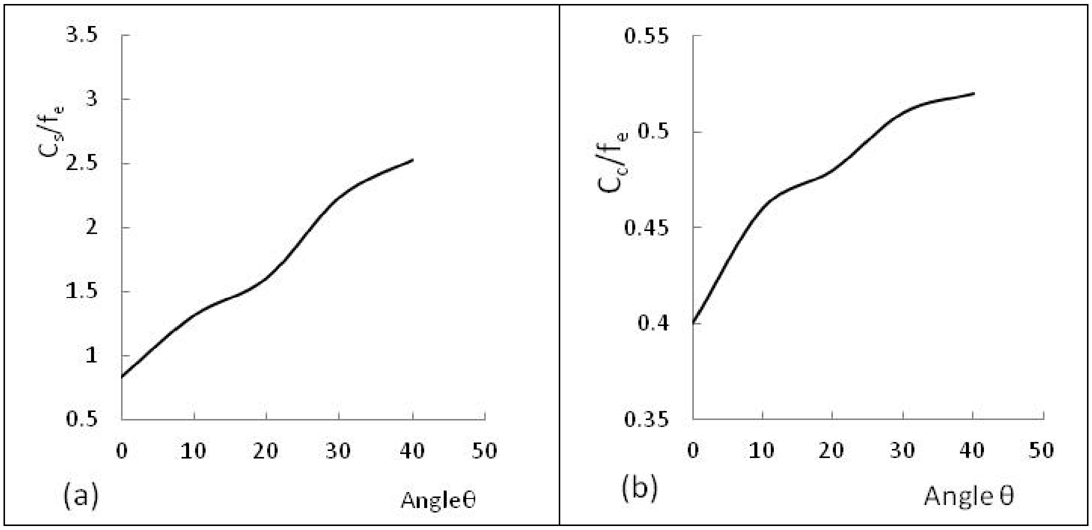

FIG. 5. Variation of the:(a)relative spherical aberration coefficient (C_s/f_e) and (b)relative chromatic aberration coefficient (C_c/f_e) of the lenses as a function of the angle at ($V_{I(in)}$= 8000V and $V_{II(out)}$= 100V).

The Effect of Air Gap Electrodes Design

Research work has been conducted on the influence of air gap electrodes distance on the other set of electrostatic lenses.The principles in the above section can be applied to the different air gap lenses at the preferred angles (0^o and 20^o), respectively. This involves operating the lenses at the same optical conditions ($V_{I(in)}$ = 8000V, $V_{II(out)}$ = 100V) and at zero magnification conditions.

In order to calculate the variation in the electron optical properties of the two types of lenses having angles (0^o and 20^o) with the air gap, six different kinds of asymmetrical electrostatic lenses are chosen for the performance of detailed calculation. The corresponding values of the air gap distance are taken [S = (0,3,5,7,10,11 &15) mm], respectively for the two types of lenses (0^o and 20^o). These lenses are identical in all dimensions.

The variations of the axial potential distribution of the previous lenses for different air gaps are calculated at constant electrode voltages ($V_{I(in)}$ = 8000V and $V_{II(out)}$ = 100V) as demonstrated in Fig. 6 for the angles (a) $\theta = 0^o$ and (b) $\theta = 20^o$. It is noticed from this figure that the half-width of the potential distribution in both angles decreases as the distance of air gap increases; see Fig. 6(a and b), (i.e. when the inner electrode I(in) becomes far from the specimen). Other tests for the air gap distance were performed and yielded the fact that the preferred electrode angles (0^o and 20^o) produce the best optical performance. It is worthy to calculate the trajectories of electrons inside the previous electrostatic lenses in order to compare their optical performances. The trajectories of electrons R(z) of these lenses as a function of Z are calculated at the same optical conditions as mentioned before for different air gaps of the two values of angles ($0^o$and 20^o) as illustrated in Fig. 7. When the air gap value increases, the working distance decreases. It is clear that there is a linear relation between them as given in Fig. 7(a and b).This in turn will give good results in relation to the optical performance of these lenses.

Systematic investigations have been carried out on the effect of the air gap on equipotential lines of electrostatic lenses for both angles ($\theta = 0^o$) and ($\theta = 20^o$) at the same optical conditions as mentioned before in order to compare the trajectories of equipotential lines in the structures of these lenses. The equipotential lines of the previous lenses for different air gaps are calculated at the same voltages as represented by graphical results shown in Fig. 8. It is noticeable that for the lens of the air gap (S = 0), the equipotential lines emerge in the circular paths from the outer electrode region compared with the lens of (S = 15mm). The equipotential lines are converging toward the optical axis and do not exceed the outer electrode region in both angles ($\theta = 0^o$ and $\theta = 20^o$); therefore, the air gap of (S = 15 mm) can be considered a preferred gap for these lenses. It should be mentioned that the air gap distance has a great effect on the electron optical properties of the asymmetrical electrostatic lenses.

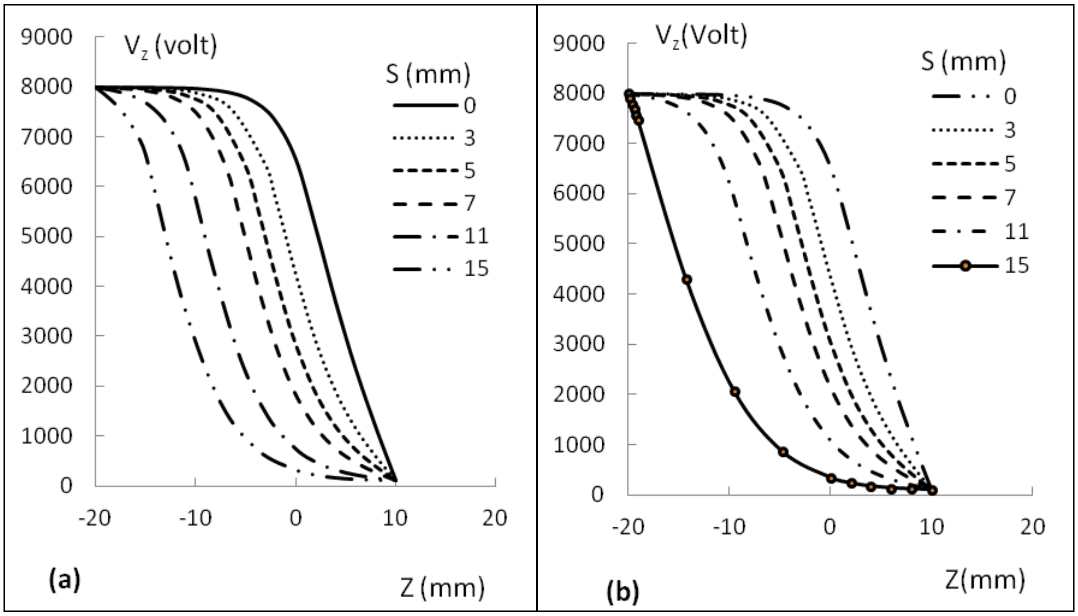

FIG. 6. The axial potential distribution of the electrostatic lenses of different air gaps (S) at voltages ($V_{I(in)}$=8000V and $V_{II(out)}$=100V) of the two values of angle (a) θ = 0° and (b) θ = 20°.

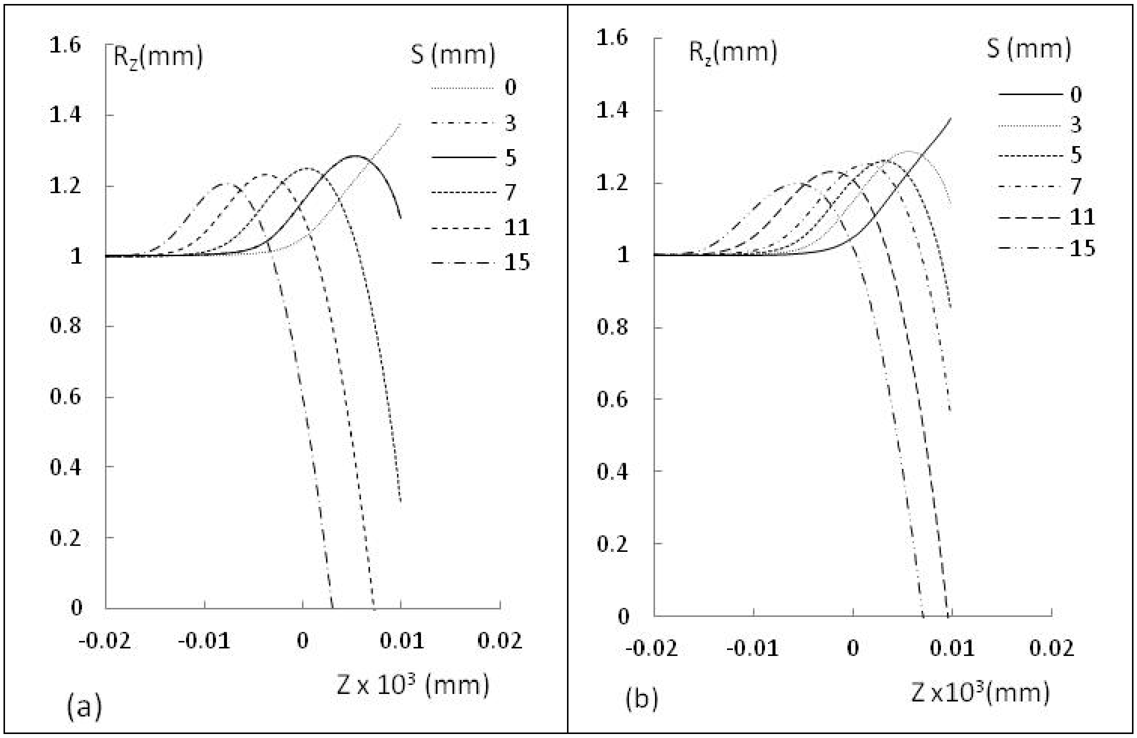

FIG. 7. The trajectories of the electrons inside the electrostatic lenses of different air gaps (S) at voltages (VI(in) = 8000 V and VII(out) =100 V) of the two values of angle (a) θ = 0° and (b) θ = 20°.

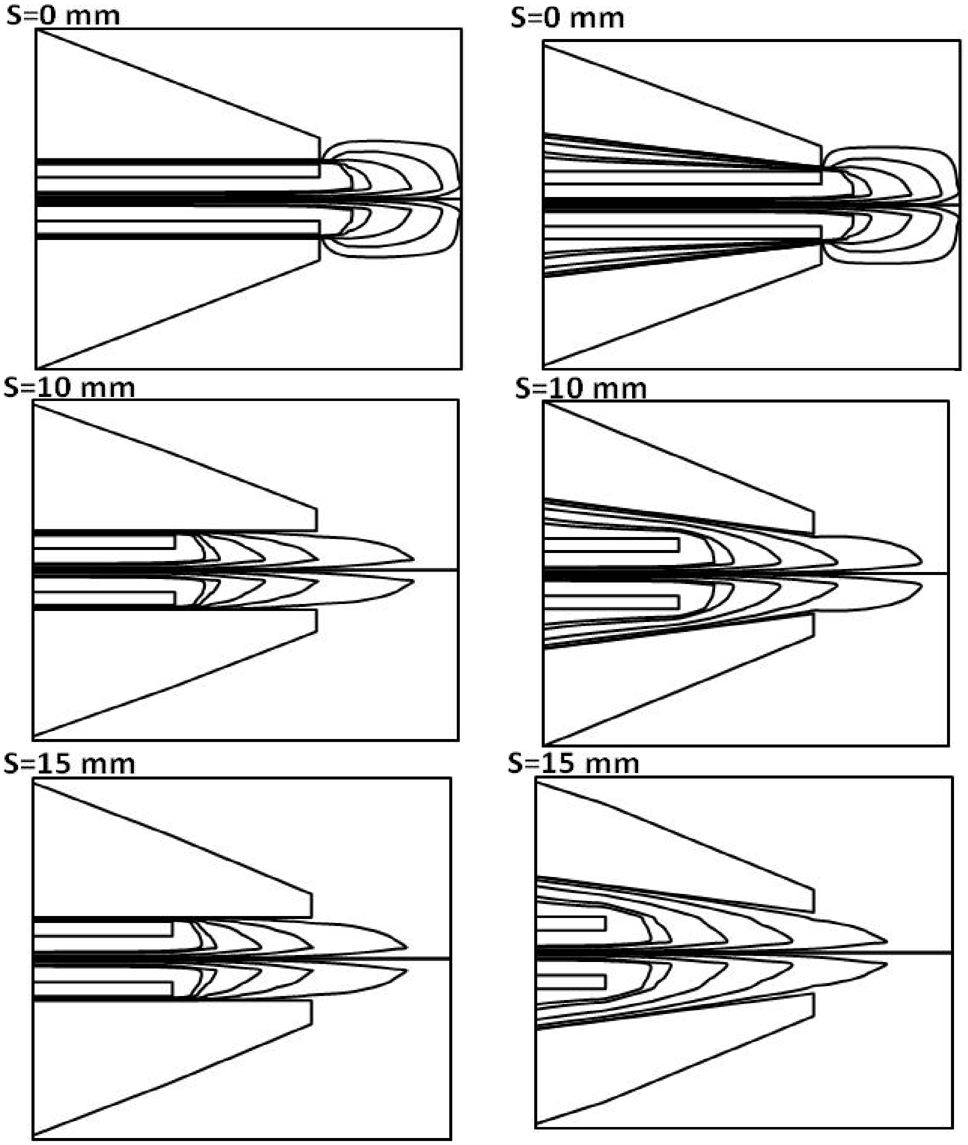

(a) θ = 0° **(b) θ = 20°**

FIG. 8. The equipotential lines of electrostatic lenses of different air gaps S = (0, 10, 15) mm at voltages (VI(in) = 8000 V and VII(out) =100 V) of the two values of angle: (a) θ = 0° and (b) θ = 20°.

This paper studies the impact of both parameters, the air gap (S) and the outer electrode angle (θ), on the improvement of the electron optical properties of the electrostatic lenses. A systematic investigation has been carried out on the effect of the above parameters (S and θ) on the optical properties in order to obtain the performance of these lenses. The spherical and chromatic aberration coefficients of these lenses were calculated as mentioned in the previous section at the same optical conditions. Fig. 9 shows a comparison between the relative spherical aberration coefficient (C_s/f_e) of the above lenses of angles (θ = 0° and θ = 20°) as a function of the air gap at the same inner and outer electrode voltages ($V_{I(in)}$= 8000V) and ($V_{II(out)}$ = 100V) respectively. It is noticed from Fig. 9 that both curves for (θ = 0°,θ = 20°) intersect and acquire their lowest values of the relative spherical aberration coefficient at (S = 11 mm). Fig. 10 also shows a comparison between the relative chromatic aberration coefficient (C_c/f_e) of the two types of electrostatic lenses of angles (0° and 20°) as a function of air gap at constant voltages as mentioned above. From the previous figure, it can be noticed that the curve of (θ = 0°) has acquired the lowest value of (C_c/f_e) at (S = 13 mm) in comparison with the other curve of (θ = 20°), and their values decrease irregularly.

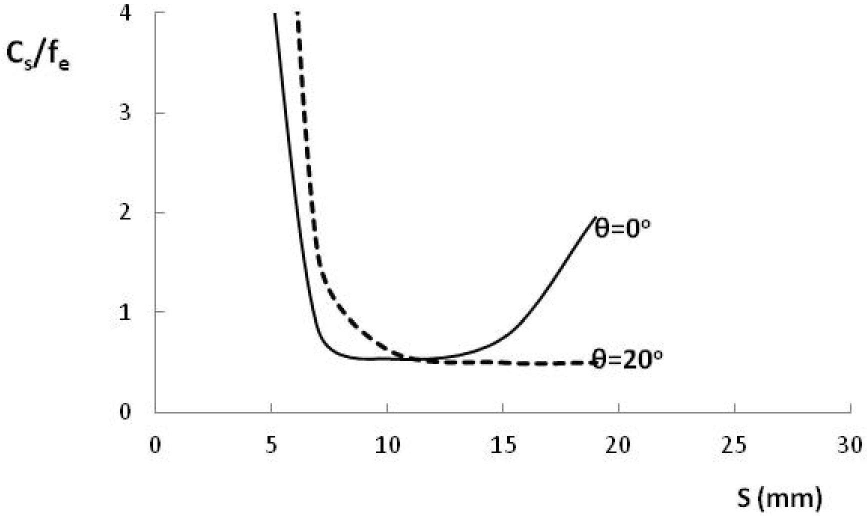

FIG. 9. Comparison between the relative spherical aberration coefficient (C_s/f_e) of the two types of electrostatic lenses of angles (0° and 20°) as a function of the air gap at constant voltages (VI(in) = 8000 V and VII(out) = 100 V).

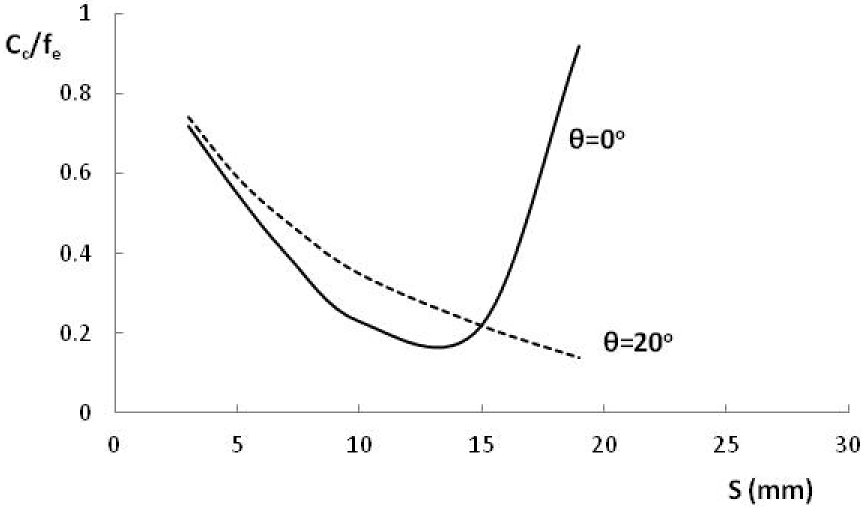

FIG. 10. Comparison between the relative chromatic aberration coefficient (C_c/f_e) of the two types of electrostatic lenses of angles (0° and 20°) as a function of the air gap at constant voltages (VI(in)=8000V and VII(out) = 100V).

From the above investigation, it is interesting to point out that there are progressive developments in the electron optical properties of the electrostatic lenses concerning the above discussed parameters.

Comparison with Earlier Published Results

In this section, a comparison between the electron optical performance of the preferred asymmetrical electrostatic lenses designed and presented at this work with that of other electrostatic lenses studied earlier by other researchers as indicated in Table 1. It can be noticed that the lowest values of the relative spherical and chromatic aberration coefficients occur corresponding to the present work in comparison with those of recently published results by other researchers which in turn gives a better resolution in comparison with other lenses. However, these lenses have verified higher resolution in the image formation of the electron microscope.

TABLE 1. Comparison between the relative spherical and chromatic aberration coefficients (C_s/f_e and C_c/f_e) for the asymmetrical electrostatic lenses of the present work with those of published results.

Lenses of published results	C_s/f_e	C_c/f_e	$V_{II(out)}$ (Volt)
Al- Meshhadany (2002) [19]	3.60	0.79	-------
Abd- Hujazie (2006) [10]	0.53	0.26	100
Al-Khashab and Al-Shamma (2009a) [8]	4.85	4.20	100
Al-Khashab and Al-Shamma (2009b) [9]	2.68	0.60	100
Present work ($\theta = 0^o$, S = 11 mm)	0.53	0.19	100
Present work ($\theta = 0^o$, S = 13 mm)	0.59	0.16	100

Conclusions

It is found out from the foregoing analysis that the plots of equipotential lines can be very essential in the early design stages of the real system, since they can often explain the apparently unusual behavior of the lens in comparison with the design expectations based on axial potential distribution only.

In the present investigation, it has been observed that the outer electrode angle together with the air gap of the electrodes have a very important effect on the design characteristics of the asymmetrical electrostatic lenses and consequently on their objective focal properties. This lens design of ($\theta = 0^o$ and S = 11mm) probably represents the best performance that can be obtained with the present technology.

References

[1] Hanszen, K.J. and Lauer, R., in: Focusing of Charged Particles, A.Septies, Ed. (Academic, New York, 1967) Ch.2.2.

[2] Mulvey, T. and Wallington, M.J., Rep. Prog. Phys. 36 (1973) 347.

[3] Szilagyi, M., J. Vac. Sci. Technol. A5 (1987) 273.

[4] Kuyatt, C.J. and Simpson, J.A., Rev. Sci. Instrum. 38 (1967) 103.

[5] Firestein, F. and Vine, J., Br. J. App1. Phys. 14 (1963) 449.

[6] Hawkes, P.W. and Kasper, E., Principle of Electron Optics, (Academic Press, London, 1996).

[7] Al-Shamma, M.T.M., M.Sc. Thesis, Mosul University, Mosul, Iraq, (2007).

[8] Al-Khashab, M.A. and Al-Shamma, M.T.M., Dirasat, Pure Sciences, 37(2) (2009a) 171.

[9] Al-Khashab, M.A. and Al-Shamma, M.T.M., Dirasat, Pure Sciences, 37(2) (2009b) 183.

[10] Abd-Hujazie, N.S., Ph.D. Thesis, The University of Mosul, Iraq, (2006).

[11] Frosien, J., Plies, E. and Anger, K., Journal of Vacuum Science and Technology, 7(6) (2009) 1071.

[12] Al-Jumayli, F.A.M., Ph.D. Thesis, The University of Mosul, Iraq, (2010).

[13] Al-Khashab, M.A. and Hujazie, N.S., Dirasat, Pure Sciences, 37(2) (2010) 85.

[14] Al-Khashab, M.A. and Hujazie, N.S., Dirasat, Pure Sciences, 38(1) (2011) 52.

[15] Lencova', B., Nuclear Instruments and Methods in Phys. Research, Section A (1995) 1.

[16] Munro, E., A Set of Computer Programs for Calculating the Properties of Electron Lenses, Report CUED/B-ELECT/TR 45, Cambridge University, Eng. Dept., (1975).

[17] Grivet, P., Electron Optics, Part 1 Translated by Hawkes, P.W.,(Pergamon Press Oxford, 2nd English Edition, 1972).

[18] Lencova', B. and Lenc, M., Optik, 97(3) (1994) 121.

[19] Al-Meshhadany, I.A.M., M.Sc. Thesis, Baghdad University, Iraq, (2002).

Volume 5, Number 2, 2012. pp. 77-88

Jordan Journal of Physics

ARTICLE

Factors Affecting Gamma Ray Transmission

N. A . Alallak and **S. S. Sarhan**

Department of Engineering, Arab Community College, Amman, Jordan.

Received on: 27/6/2011; Accepted on: 16/2/2012

Abstract: Gamma ray transmission and the parameters which affect this process; attenuation coefficients, cross-sections, effective atomic numbers and electron densities, were studied for brass, Fe, Al, PVC and Perspex, using gamma spectroscopy. The comparison between experimental and theoretical values is made; these are found to be in good agreement. The inverse relations between energy and attenuation coefficients, as well as cross-sections were emphasized. In the energy range (661.6 keV-1332.5 keV), the effective atomic numbers showed a constant behavior with energy. Brass shows up as a good attenuating material, while other samples are relatively weak attenuators. The effect of the composition of the compound appears obviously in this study.

Keywords: Attenuation coefficients (linear and mass); Cross-sections; Effective atomic number; Electron density.

Introduction

Increasing the use of gamma active isotopes in support of application, makes the study of the absorption and interaction of gamma radiation in materials an important research field. The photon attenuation coefficients (linear and mass attenuation coefficients), effective atomic number and electron density are basic quantities required in determining the attenuation of X-rays and gamma photons in matter.

The purpose of this research is studying the factors which affect gamma ray transmission in different methods. The comparison between different methods and between experimental and theoretical values for each factor is made.

The importance of the attenuation of photons has prompted many investigators to measure the attenuation coefficients, effective atomic number and electron density by employing different methods. Some of these factors are determined for alloys [1-3], amino-acids [4-5], thermo-luminescent dosimetrics (TLD) [6], superconductors [7] and building materials [8]. Other used X-ray to determine the effective atomic numbers of materials of dosimetric interest at energies 1-20 keV [9]. Another paper reports a comprehensive set of formulae for calculating the effective atomic numbers and electron densities for all types of materials and for energies above 1 keV [10]. Some investigators defined the previous parameters, and further they found a quantity called effective atomic weight which they defined as the ratio of the molecular weight of a sample to the total number of atoms of all types composing it. A new effective atomic number relation has been evolved [11]. Also, variation method and Compton scattering are two different methods used to calculate the effective atomic number [12].

In this work, the transmission factors; linear and mass attenuation coefficients, effective atomic numbers, cross-sections and electron densities are studied for five different kinds of samples, which are pure elements (Al, Fe), thermoplastic (Perspex, PVC) and alloy (Brass), by using gamma ray spectroscopy.

The linear attenuation coefficients of the samples are determined by the transmission

Corresponding Author: S. S. Sarhan **Email**: s3m_rose@yahoo.com

experiments as a Non-destructive testing method, under a good geometry condition (collimated gamma ray transmission method).

As a photon makes its path through a matter, there is a probability that it makes an interaction with the material such as absorption (photoelectric effect), scattering (Rayleigh or Compton scattering) or splitting (pair production). Therefore, part of the incident beam of intensity (I_o) will be partially or completely removed from the beam as a result of interaction(s) within the absorber of thickness x. This reduces the transmitted intensity that reaches the detector to (I), where, introducing μ, the linear attenuation coefficient, the transmitted intensity is given by;

$$I(x) = I_o \exp(-\mu x) \qquad (1)$$

This is called the Beer-Lambert law, where μ measured in units of length^{-1} describes the probability of absorption or scattering occurring per unit length within the absorber material [13]. The exponential means that equal thickness of the absorber attenuates the photon beam by an equal fraction or percentage [14].

μ is also called the total attenuation coefficient due to the contribution of different effects in the attenuation process. Hence, the total attenuation coefficients may be expanded as:

$$\mu = \omega + \tau + \sigma + \kappa + \pi \qquad (2)$$

where, ω: the probability of coherent scattering, τ: the probability of photoelectric absorption, σ: the probability of Compton scattering, κ: the probability of pair production and π: the probability of photodisintegration.

Therefore:

$$\left.\begin{aligned}\exp(-\mu x) &= \exp(-\omega x) + \exp(-\tau x)\\ &+ \exp(-\sigma x) + \exp(-\kappa x)\\ &+ \exp(-\pi x)\end{aligned}\right\} \qquad (3)$$

To overcome the dependence of the linear attenuation coefficient on the absorber density (ρ), it is normalized by the absorber density. Hence, the mass attenuation coefficient is defined as;

$$\mu_m = \mu / \rho \qquad (4)$$

Using μ_m instead of μ, equation (1) becomes:

$$I(x) = I_o \exp(-{}^{\mu}\!/_{\rho})\rho x \qquad (5)$$

In the case of a compound of various elements, it is assumed that the contribution of each element of the compound to the total photon interaction is additive, obeying the well-known mixture rule and it is also called Bragg law. Therefore, the mass attenuation coefficient for the compound can be written as:

$$(\frac{\mu}{\rho})_{mix} = \sum_i w_i (\frac{\mu}{\rho})_i \qquad (6)$$

where w_i is the weight fraction of the element i ($w_i = a_i A_i / \sum a_j A_j$; here A_i is the atomic mass of the ith element, and a_i is the number of atoms of this element in the compound), $(\mu/\rho)_i$ is the mass attenuation coefficient for element i.

Berger and Hubbell developed XCOM, for calculating mass attenuation coefficients or photon interaction cross-sections for any element, compound or mixture, at energies from 1 keV to 100 GeV [1].

The cross-section can be defined as the probability of an interaction to occur, it has the dimension of area in units of barn abbreviated $b = 10^{-28}\,m^2 = 10^{-24}\,cm^2 = 100 fm^2$.

There are different kinds of cross-sections; atomic, molecular and electronic cross-sections, the atomic cross-section for an element of atomic weight A is given by:

$$\sigma_a = \frac{\mu}{\rho}\frac{A}{N_{av}} \qquad (7)$$

N_{av} represents the Avogadro's number.

For a compound the molecules of which have n_i atoms for the i-th element, the atomic or molecular cross-sections are given by:

$$\sigma_a = \frac{\mu}{\rho}\sum_i \frac{n_i A_i}{\sum n_i}\frac{1}{N_{av}} \qquad (8)$$

The electronic cross-section for an element is given by:

$$\sigma_e = \frac{\sigma_a}{Z} \qquad (9)$$

Hence, for the compound, the electronic cross-section is:

$$\sigma_e = \frac{1}{N_{av}}\sum_i (\frac{f_i A_i}{Z_i})(\frac{\mu}{\rho})_i \qquad (10)$$

where f_i ($= n_i/\sum n_j$) is the fractional abundance of element i, with respect to the total number of atoms. Z_i is the atomic number of the element.

The effective atomic number (Z_{eff}) is a property for a compound, it describes the properties of the composite materials in terms of equivalent elements, it represents the weighted average atomic number of the compound composed of different materials, the average is weighted according to the relative number of each type of atom, Z_{eff} value of a material varies within a range with lowest and highest atomic numbers of its constituent elements [7].

The effective atomic number is equal to:

$$Z_{eff} = \frac{\sigma_a}{\sigma_e} = \frac{\sum_i n_i \sigma_i}{\sum_i n_i \frac{\sigma_i}{Z_i}} = \frac{\sum_i f_i A_i (\frac{\mu}{\rho})_i}{\sum f_i \frac{A_i}{Z_i} (\frac{\mu}{\rho})_i} \qquad (11)$$

The electron density can be defined as the number of electrons per unit mass, and it can be mathematically written as:

$$N_{el} = \frac{(\frac{\mu}{\rho})_c}{\sigma_e} \qquad (12)$$

where N_{el} represents the electron density in unit of electron/gram, $(\mu/\rho)_c$ is the compound mass attenuation coefficient and σ_e is the electronic cross-section.

Experimental Procedure:

Transmission experiments with the narrow beam (good-geometry) setup were used for measuring the incident and transmitted intensities, and hence calculating the attenuation coefficient. Further calculations of the cross sections (atomic, electronic and molecular), effective atomic numbers and electron densities were performed.

Two gamma sources were used in these experiments so that the above parameters were studied at three different energies. Table 1 displays the properties of the gamma sources used in this experiment.

The five sample materials were shaped each in five square slices, for measuring the attenuation, these five slices are stacked one by one on the detector, the intensities of the transmitted photons were determined by choosing the counting time as 100 minutes, counts were recorded under the photo peaks, ad statistical uncertainty was kept as low as possible, Henceforth, different thickness is achieved each time. The dimensions of the samples were measured with a vernier caliper. Then the samples were weighted with a digital balance, and the density was calculated.

TABLE 1. The gamma source description.

Gamma-ray source	Half-life (days)	Activity (µCi) (Production date 1999)	Energy (MeV)	Count rate at aperture (count/sec)
^{137}Cs	11012	0.9508	0.6616	12.2
^{60}Co	1923	1.016	1.173	9.0
^{60}Co	1923	1.016	1.332	9.0

TABLE 2. The sample description.

Sample	Chemical composition	Dimensions (cm) Length ×Width ×Thickness	Average mass (g)	Average density (g/cm^3)
Aluminum	Al	3.95 × 5.69 × 0.51	30.75	2.68 ± 0.016
Perspex	$C_5H_8O_2$	5.17 × 5.07 × 0.45	13.31	1.12 ± 0.022
PVC (Poly-Vinyl Chloride)	C_2H_3Cl	5.08 × 5.03 × 0.51	17.61	1.34 ± 0.014
Iron	Fe	5.00 × 5.00 × 0.20	37.45	7.49 ± 0.34
Brass	Cu_3Zn_2	5.10 × 5.11 × 0.21	43.73	7.85 ± 0.36

The experiment was performed at the Radiation Measurement Laboratory at Al- Balqa Applied University. The gamma rays are well collimated using two collimators; one at the source and the other at the detector. Each of the collimators has a cylindrical shape and a circular aperture. The signal is detected by NaI (Tl) scintillation detector of a (3×3 inch) crystal and a high bias voltage of 1000 volts. A lead shield surrounds the detector to reduce the undesired external radiation. Fig. 1 below shows the system setup, the source collimator and the lead shield in which the detector is embedded.

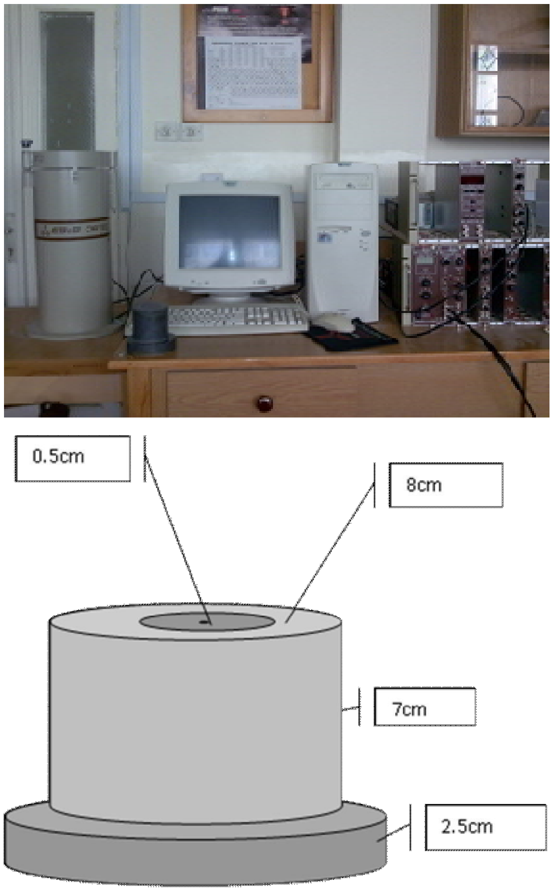

FIG. 1. The experimental setup and the source collimator dimensions.

The weak detector pulse enters the preamplifier (or preamp.). The pulse then enters the linear amplifier which has two main functions; pulse shaping and amplitude gain, for which the multi-channel analyzer has been designed. The amplified pulse is then fed to the Multi-Channel Analyzer (MCA), which converts the analog signal into a digital number through an analog to digital converter (ADC), in this case the software is used to control the MCA functions and other settings, in this experiment Senti-vision was used to analyze the spectrum. The energy and the efficiency of the system were calibrated using a certified standard source from the International Atomic Energy Agency (IAEA).

Results and Discussion

The linear attenuation coefficient quantity (μ) is determined by measuring the incident photons intensity (I_0) and the intensity (I) of the photons after passing through samples with thickness (x), a graph of $\ln(I_0/I)$ versus thickness (x) is drawn, a linear relation appears, each linear graph is fitted by linear fit method, the slope of the linear fit equation represents the value of the linear attenuation coefficient.

From the graphs, it is clear that the linear attenuation coefficient is inversely proportional to energy, and that's related to the dependency of the linear attenuation coefficient on the interaction between photons and matter, when the photons energy increases, the transmitted photons increase and the absorbed photons decrease, as a result the linear attenuation coefficient decreases.

Another definition which is associated with linear attenuation coefficient is the mean free path, it represents the distance between successive interactions. Mathematically, it is the inverse of the linear attenuation coefficient, the direct relation between it and energy is found, and it explains why the number of interactions becomes higher when the distance between the interactions gets smaller.

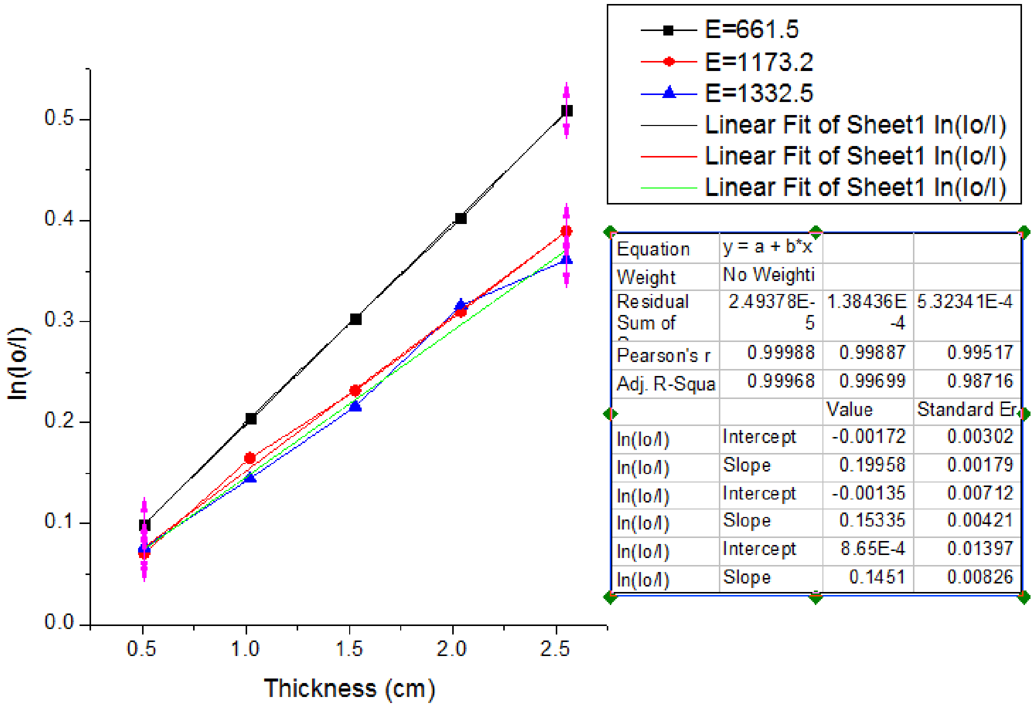

Equation	y = a + b*x		
Weight	No Weighti		
Residual Sum of	2.49378E-5	1.38436E-4	5.32341E-4
Pearson's r	0.99988	0.99887	0.99517
Adj. R-Squa	0.99968	0.99699	0.98716
		Value	Standard Er
ln(Io/I)	Intercept	-0.00172	0.00302
ln(Io/I)	Slope	0.19958	0.00179
ln(Io/I)	Intercept	-0.00135	0.00712
ln(Io/I)	Slope	0.15335	0.00421
ln(Io/I)	Intercept	8.65E-4	0.01397
ln(Io/I)	Slope	0.1451	0.00826

FIG. 2. Linear attenuation coefficient of Al at (a) 661.6 keV, (b) 1173.2 keV and (c) 1332.5 keV.

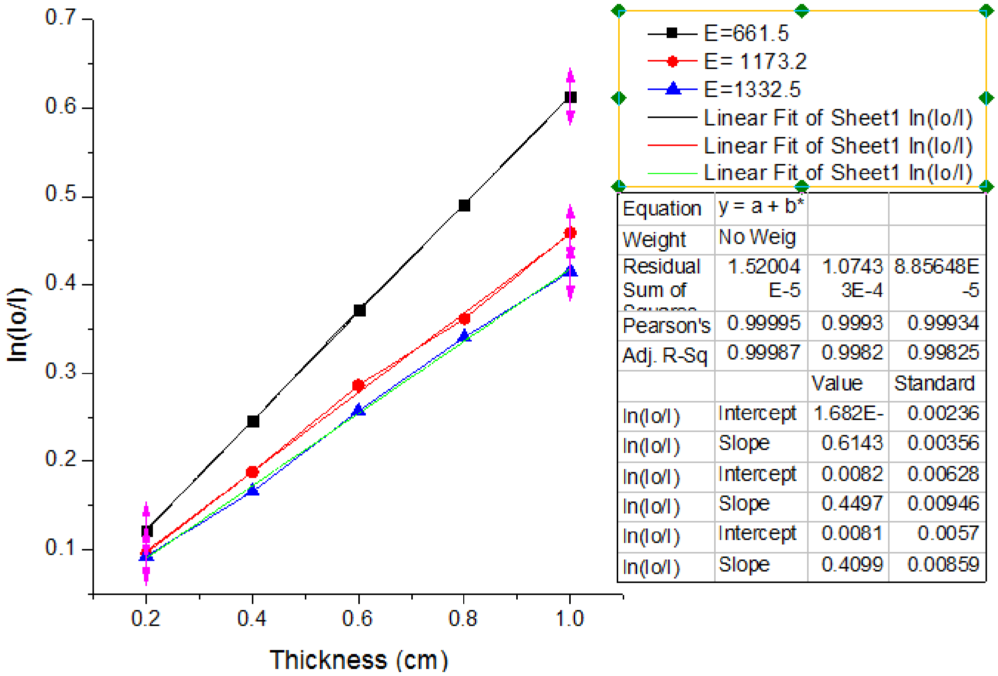

Equation	y = a + b*		
Weight	No Weig		
Residual Sum of	1.52004E-5	1.07433E-4	8.85648E-5
Pearson's	0.99995	0.9993	0.99934
Adj. R-Sq	0.99987	0.9982	0.99825
		Value	Standard
ln(Io/I)	Intercept	1.682E-	0.00236
ln(Io/I)	Slope	0.6143	0.00356
ln(Io/I)	Intercept	0.0082	0.00628
ln(Io/I)	Slope	0.4497	0.00946
ln(Io/I)	Intercept	0.0081	0.0057
ln(Io/I)	Slope	0.4099	0.00859

FIG. 3. Linear attenuation coefficient of brass at (a) 661.6 keV, (b) 1173.2 keV and (c) 1332.5 keV.

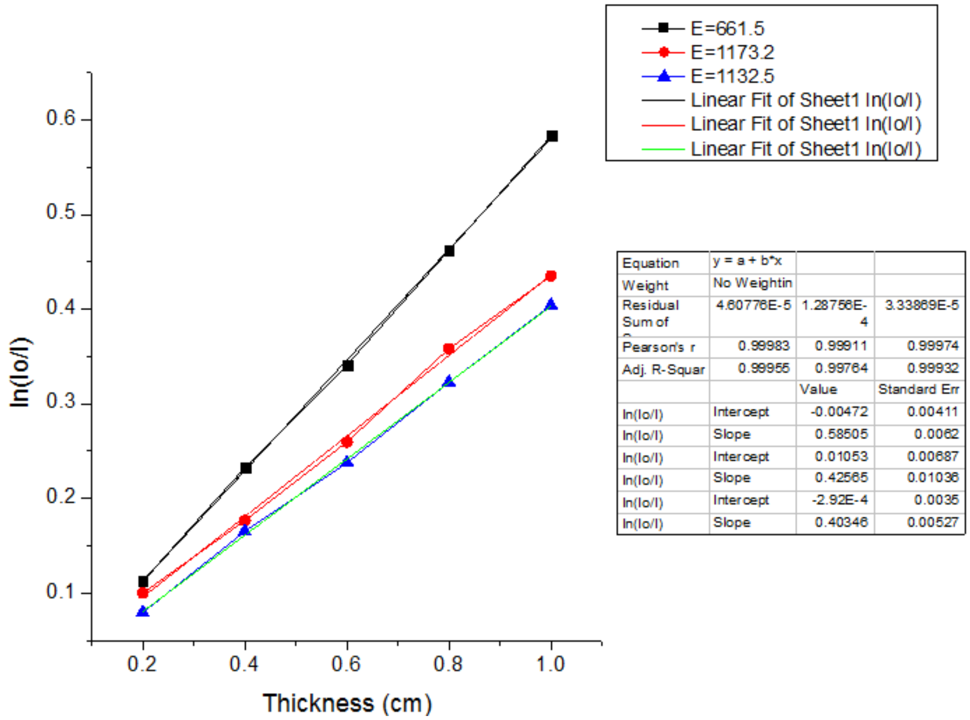

Equation	y = a + b*x		
Weight	No Weightin		
Residual Sum of S	4.60776E-5	1.28756E-4	3.33869E-5
Pearson's r	0.99983	0.99911	0.99974
Adj. R-Squar	0.99955	0.99764	0.99932
		Value	Standard Err
ln(Io/I)	Intercept	-0.00472	0.00411
ln(Io/I)	Slope	0.58505	0.0062
ln(Io/I)	Intercept	0.01053	0.00687
ln(Io/I)	Slope	0.42565	0.01036
ln(Io/I)	Intercept	-2.92E-4	0.0035
ln(Io/I)	Slope	0.40346	0.00527

FIG. 4. Linear attenuation coefficient of Fe at (a) 661.6 keV, (b) 1173.2 keV and (c) 1332.5 keV.

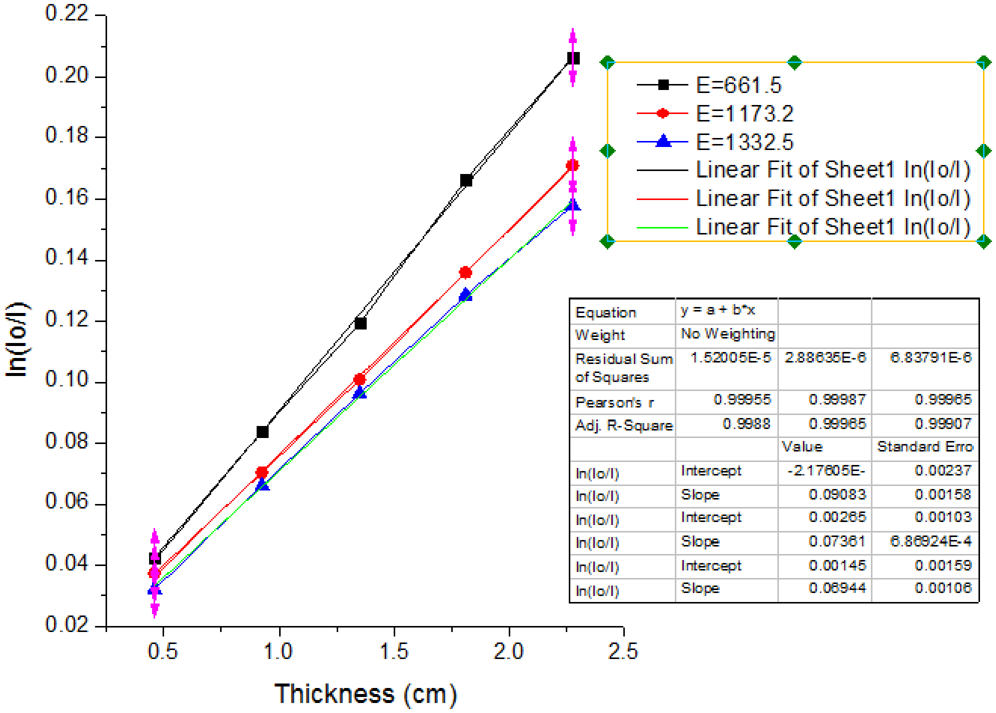

Equation	y = a + b*x		
Weight	No Weighting		
Residual Sum of Squares	1.52005E-5	2.88635E-6	6.83791E-6
Pearson's r	0.99955	0.99987	0.99965
Adj. R-Square	0.9988	0.99965	0.99907
		Value	Standard Erro
ln(Io/I)	Intercept	-2.17605E-	0.00237
ln(Io/I)	Slope	0.09083	0.00158
ln(Io/I)	Intercept	0.00265	0.00103
ln(Io/I)	Slope	0.07361	6.86924E-4
ln(Io/I)	Intercept	0.00145	0.00159
ln(Io/I)	Slope	0.06944	0.00106

FIG. 5. Linear attenuation coefficient of perspex at (a) 661.6 keV, (b) 1173.2 keV and (c) 1332.5 keV.

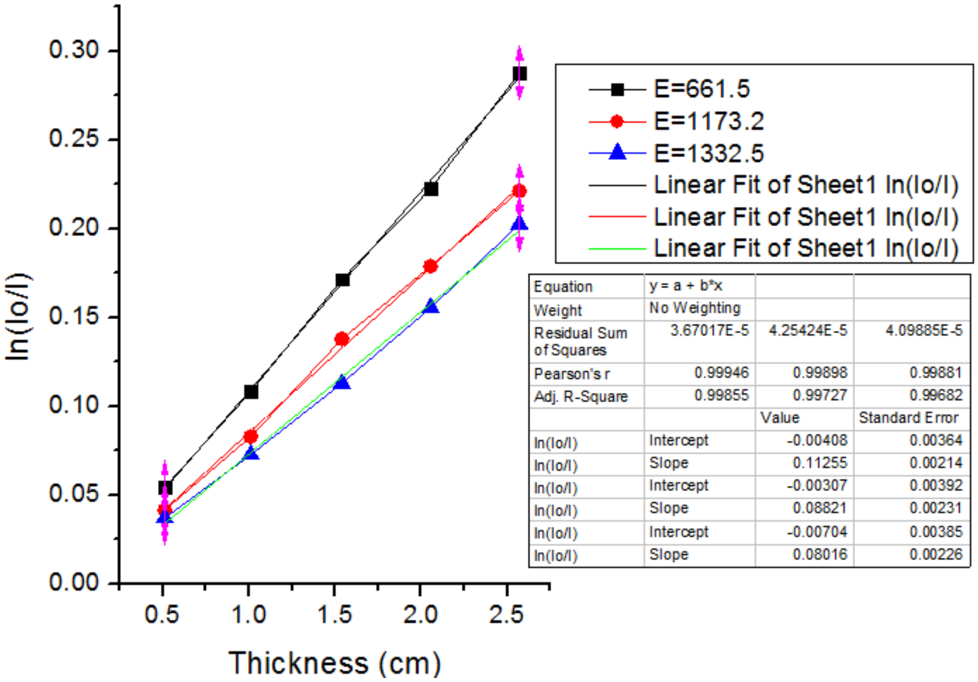

FIG. 6. Linear attenuation coefficient of PVC at (a) 661.6 keV, (b) 1173.2 keV and (c) 1332.5 keV.

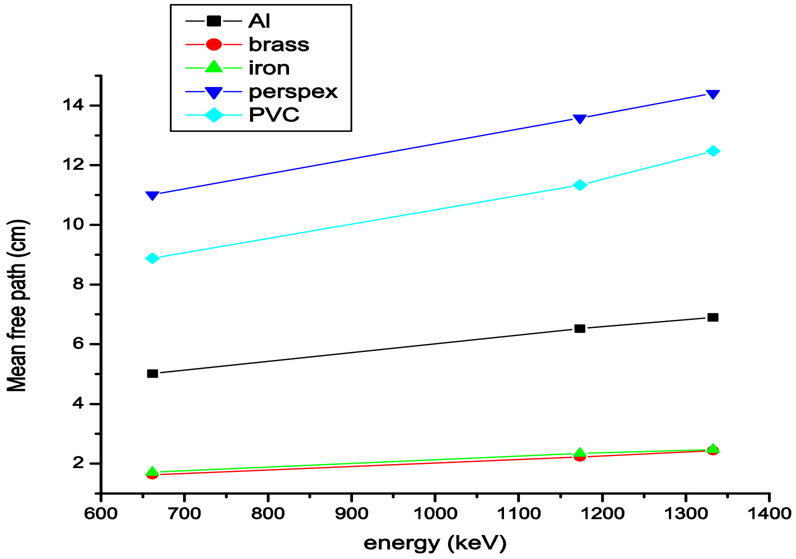

FIG. 7. The mean free path for all samples at different energies.

TABLE 3. The linear attenuation coefficients and mean free path for the samples.

Sample	Linear attenuation coefficient (cm^{-1})			Mean free path(cm)		
	661.6 keV	1173.2 keV	1332.5 keV	661.6 keV	1173.2 keV	1332.5 keV
Aluminum	0.1991	0.1530	0.1448	5.020	6.530	6.906
Iron	0.5850	0.4256	0.4034	1.709	2.349	2.478
Brass	0.6143	0.4497	0.4099	1.628	2.223	2.439
Perspex	0.0908	0.0736	0.0694	11.013	13.586	14.409
PVC	0.1125	0.0882	0.0801	8.884	11.336	12.475

In this experiment, the samples are chosen to make a comparison between pure elements (Al, Fe), thermoplastic materials (PVC, Perspex) and alloy which is represented by Brass. It's found that brass (the alloy) is a good absorber and then come pure elements but thermoplastic materials are not, from this arrangement the dependency of the linear attenuation on density is obvious, if we normalize the linear attenuation by the absorber density. Hence, the mass attenuation coefficient (μ_m) is defined.

From the tables, it is observed that, as the density increases the mass attenuation coefficient decreases; this confirms the contribution of the absorption process (photoelectric effect), scattering process (Compton, coherent) and pair production.

The experimental results for mass attenuation coefficients are compared with the XCOM data base and mixture rule, the results are close to each other, and Table (4) below clarifies that.

TABLE 4. The mass attenuation coefficients of the samples at different energies

Sample	^{137}Cs data (661.6 keV)				^{60}Co data(1173.2 keV)			
	$(\mu/\rho)_{XCOM}$ (cm^2/g)	$(\mu/\rho)_{exp}$ (cm^2/g)	$(\mu/\rho)_{mix}$ (cm^2/g)	error%	$(\mu/\rho)_{XCOM}$ (cm^2/g)	$(\mu/\rho)_{exp}$ (cm^2/g)	$(\mu/\rho)_{mix}$ (cm^2/g)	error%
PVC	0.079	0.082	0.079	2.8	0.060	0.063	0.060	6.0
Perspex	0.083	0.079	0.083	5.2	0.063	0.064	0.063	0.80
Aluminum	0.074	0.073	-	1.3	0.056	0.057	-	3.5×10^{-3}
Brass	0.072	0.073	0.072	0.2	0.054	0.053	0.054	1.8
Iron	0.073	0.074	-	1.0	0.055	0.054	-	2.3

Sample	^{60}Co data(1332.5 keV)			
	$(\mu/\rho)_{XCOM}$ (cm^2/g)	$(\mu/\rho)_{exp}$ (cm^2/g)	$(\mu/\rho)_{mix}$ (cm^2/g)	error%
PVC	0.056	0.058	0.056	2.8
Perspex	0.059	0.063	0.059	1.4
Aluminum	0.053	0.054	-	7.5×10^{-3}
Brass	0.051	0.048	0.051	4.5
Iron	0.051	0.051	-	1.2

Trials are made to make a relation between mass attenuation coefficient and energy. First, suppose that the mass attenuation coefficient can be written as [15]:

$$\mu_m = AE^{-B} \tag{13}$$

Take the logarithm for both sides:

$$\ln \mu_m = \ln A - B \ln E \tag{14}$$

This relation represents a straight line with slope ($-B$) and intercepts ln (A).

The linear attenuation coefficient can be written as:

$$\mu = \rho A E^{-B} \tag{15}$$

The equations that represent the relations between linear attenuation coefficient and energy for samples can be known after finding the constants which are:

$$\left.\begin{array}{l} \text{For Al } \mu = 3.86181E^{-0.4567} \\ \text{For Fe } \mu = 19.42989E^{-0.5396}. \\ \text{For Brass } \mu = 24.4989E^{-0.5673}. \\ \text{For PVC } \mu = 2.350692E^{-0.4673} \\ \text{For Perspex } \mu = 1.23073E^{-0.3802} \end{array}\right\} \tag{16}$$

The previous relations represent a generalization of the samples to find the linear attenuation coefficient at any energy.

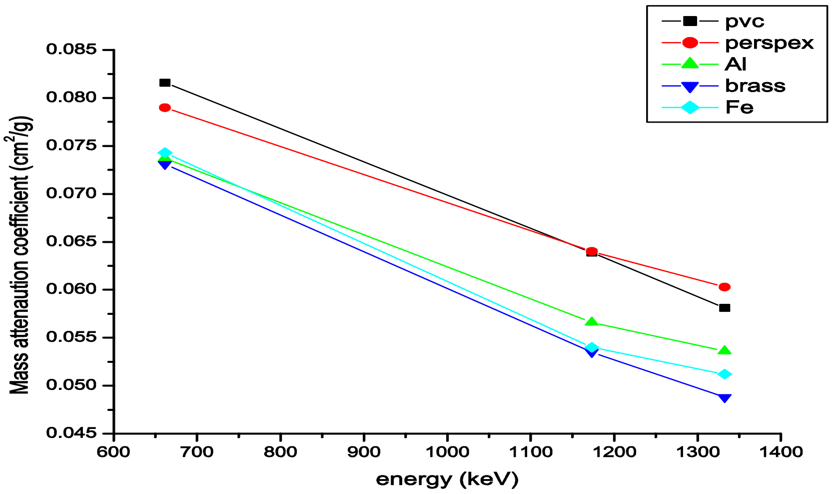

FIG. 8. Mass attenuation coefficient versus energy for all samples.

Another important parameter that affects the transmission photons is cross-section (atomic, molecular and electronic cross-section), which has an inverse relation with energy and is associated with the mean free path definition.

Atomic cross-section which is represented by Al and Fe in this experiment, has linear relationships with atomic weight and mass attenuation coefficient, the atomic weight for Al is 26.98 while for Fe is 55.8 with a difference equal to 28.82, for this reason iron has a higher value of atomic cross-section than Al, although Al has a higher mass attenuation coefficient.

Turning to the compounds, the molecular cross-section plays an important role in the interaction between photons and matter, if we assume that the molecular cross-section is related to the molecular weight and energy by the expression:

$$\sigma_m = kAE^b \tag{17}$$

where k and b are constants, then we have:

$$\ln(\sigma_m/A) = b\ln(E) + \ln(k) \tag{18}$$

This is a straight line of slope b and intercepts ln (k). The numerical values of k and b are given under the assumption that the energy is expressed in units of keV, the atomic weight in gmol^{-1} and the molecular cross-section in barn/molecule. The straight line fitting yields the values of b, ln (k), the equation of the molecular cross-section is;

$$\sigma_m = 3.62879\times 62.4967\, E^{-0.51}$$

$$\sigma_m = 1.21191\times 100.1112\, E^{-0.3418}$$

$$\sigma_m = 3.14842\times 321.398\, E^{-0.5009}$$

Brass molecules have the highest probability of interaction, then Perspex, but PVC molecules have low interaction probability, the explanation of this result is related to the large difference of the molecular weight, for brass it equals 321.398 comparing with Perspex which has a molecular weight of 100.1112, but for PVC the molecular weight is only 62.4967.

Due to the size of the atoms which compose the compounds, Cu and Zn of brass are sufficiently large so the electrons in the last shell are fewer bands to the nucleus; this point increases the interaction probabilities, comparing with H-atom, C-atom, O-atom and Cl- atom in Perspex and PVC, which seem small relative to Cu and Zn.

Molecular cross-section is also found by using Eq. 8, the comparison between the results of the two methods is made, and the results are almost compatible.

The last definition in cross-sections is electronic cross-section, for the compounds brass has the largest value. However, PVC and Perspex are approximately close to each other, with a small difference between them; PVC has a greater value than Perspex; attributed to the existence of chlorine (Z = 17, A = 35.45) in PVC which is a little greater than Oxygen (Z = 8, A = 17) in Perspex, although oxygen has a higher value of mass attenuation coefficient.

TABLE 5. The atomic and electronic cross-sections of the pure elements.

Sample	661.6 keV		1173.2 keV		1332.5 keV	
	$\sigma_a \times 10^{-24}$	$\sigma_e \times 10^{-25}$	$\sigma_a \times 10^{-24}$	$\sigma_e \times 10^{-25}$	$\sigma_a \times 10^{-24}$	$\sigma_e \times 10^{-25}$
Al	3.282 ± 0.02090	2.525 ± 0.01869	2.509 ± 0.3849	1.930 ± 0.04606	2.414 ± 0.05086	1.863 ± 0.03643
Fe	6.770 ± 0.04413	2.639 ± 0.02471	5.318 ± 0.1481	2.045 ± 0.05696	4.742 ± 0.03508	1.824 ± 0.01348

TABLE 6. The molecular and electronic cross-sections of the samples.

Sample	σ_m from fitting equation (barn/molecule)			σ_m from equation(8) $\times(10^{-23})$ (cm^2/molecule)			$\sigma_e \times 10^{-25}$		
	661.6 keV	1173.2 keV	1332.5 keV	661.6 keV	1173.2 keV	1332.5 keV	661.6 keV	1173.2 keV	1332.5 keV
Brass	8.263	6.169	5.781	3.902 ± 0.01183	2.969 ± 0.03301	2.72712 ± 0.05688	2.644	2.563	2.566
Perspex	13.18	10.84	10.37	1.313 ± 0.009970	1.105 ± 0.04710	1.021 ± 0.005850	1.977	1.956	1.957
PVC	39.11	29.36	27.54	0.8204 ± 0.08318	0.6411 ± 0.11566	0.5602 ± 0.09432	1.856	1.827	1.828

Note: σ_a has a unit of (cm^2/atom), σ_m is in barn/molecule and σ_e is in (cm^2/electron).

Table 7. The effective atomic number and electron density of the samples.

Sample	$Z_{\text{effective}}$ from constituents			$Z_{\text{effective}}$ from equation (11)			Electron density		
	661.6 keV	1173.2 keV	1332.5 keV	661.6 keV	1173.2 keV	1332.5 keV	661.6 keV	1173.2 keV	1332.5 keV
Brass	29.49± 0.08426	29.99 ± 0.3222	29.39± 0.5959	29.50 ± 0.09154	30.04 ± 0.3351	29.39 ± 0.6129	2.763± 0.007890	2.809± 0.03018	2.754 ± 0.05582
Perspex	3.414 ± 0.02716	3.783 ± 0.06115	3.715 ± 0.02128	3.415 ± 0.02718	3.766 ± 0.06077	3.724 ± 0.02133	3.080 ± 0.02451	3.413± 0.05518	3.352 ± 0.01921
PVC	5.311 ± 0.05371	5.470 ± 0.09854	5.083 ± 0.08546	5.329 ± 0.05403	5.387 ± 0.1139	5.109 ± 0.08519	3.070 ± 0.03104	3.162± 0.05696	2.939 ± 0.04942

After finding the cross-section of the samples, the calculation of effective atomic number $Z_{\text{effective}}$ and electron density becomes possible, by using Eq. 11, the results are arranged in the table above.

There is another method for determining effective atomic numbers and electron densities. These have been determined by matching the atomic cross-section with the corresponding values of the elements of the compound at a given energy. In other words, the effective atomic number for each sample was determined by using the atomic cross-section for the compound constituents.

Since the mass attenuation coefficients for each individual element in the compound for the energies 661.6, 1173.2 and 1332.5 keV are not available experimentally, these attenuations were taken from the XCOM data base, assuming that the elemental cross-section can be written as [6]:

$$\sigma = A(Z)E^{B(Z)} \tag{19}$$

Since this cross-section shows a non-linear relation with energy E and atomic number Z; $A(Z)$ and $B(Z)$ are constant with respect to energy. Taking the logarithm for both sides of the previous equation gives:

$$\ln \sigma = \ln A(Z) + B \ln E \qquad (20)$$

This equation represents a straight line with slope $B(Z)$ and intercepts ln ($A(Z)$). The linear fit is taken to determine the values of $B(Z)$ and ln ($A(Z)$). Since ln ($A(Z)$) and $B(Z)$ are simple functions of the atomic number, it is assumed that it can be written as [6]:

$$\ln A(Z) = \ln A_1 + B_1 \ln Z$$

and

$$B(Z) = \ln A_2 + B_2 \ln Z \qquad (21)$$

These equations also represent straight lines with slopes B_1 and B_2 and intercept ln (A_1) and ln (A_2), respectively. All of the previous coefficients are constants and can be determined using the linear fit method.

The formula that can be used to determine the effective atomic number in this case is:

$$Z_{eff} = [\frac{\sigma_{compound}}{A_1 E^{\ln A_2}}]^{1/d} \qquad (22)$$

where

$$d = B_1 + B_2 \ln E \qquad (23)$$

The electron density can also be calculated using the formula:

$$N_{el} = N_{av} Z_{eff} \frac{\sum_i n_i}{\sum_i n_i A_i} \qquad (24)$$

Theoretically, the variation of energy makes a difference in the effective atomic number. In general, that is not clear here in this experiment, where the effective atomic numbers for different energies are very close to each other. This is attributed to the Compton scattering which is dominant in this range of energy. Although we take the net area under the photo peak, Compton scattering cross-section has a Z-dependence, where it is proportional to Z^1 as $\sigma_{compton} \propto Z$. Therefore, the effective atomic number is constant in this energy range.

Comparing the three compounds in terms of the effective atomic number, we find that Brass has the highest value, then PVC, and Perspex is the last one. The reason of this order is the kind of atoms in each compound, the atomic numbers of the constituents affect the atomic number of the compound, Cu (Z = 29) and Zn (Z = 30) in Brass, have atomic numbers higher than carbon (Z = 6), hydrogen (Z = 1) and oxygen (Z = 8) in Perspex. In PVC, in addition to carbon and hydrogen, there is chlorine (Z = 17), so there is a large difference between the constituents of Perspex and PVC relative to those of Brass. However, a reverse order is found for electron density because of the big difference in the atomic weight of the compounds.

Conclusion

Attenuation coefficients of the samples have been measured, using collimated gamma ray transmission method, the other factors; cross-sections, effective atomic numbers and electron densities; have been calculated with respect to the mass attenuation coefficients.

From the analysis, brass appears as a good attenuator, and the inverse relation between energy and gamma attenuation clearly appears. The cross-sections for the ^{60}Co lines 1173.2 keV and 1332.5 keV are very close to each other, which means the probability of interaction is approximately the same. On the other hand, the effective atomic numbers for the samples are found to be constant; also the effective atomic number and electron density of composite material give an indication of their atomic composition.

Acknowledgments

The authors like to extend their gratitude to the Scholar Rescue Fund (SRF) for their support.

References

[1] Kaewkhao, J., Laopaiboon, J. and Chewpraditkul, W., J. Quant. Spectrosc. Ra. 109 (2008) 1260.

[2] Murty, V., Rad. Phy. and Chorn. 21 (2004) 667.

[3] Sabriye, S., Karahan, H. and Őmer, F., J. Quant. Spectrosc. Ra. 83 (2004) 237.

[4] Manohara, S.R. and Hanagodimath, S.M., Nucl. Instrum. Methods. B, 258 (2007) 321.

[5] Shivalinge, G., Krishnaveni, S. and Ramakrishna, G., Nucl. Instrum. Methods B, 239 (2005) 369.

[6] Shivalinge, G., Skrishnaveni, Y., Umesh, T.K. and Ramakrimshna, G., Pramana –J. Phys. 63 (2004) 529.

[7] Baltas, H. and Cevik, U., Nucl. Instrum. Methods B, 266 (2008) 1127.

[8] Awadallah, M.I. and Imran, M.M., J. Environ. Radioactiv. 94 (2007) 129.

[9] Kiran, K. and Venkata, K.R., Radiat. Phys. Chem. 50 (1997) 545.

[10] Manohara, S.R., Hanagodimath, S.M. and Gerward, L., Phys. Med. Biol. 53 (2008) 377.

[11] Manjunathaguru, V. and Umesh, T., J. Phys. B- At. Mol. Opt. 39 (2006) 3969.

[12] Kaliman, Z., Orlic, N. and Jelovica, I., Nucl. Instrum. Methods A, 580 (2007) 40.

[13] Hendee, R. and Ritenour, E.R., Medical Imaging Physics, 4th Ed. (John Wiley and Sons, New York, 2005).

[14] Morgan, C.L., Basic Principles of Computed Tomography, (University Park Press, Baltimore, 1983), Chapter 2.

[15] Awadallah, M.I., Ph.D. Thesis, University of Jordan, (2003), Amman, Jordan (Unpublished).

[16] Thangaraju, B. and Kaliannan, B., J. Cryst. Res.Technol., 35 (2000) 71.

[17] Habubi, N.F., Mishjal, K.H. and Ziad, T.K., Journal of College Education, Al-Mustansyriah University, (2002).

[18] Omar, A.M., Elementary Solid State Physics, (Addison-Wesley Publishing Company, First Printing, 1975).

[19] Banerjee, A.N., Ghosh, C.K., Das, S. and Chattopadhyay, K.K., Physica, 370 (2005) 264.

[20] Stenzel, O., The Physics of Thin Film Optical Spectra, (Springer-Verlag, Berlin, Heidelberg , Germany Press, 2005).

[21] Islam, M.R. and Podder, J., Cryst. Res. Technol., 44(3) (2009) 286.

[22] Singh, J., Semiconductor Optoelectronics Physics and Technology, (McGraw-Hill, Inc., 1995).

[23] Dekker, A.J., Solid State Physics (Prentice Hall, Inc., 1958).

[24] Ali, H.M., Mohamed, H.A., Wakkad, M.M. and Hasaneen, M.F., Thin Solid Films, 515.

[25] Al-Sabayleh, M.A., J. Sci. Med., 20(1) (2008) 17.

[26] Khodair, Z.T., Ph.D. thesis, University of Baghdad, College of Education-Ibn Al-Haithem (2011).

الجدول (3): بعض قيم معامل الانكسار لأغشية ZnO النقية والمشوبة بالنحاس.

معامل الانكسار عند الطول الموجي (380 nm)	الغشاء ونسبة الإشابة
2.639	*ZnO*
2.376	*ZnO:Cu (3%)*
2.368	*ZnO:Cu (5%)*
2.258	*ZnO:Cu (7%)*
2.189	*ZnO:Cu(9%)*

الاستنتاجات

تم التوصل في هذا البحث إلى الاستنتاجات الآتية:

- إمكانية تحضير أغشية أوكسيد الخارصين باستخدام طريقة APCVD ضمن ظروف التحضير الجديدة.
- غشاء أوكسيد الخارصين من النوع متعدد التبلور، وقد أدت إضافة الشوائب ضمن النسب العالية إلى إزاحة قليلة في منحني الطيف نحو القيم العالية لزاوية الحيود.
- طبيعة الانتقالات الإلكترونية لجميع الأغشية كانت انتقالات الكترونية مباشرة ممسوحة ومباشرة ممنوعة.
- فجوة الطاقة للانتقالات الإلكترونية المباشرة المسموحة والممنوعة تقل بزيادة نسب التشويب لجميع الأغشية المشوبة بالنحاس.
- التشويب بالنحاس أدى إلى تغير موقع قمة منحني الانعكاسية ومعامل الانكسار باتجاه الطاقات الفوتونية الواطئة مما يدل على زيادة الامتصاصية.
- معامل الخمود يتزايد في حالة الأغشية المشوبة بسبب زيادة معامل الامتصاص.

المراجع

[1] Adachi, S., Properties of Group -IV,III-V & II-VI Semiconductors, (John Wiley and Sons Ltd., 2005).

[2] Sharma, R., Shishodia, P.K., Wakahara, A. and Mehra, R.M., Material Science-Poland, 27(1) (2009) 225.

[3] Shan, F.K., Shin, B.C., Jang, S.W. and Yu, Y.S., Journal of the European Society, 24 (2004) 1015.

[4] Oztas, M. and Bedir, M., Thin Solid Films, 516 (2008) 1703.

[5] Yi, G.-C. and Wang, C., Semicond. Sci. Technol., 20 (2005) S22.

[6] Johnson, S.E. and Owen, J.R., Journal of Physics, 5(11) (1995) 871.

[7] Kumar, R. and Khare, N., Thin Solid Films, 516 (2008) 1302.

[8] Jeong, S.H., Park, B.N. and Lee, S.B., J.-H., Surface and Coatings Technology, 193 (2005) 340.

[9] Ismail, R.A., Al-Naimi, A. and Al-Ani, A.A., e-J. Surf. Sci. Nanotech., 4 (2006) 636.

[10] Elanchezhiyan, J., Shin, B.C., Lee, W.J., Park, S.H. and Kim, S.C., Cryst. Res. Technol., 44(12) (2009) 1319.

[11] Xiaming, Z., Huizhen, W., Shuangjiang, W., Yingying, Z., Chunfeng, C., Jianxiao, S., Zijian, Y., Xiaoyang, D. and Shurong, D., Journal of Semiconductors, 30(3) (2009) 1.

[12] Table of Periodic Properties of the Elements, Sargent-Welch Scientific Company.

[13] Ilican, S., Caglar, M., Caglar, Y. and Demirci, B., Journal of Optoelectronics and Advanced Materials, 10(10) (2008) 2592.

[14] Caglar, Y., Zor, M., Caglar, M. and Ilican, S., Journal of Optoelectronics and Advanced Materials, 8(5) (2006) 1867.

[15] Caglar, M., Caglar, Y. and Ilican, S., Journal of Optoelectronics and Advanced Materials, 8(4) (2006) 1410.

وعند الطاقات المنخفضة تقترب قيمة k_0 من الصفر تقريبًا، لذلك يمكن كتابة المعادلة (10) بالصيغة التالية [25]:

$$n_o = \frac{1+\sqrt{R}}{1-\sqrt{R}} \qquad (11)$$

الشكل (9) يمثل تغير معامل الانكسار كدالة للطول الموجي لغشاء أوكسيد الخارصين النقي؛ إذ نلاحظ أن طبيعة منحني معامل الانكسار مشابهة تقريبًا لطبيعة منحني الانعكاسية نظراً لارتباط (R) مع (n_o) وفقاً للعلاقة (5)، وأن أعلى قيمة يصلها معامل الانكسار تكون مقابلة لقيمة فجوة الطاقة تقريباً، أما عند التشويب فنلاحظ أن أعلى قيمة يصلها معامل الانكسار تنحرف نحو الطاقات الفوتونية المنخفضة، والجدول (3) يبين قيمة معامل الانكسار لجميع الأغشية بثبات الطول الموجي.

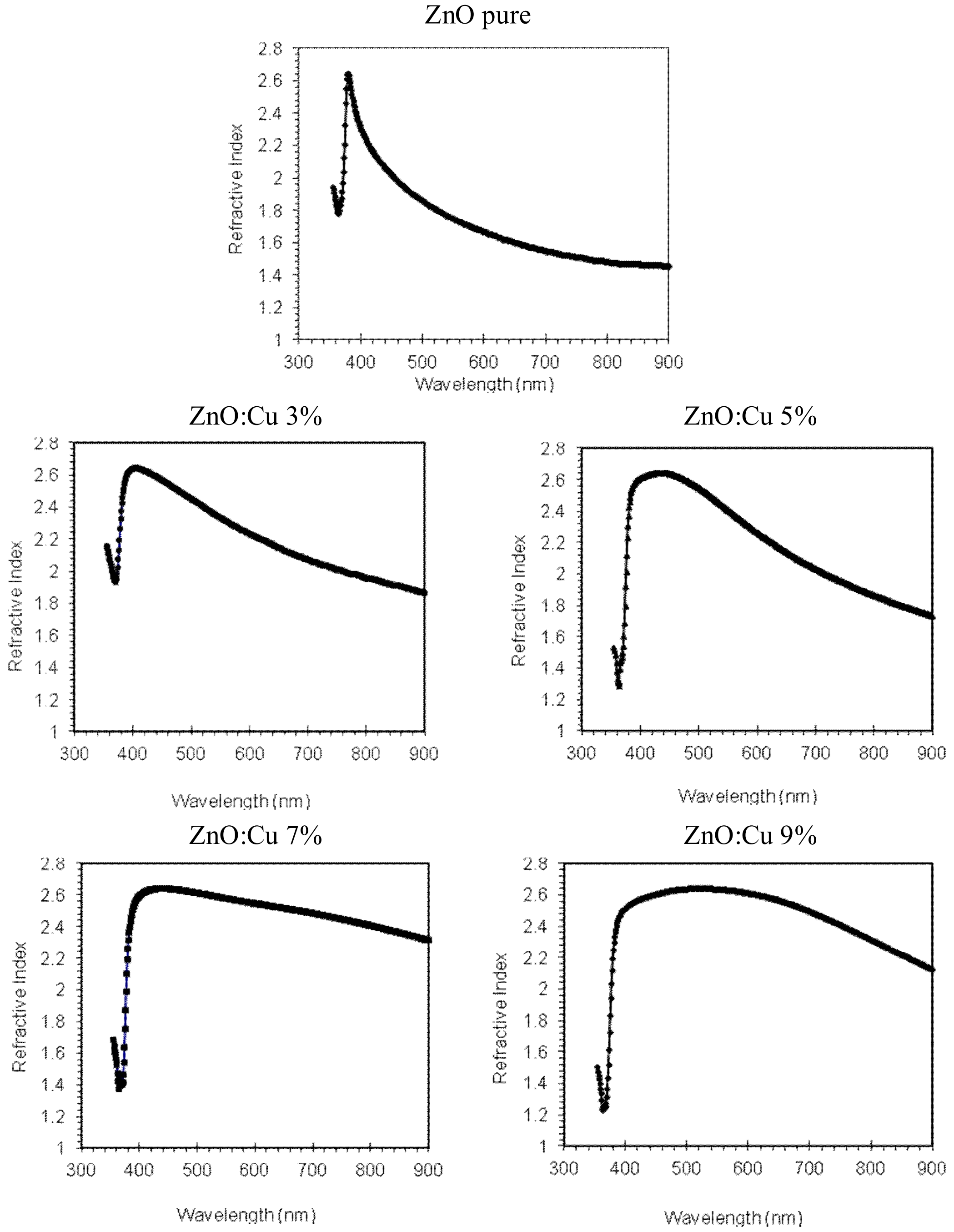

ZnO pure

ZnO:Cu 3%

ZnO:Cu 5%

ZnO:Cu 7%

ZnO:Cu 9%

الشكل (9): تغير معامل الانكسار كدالة للطول الموجي لأغشية أوكسيد الخارصين النقية والمشوبة ولنسب مختلفة.

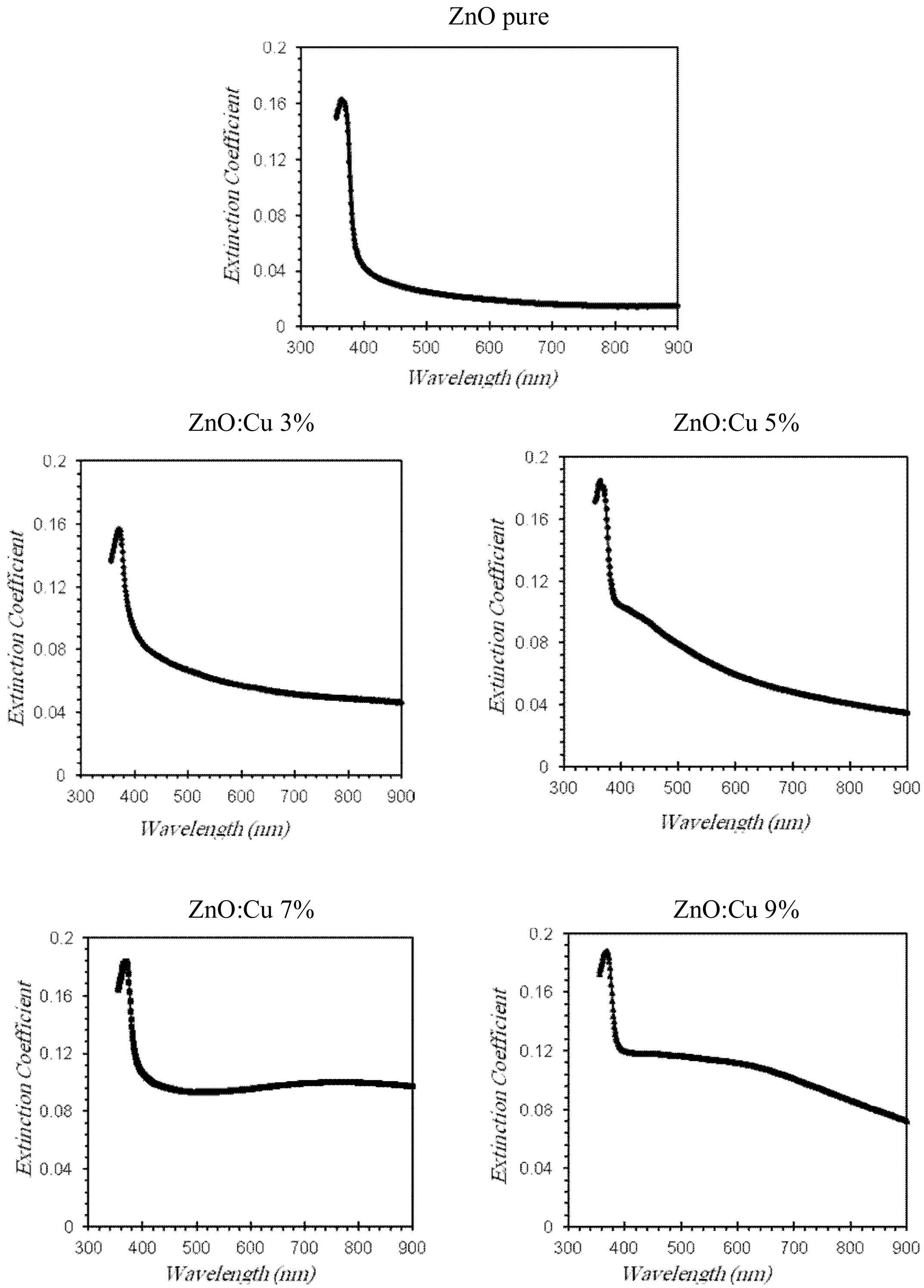

الشكل (8): تغير معامل الخمود كدالة للطول الموجي لأغشية أوكسيد الخارصين النقية والمشوبة ولنسب مختلفة.

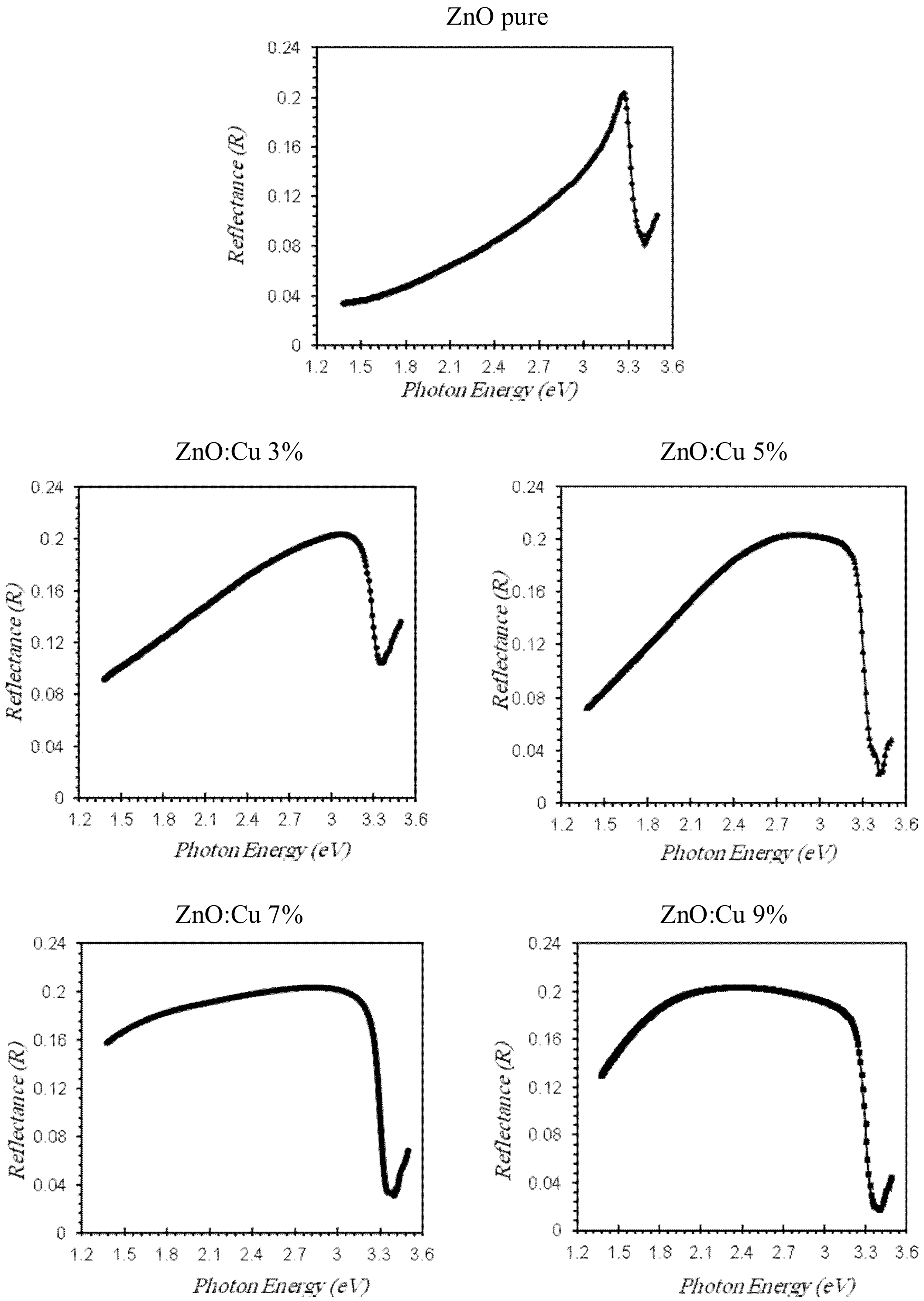

الشكل (7): تغير الانعكاسية كدالة لطاقة الفوتون لأغشية أوكسيد الخارصين النقية والمشوبة ولنسب مختلفة.

الجدول (2): قيم فجوة الطاقة للانتقالين المباشرين المسموح والممنوع لأغشية أوكسيد الخارصين النقية والمشوبة بالنحاس.

الغشاء ونسبة الإشابة	الانتقال المباشر المسموح	الانتقال المباشر الممنوع
	E_g *(eV)*	E_g *(eV)*
ZnO	3.25	3.20
ZnO:Cu (3%)	3.20	3.12
ZnO:Cu (5%)	3.18	3.10
ZnO:Cu (7%)	3.16	3.08
ZnO:Cu(9%)	3.15	3.03

بالاعتماد على طيفي النفاذية transmittance والامتصاصية absorbance، تم حساب الانعكاسية reflectance بموجب قانون حفظ الطاقة من العلاقة الآتية :[20]

$$R + T + A = 1 \qquad (7)$$

إذ تمثل:

R: انعكاسية الغشاء. T: نفاذية الغشـاء.

A: امتصاصية الغشاء.

الشكل (7) يبين تغير الانعكاسية (R) كدالة لطاقة الفوتون (hv) لغشاء أوكسيد الخارصين؛ إذ نلاحظ أن الانعكاسية تكون قليلة عند قيم الطاقات الفوتونية الواطئة ثم تزداد إلى أن تصل إلى قيمة معينة بعدها تبدأ بالانخفاض السريع عند الطاقات الفوتونية العالية. وتفسير ذلك أن الامتصاص يكون قليلاً جداً عند الطاقات الأقل من فجوة الطاقة تقريباً وأن تناقص النفاذية ناتج عن زيادة الانعكاس من سطح الغشاء حسب المعادلة (7)، وعند الطاقات الفوتونية الأعلى من فجوة الطاقة سوف يزداد الامتصاص مما يسبب هبوطاً في الانعكاسية فتتكون عندئذ ذروة (قمة) عند الطاقات المقابلة لقيمة فجوة الطاقة، ونلاحظ أن التشويب وللنسب كافة أدى إلى تغير في موقع قمة منحني الانعكاسية باتجاه الطاقات الفوتونية الواطئة، وهذا بدوره يدل على زيادة الامتصاصية.

وبالاعتماد على معامل الامتصاص المحسوب من العلاقة (4)، تم حساب معامل الخمود باستخدام العلاقة الآتية :[21]

$$K_0 = \frac{\alpha\lambda}{4\pi} \qquad (8)$$

كما يمثل معامل الخمود الجزء الخيالي من معامل الانكسار المعقد (N) بموجب العلاقة الآتية [22,21]

$$N = \frac{C}{V} = n_o - ik_0 \qquad (9)$$

إذ تمثل:

C: سرعة الضوء في الفراغ.

V: سرعة الضوء خلال الغشاء.

n_o: الجزء الحقيقي من معامل الانكسار (معامل الانكسار).

وفي الحقيقة، فإن معامل الخمود extinction coefficient هو مقدار التوهين الحاصل في شدة الأشعة الكهرومغناطيسية [23]، ومن ثم فهو يمثل مقدار الطاقة الممتصة في الغشاء الرقيق. الشكل (8) يبين تغير معامل الخمود كدالة للطول الموجي لغشاء أوكسيد الخارصين النقي؛ إذ نلاحظ أن معامل الخمود يتزايد تدريجيًا بتزايد طاقة الفوتون، ثم تعقب ذلك زيادة سريعة عند الطاقات الفوتونية العالية، وهذا يدل على أن هناك زيادة في الامتصاصية أدت بدورها إلى زيادة معامل الامتصاص حسب العلاقة (4) ومن ثم إلى زيادة معامل الخمود. وعند التشويب نلاحظ أن المنحنيات تسلك بصورة عامة السلوك نفسه المشار إليه أعلاه مع انحراف حافة الامتصاص نحو الطاقات الفوتونية المنخفضة، وهذا يؤكد أن حالة التشويب لها تأثير واضح في زيادة المستويات المانحة ومن ثم في زيادة معامل الخمود.

تم حساب معامل الانكسار في حالة السقوط العمودي وفقاً للعلاقة الآتية [24,21,20].

$$n_o = \left[\left(\frac{1+R}{1-R}\right)^2 - \left(k_o^2 + 1\right)\right]^{\frac{1}{2}} + \frac{1+R}{1-R} \qquad (10)$$

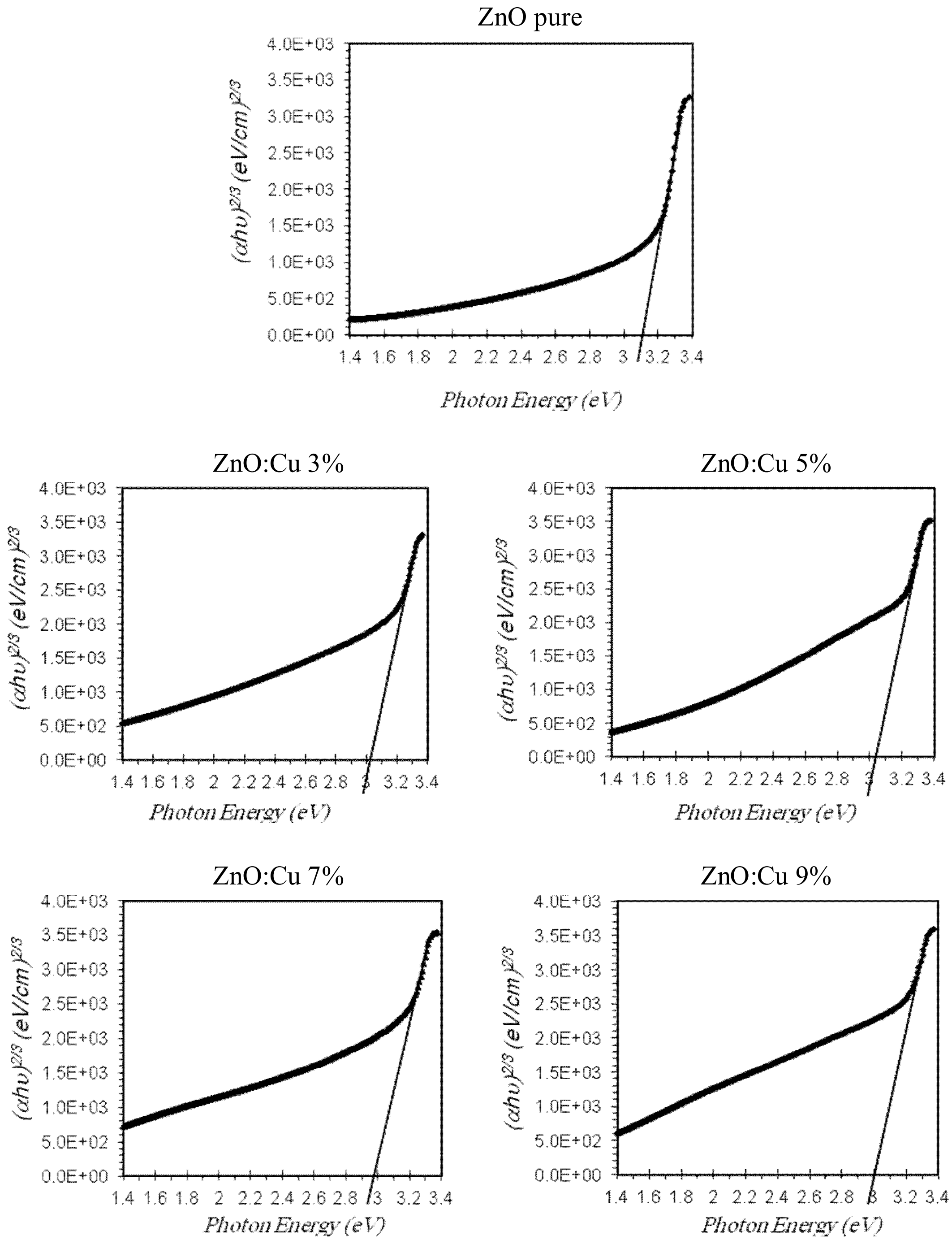
ZnO pure

ZnO:Cu 3%

ZnO:Cu 5%

ZnO:Cu 7%

ZnO:Cu 9%

الشكل (6): فجوة الطاقة للانتقال المباشر الممنوع لأغشية أوكسيد الخارصين النقية والمشوبة ولنسب مختلفة.

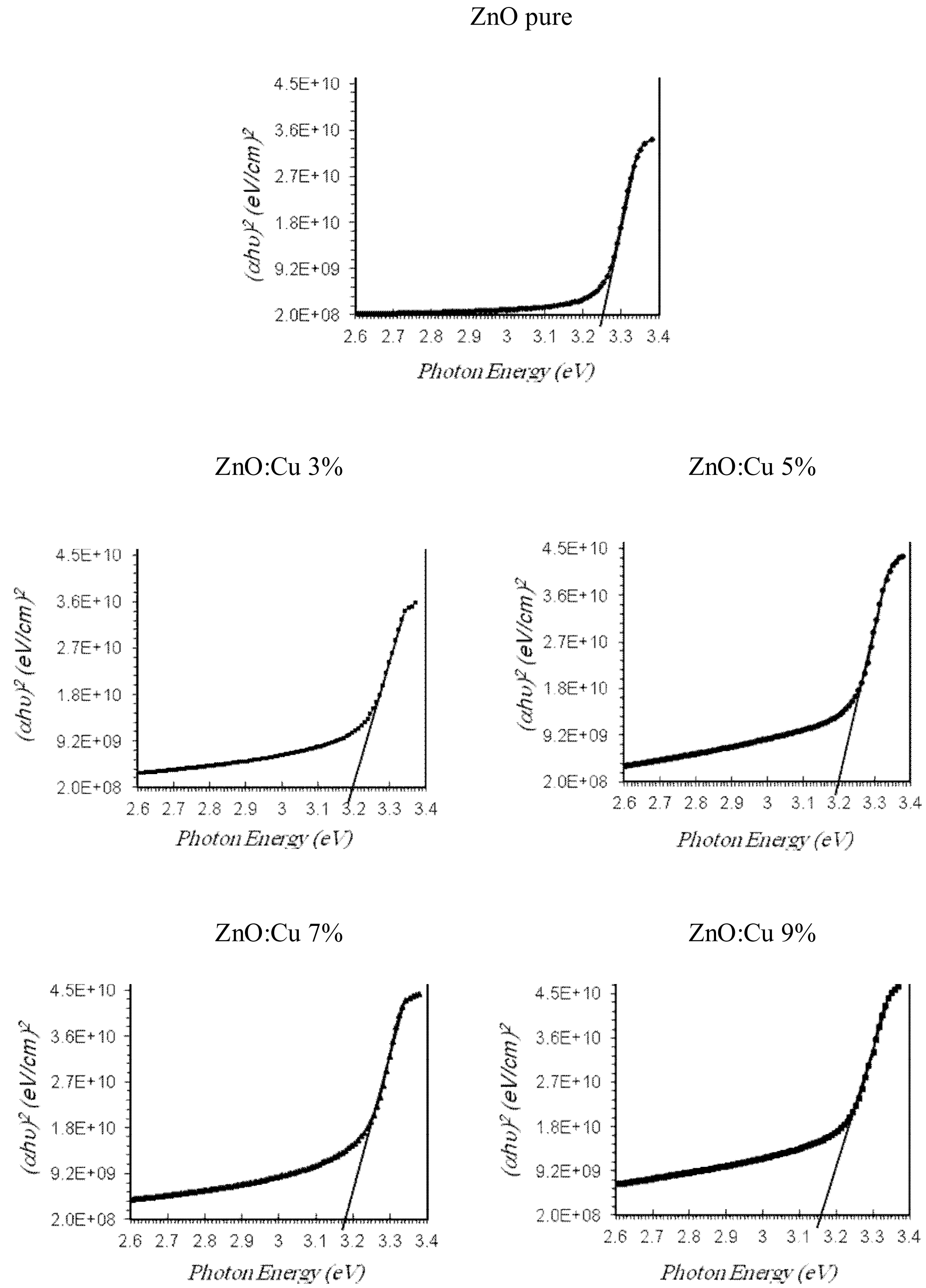

الشكل (5): فجوة الطاقة للانتقال المباشر المسموح لأغشية أوكسيد الخارصين النقية والمشوبة ولنسب مختلفة.

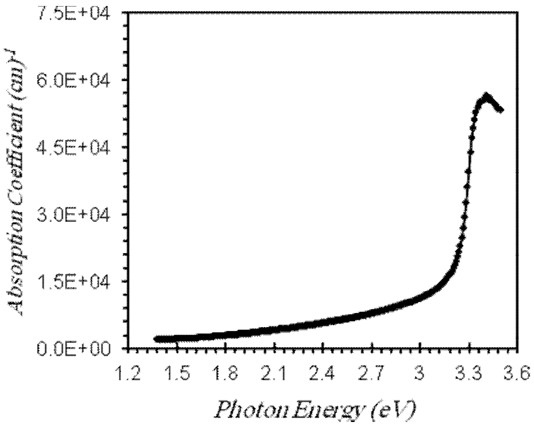

ZnO pure

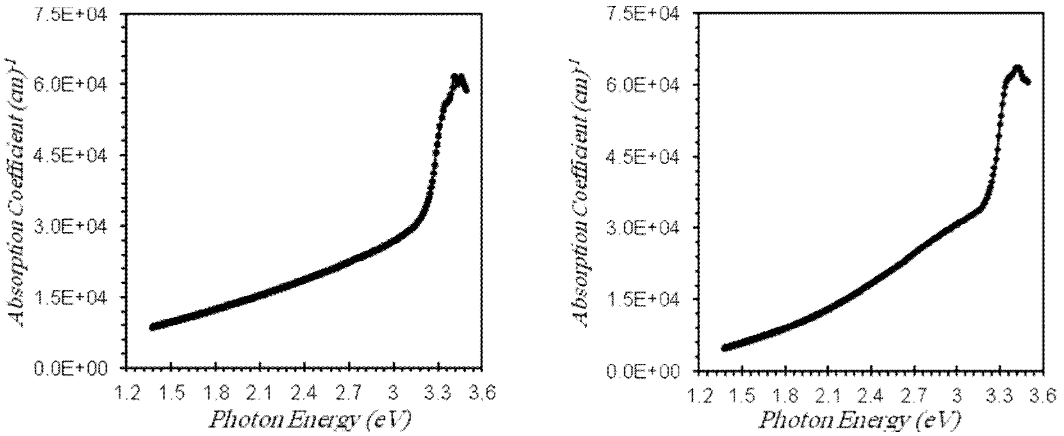

ZnO:Cu 3%

ZnO:Cu 5%

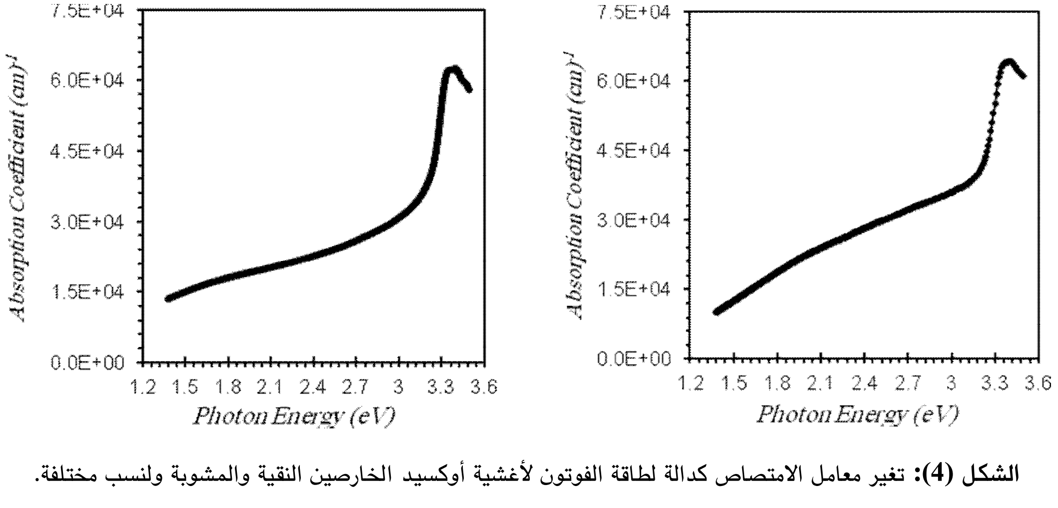

ZnO:Cu 7%

ZnO:Cu 9%

الشكل (4): تغير معامل الامتصاص كدالة لطاقة الفوتون لأغشية أوكسيد الخارصين النقية والمشوبة ولنسب مختلفة.

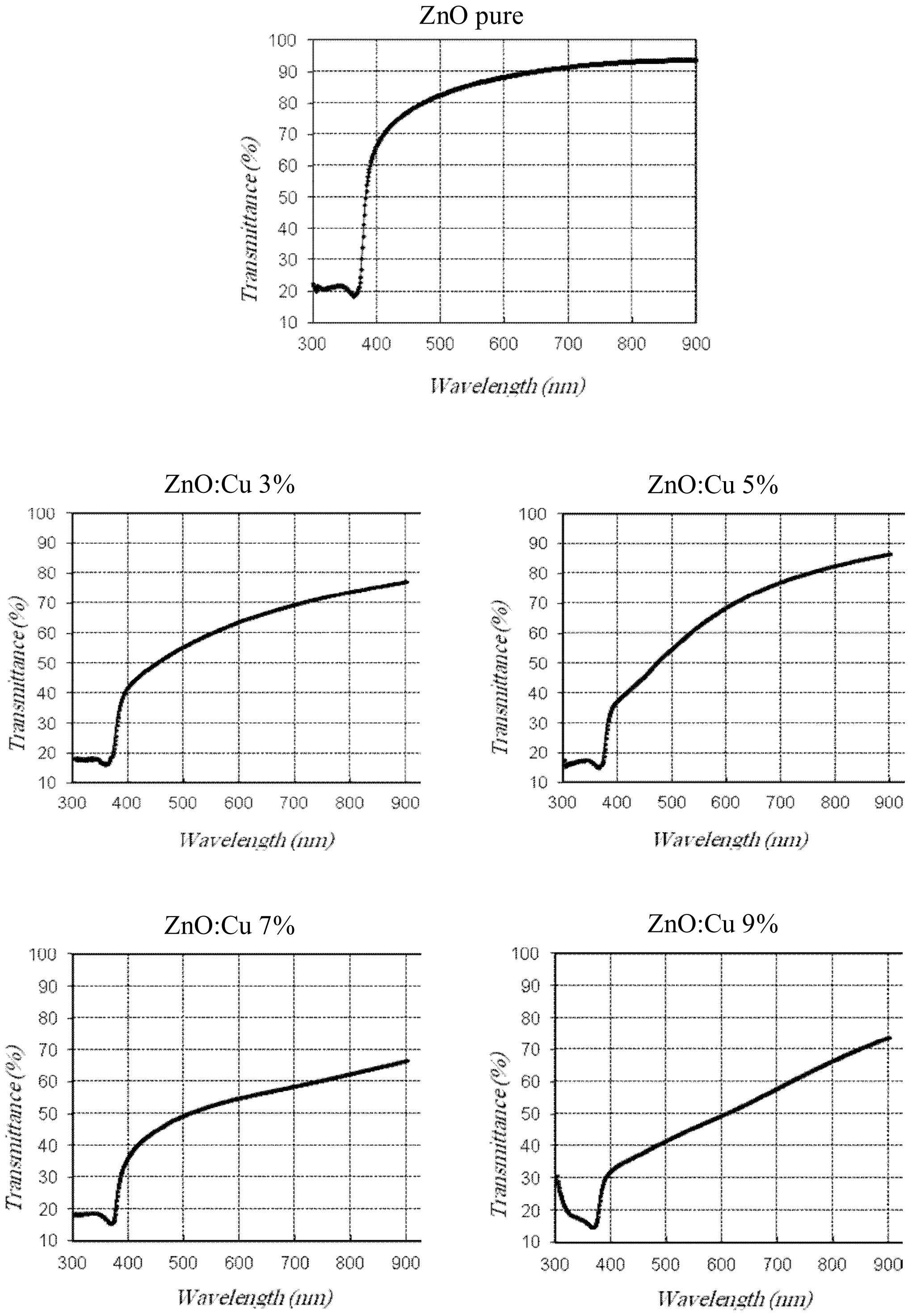

الشكل (3): تغير طيف النفاذية كدالة للطول الموجي لأغشية أوكسيد الخارصين النقية والمشوبة ولنسب مختلفة.

2. الخواص البصرية

بالاعتماد على قيم النفاذية والامتصاصية ضمن مدى الأطوال الموجية (300-900 nm)، رُسمت علاقة النفاذية كدالة للطول الموجي كما في الشكل (3)، وبينت هذه النتائج أن أغشية أوكسيد الخارصين النقية تمتلك نفاذية عالية معدلها حوالي (90%) في منطقة الطيف المرئي والمنطقة تحت الحمراء القريبة مع نفاذية قليلة في المنطقة فوق البنفسجية تزداد بشكل حاد عند قيم الأطوال الموجية (380 – 400 nm)، وتسمى هذه المنطقة بحافة الامتصاص الأساسية، وهذا يدل على أن المادة هي شبه موصل ذو فجوة طاقة واسعة وأن طاقة الفوتونات في المنطقة عالية النفاذية لا تعاني من امتصاص عالٍ، وكذلك فإن لنعومة سطح الغشاء وحجم الحبيبات دورًا في تقليل التشتت [15]، ومع زيادة نسب التشويب نلاحظ أن هناك نقصانًا في قيم النفاذية يقابله زيادة في قيم الامتصاصية وانحراف حافة الامتصاص الأساسية نحو الأطوال الموجية الطويلة (الطاقة الواطئة)، وهذا يبين أن التشويب أدى إلى زيادة المستويات المانحة بالقرب من حزمة التوصيل، وبالتالي فإن إمكانية امتصاص الفوتونات ذات الطاقة المنخفضة واردة جدًا.

تم حساب معامل الامتصاص في منطقة الامتصاص الأساسية باستخدام العلاقة الآتية [16]:

$$\alpha = -\ln (T) / d \qquad (4)$$

إذ تمثل T: نفاذية الغشاء. d: سمك الغشاء.

يوضح الشكل (4) تغير معامل الامتصاص كدالة لطاقة الفوتون لغشاء أوكسيد الخارصين والأغشية المشوبة ولمختلف النسب، ومنه نلاحظ أن معامل الامتصاص كدالة لطاقة الفوتون لغشاء أوكسيد الخارصين النقي يزداد تدريجياً بمقدار صغير بزيادة طاقة الفوتون ولمدى الطاقات ($h\nu < 3eV$) ثم تعقب ذلك زيادة سريعة في المدى (3-3.2eV)، وهذه الزيادة السريعة تساعدنا على التنبؤ بحافة الامتصاص الأساسية، وقد أظهرت النتائج أن زيادة نسب التشويب أدت إلى زيادة واضحة في جميع قيم معامل الامتصاص، وخاصة عند الطاقات المنخفضة، وهذا يبدو واضحاً من الشكل (4)؛ إذ زحفت حافة الامتصاص الأساسية باتجاه الطاقات الفوتونية المنخفضة.

نلاحظ كذلك أن معامل الامتصاص لجميع الحالات سواء في الأغشية النقية أو المشوبة يمتلك قيمًا أكبر من ($10^4\ cm^{-1}$) في مدى الطاقات العالية مما يدل على حدوث انتقالات إلكترونية مباشرة، وهذا يتفق مع المصدر [17].

تبين من الدراسة الحالية حدوث نوعين من الانتقالات الإلكترونية، وهي الانتقالات الإلكترونية المباشرة المسموحة والممنوعة التي بموجبها أمكن حساب قيمة فجوة الطاقة على النحو الآتي:

<u>أولاً</u>: حساب قيمة فجوة الطاقة البصرية optical band gap في حالة الانتقالات المباشرة المسموحة، أي فجوة الطاقة الواقعة بين قمة حزمة التكافؤ وقعر حزمة التوصيل عند المتجه الموجي (K = 0) وباستخدام العلاقة الآتية [18]:

$$(\alpha h\nu)^2 = B^2 (h\nu - E_g) \qquad (5)$$

الشكل (5) يمثل المنحني المرسوم بين $(\alpha h\nu)^2$ وطاقة الفوتون لأغشية أوكسيد الخارصين والأغشية المشوبة. وبمد الجزء المستقيم من المنحني ليقطع محور طاقة الفوتون عند النقطة ($(\alpha h\nu)^2 = 0$) نحصل على قيمة فجوة الطاقة البصرية للانتقال المباشر المسموح، ونلاحظ أن قيم (E_{opt}) تقل بزيادة نسب الشوائب لجميع الأغشية كما هو موضح في الجدول (2)، وهذا يعني أن التشويب أدى إلى إزاحة حافة الامتصاص نحو الطاقات المنخفضة، وهذا النقصان يمكن تفسيره بأن الشوائب أدت إلى تكوّن مستويات مانحة كما بينا سابقًا داخل فجوة الطاقة وبالقرب من حزمة التوصيل عملت بدورها على إزاحة مستوى فيرمي نحو حزمة التوصيل ومن ثم امتصاص الفوتونات ذات الطاقة الأقل من (3.25eV) حتى (3.15eV).

<u>ثانياً</u>: حساب قيمة فجوة الطاقة في حالة الانتقالات المباشرة الممنوعة باستخدام العلاقة الآتية [19]:

$$(\alpha h\nu)^{2/3} = B^{2/3} (h\nu - E_g) \qquad (6)$$

وبرسم العلاقة بين $(\alpha h\nu)^{2/3}$ وطاقة الفوتون ومد الجزء المستقيم من المنحني ليقطع محور طاقة الفوتون عند النقطة ($(\alpha h\nu)^{2/3} = 0$) نحصل على قيمة فجوة الطاقة البصرية لأغشية أوكسيد الخارصين النقية والمشوبة. الشكل (6) يمثل المنحني المرسوم بين $(\alpha h\nu)^{2/3}$ وطاقة الفوتون لهذه الأغشية؛ إذ نلاحظ نقصان قيم (E_g) بزيادة نسب التشويب لجميع الأغشية وللسبب السابق نفسه في حالة الانتقالات المباشرة المسموحة، كما في الجدول (2).

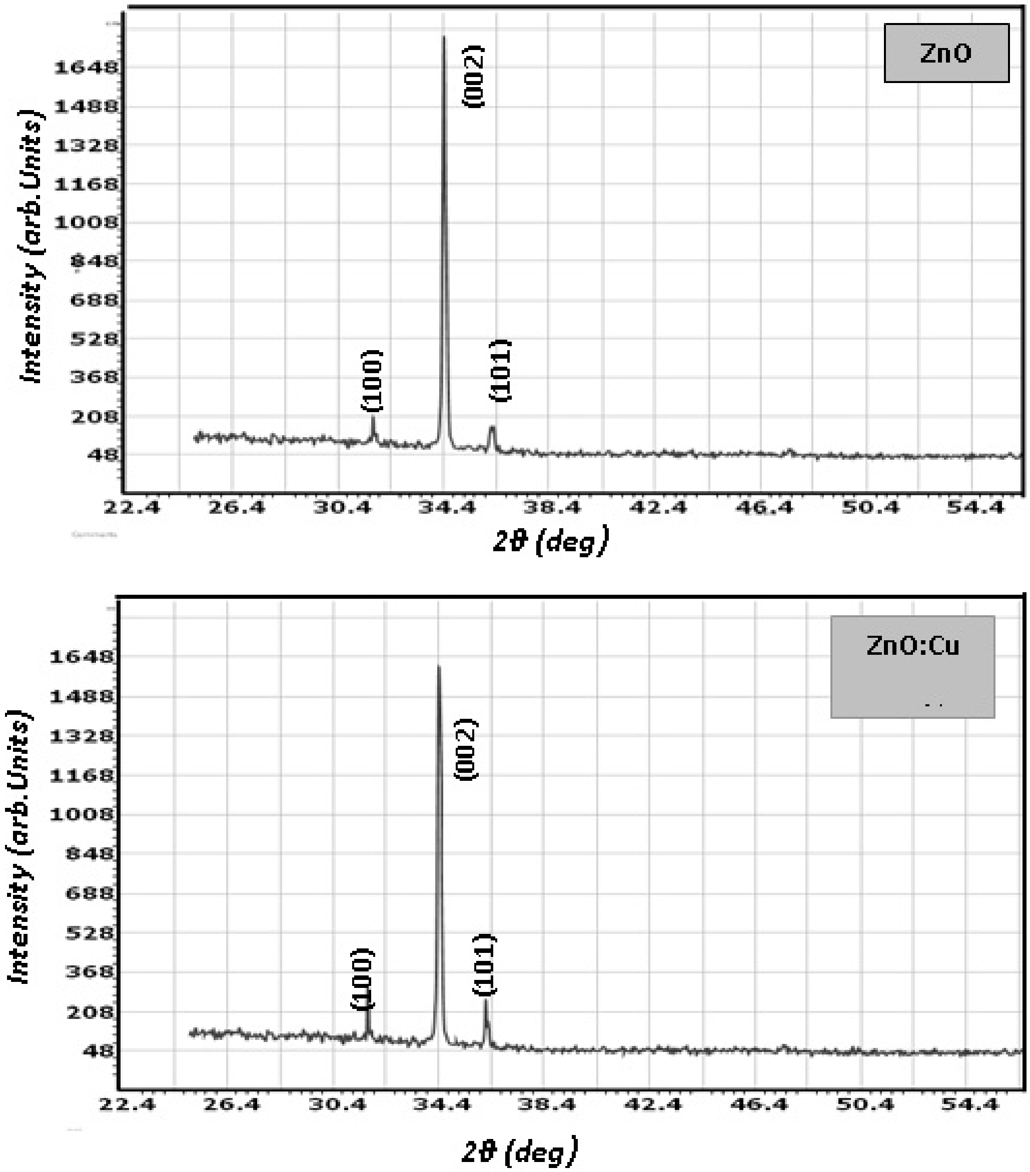

الشكل (2): مخطط حيود الأشعة السينية لأغشية أوكسيد الخارصين النقية والمشوبة بالنحاس.

الجدول (1): نتائج حيود الأشعة السينية لأغشية ZnO النقية والمشوبة بالنحاس.

	Undoped ZnO (002)	***ZnO:Cu at 9% (002)***	***JCPDS for ZnO (002)***
2θ	34.452	34.481	34.422
d(Å)	2.6011	2.599	2.6033
d % error	0.084	0.080	_____
a_o(Å)	3.2470	3.2440	3.2498
c_o (Å)	5.2022	5.1980	5.2066
Grain size (nm)	60.44	45.96	_____

أما في حالة التطعيم بالنحاس، فقد استخدمنا المعادلة:

$$t = \frac{m_2 - m_1}{A \cdot \rho_{total}}$$

إذ إن ρ_{total} = كثافة ZnO × نسبته في المركب + كثافة Cu × نسبته في المركب.

القياسات البصرية والتركيبية

اشتملت القياسات البصرية على طيفي الامتصاصية (Absorbance) والنفاذية (Transmittance) لمدى الأطوال الموجية (300-900nm)، وذلك باستخدام جهاز من نوع (UV-1650PC) ذي الحزمتين المجهز من شركة (SHIMADZU)، وهو جهاز ذو دقة عالية (0.1 nm)، أما القياسات التركيبية فقد أُجريت باستخدام جهاز من نوع (SHIMADZU) أيضًا ذي هدف من نوع (Cu kα) وبطول موجي (1.5406 Å).

النتائج والمناقشة

1. الخواص التركيبية

إن لتأثير الشائبة داخل البنية البلورية الدور الكبير في تغيير أكثر الخصائص الفيزيائية لأنها يمكن أن تؤثر في أبسط الحالات على حجم البلورة وبالتالي في المسافة بين السطوح البلورية، مما يتسبب بدوره بإزاحة مواقع القمم في محور زاوية الحيود (2θ) ضمن منحني حيود الأشعة السينية إلى قيم اكبر أو أقل اعتمادًا على القطر الأيوني لذرات المادة الشائبة عند مقارنتها مع المادة المضيفة (Host) في الشبيكة [8]، ومن المعروف أيضًا أن التأثير الفعال للتشويب يحصل عندما تكون ذرات المادة الشائبة أصغر من أو مساوية للقطر الأيوني للمادة المضيفة [9]. في بحثنا الحالي أظهرت النتائج أن أغشية أوكسيد الخارصين النقية والمشوبة بالنسبة (9%) ذات تركيب متعدد التبلور (Polycrystalline) من النوع السداسي (Hexagonal) ضمن الاتجاهية (100)، (002)، (101)، مع نمو متميز بالاتجاهية (002) وهذا يتفق مع البحوث [11,10]، ونلاحظ أن زاوية الحيود ازدادت مع زيادة التشويب، وسبب ذلك أن القطر الأيوني للنحاس أصغر من القطر الأيوني للخارصين [12] وهما (Zn^{+2} = 0.74 Å) و(Cu^{+2} = 0.69 Å) كما في الشكل (2)، وبذلك فان إمكانية أن يحل أيون النحاس محل أيون الخارصين واردة جدًا مما يؤدي إلى نقصان حجم البلورة الذي سيؤدي إلى نقصان المسافة بين المستويات البلورية (d) ومن ثم إلى زيادة (2θ) لأن العلاقة بينهما عكسية حسب قانون براغ Bragg's Law ($n\lambda = 2d \sin\theta$)، وكذلك يقودنا الاستنتاج الحالي إلى أن ذرات المادة الشائبة ضمن الشبيكة الحالية يمكنها أن تتآصر بسهولة مع الأوكسجين المتوفر بنسبة عالية لتكوّن أوكسيد النحاس الأحادي (CuO) بأكثر الأحوال رغم أننا لم نلاحظ وجود هذا الطور في طيف الحيود، وهذا يعزى إلى نسب التشويب القليلة [9,7]، ويمكن أن يظهر هذا الطور واضحًا عند النسب العالية، كذلك تبين أن هناك زيادة طفيفة في قمم (100)، (101) مما يدل على تحسن التبلور بهذا الاتجاه. الجدول (1) يبين بعض النتائج المحسوبة عن طريق طيف الحيود، وكانت ذات تطابق جيد مع القيم القياسية ضمن نموذج (JCPDS file no. 36-1451)، وقد تم حساب ثوابت الشبيكة (a_o) و(c_o) باستخدام العلاقة الآتية [13]:

$$\frac{1}{d^2} = \frac{4}{3}\left(\frac{h^2 + hk + k^2}{a_o^2}\right) + \frac{l^2}{c_o^2} \qquad (1)$$

إذ إن: (h,k,l) تمثل معاملات ميلر Miller indices.

وكذلك تم حساب معدل الحجم الحبيبي من علاقة شيرر Scherer [7، 13]:

$$D_{av} = \frac{0.9\lambda}{B\cos\theta} \qquad (2)$$

إذ إن:

λ: الطول الموجي المستخدم في جهاز الأشعة السينية.

B: قيمة FWHM.

تم حساب نسبة الخطأ المئوية باستخدام العلاقة التالية [14]:

$$\text{Relative percentage error} = \frac{|Z_H - Z|}{Z} \times 100 \qquad (3)$$

إذ إن:

Z_H: قيمة d المحسوبة من الطيف.

Z: قيمة d ضمن بطاقة JCPDS.

السنين الأخيرة أمكن تحضير أغشية أوكسيد الخارصين كقضبان متناهية الصغر (Nanorods) ذات تطبيقات حديثة [26,5]. يمكن تحضير أغشية أوكسيد الخارصين بعدة طرق منها طريقة الترسيب البخاري الكيميائي (CVD)، وطريقة التحلل الكيميائي الحراري (Chemical Spray Pyrolysis)، والتبخير الحراري (Thermal Evaporation)، والترذيذ (Sputtering) وغيرها [2]. إن الأغشية التي يتم الحصول عليها بطريقة (APCVD) تكون ملائمة للدراسات العلمية والتطبيقات التكنولوجية، وتُعد هذه الطريقة من الطرائق الاقتصادية ومن أمثلها للحصول على أغشية المركبات العضوية.

يهدف البحث الحالي إلى دراسة خواص أوكسيد الخارصين البصرية والتركيبية، ومعرفة تأثير التشويب بالنحاس بنسب (3-9 wt%) على هذه الخواص، وذلك سعيًا للحصول على غشاء بمواصفات جيدة، وتحسين صفاته الفيزيائية في منطقة الطيف المرئي.

الجانب العملي

لأجل الحصول على المادة الأساسية في تحضير أغشية أوكسيد الخارصين النقية تم استخدام مادة خلات الخارصين المائية ($Zn[CH_3COO]_2.2H_2O$) بعد إضافة الماء المقطر إليها وبالتالي الحصول على محلول مائي ذي تركيز (1M)، وبإضافة نسب وزنية (3-9 %) من مادة نترات النحاس المائية ($Cu(No_3)_2.3H_2O$) تم الحصول على المحلول المائي الخاص بتحضير الأغشية المشوبة وبنفس التركيز المولاري أعلاه، وبعد إعداد المحلول تُرك لفترة زمنية مناسبة للتأكد من عدم وجود أية رواسب ومن ثم وضِع في الوحدة الخاصة بالتبخير في منظومة (APCVD)؛ إذ إن وجود مادة التبخير كسائل (Liquid) هي طريقة متداولة في كثير من البحوث المنشورة [7,6]. فبعد أن يصل المحلول إلى مرحلة الغليان يبدأ بخار الماء بالتصاعد حيث يُطرح خارجاً عبر صمام مُعد لهذا الغرض كما في الشكل (1)، ومن ثم يُفتح الصمام الخاص بإيصال المادة المتبخرة إلى حجرة الترسيب.

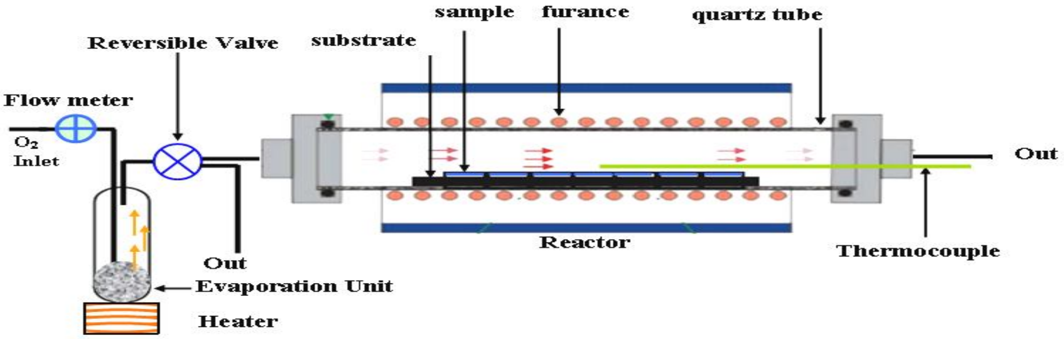

الشكل (1): مخطط توضيحي لمنظومة APCVD.

إن عملية الترسيب في منظومة (APCVD) ذات الجدار الساخن (Hot Wall) المصنعة محليًا والحصول على أغشية بمواصفات جيدة تطلبت وجود عدة مراحل، في بدايتها عملية تنظيف العينات الزجاجية ذات الأبعاد (2 X 2.5cm)؛ إذ وضِعت في محلول تراي كلورو إثيلين (TCE) ضمن جهاز الأمواج فوق الصوتية ولفترة (10 دقائق)، ثم محلول الأسيتون، وبعدها محلول الميثانول للفترة الزمنية نفسها بعد ذلك تم غسلها بالماء اللاأيوني وتجفيفها بواسطة الهواء الحار. اما ظروف الترسيب فهي على النحو الآتي:

1. درجة حرارة القاعدة 500 ^{o}C.
2. معدل تدفق الهواء 1.5 L/min.
3. زمن الترسيب 20 min.

إن الأغشية التي تم الحصول عليها كانت شديدة الالتصاق بالقاعدة، ذات تجانس جيد وخالية من التشققات وذات سماكات مختلفة تعتمد على موقع النموذج داخل حجرة الترسيب، وفي بحثنا الحالي كان سمك الغشاء المستخدم (3000 Å). فقد تم إيجاده باستخدام الطريقة الوزنية حسب المعادلة:

$$t=\frac{m_2-m_1}{A\cdot\rho_{zno}}$$

إذ إن ($m_2 - m_1$) يمثل الفرق بين وزن الأرضيات قبل ترسيب الغشاء وبعده؛

ρ_{zno} كثافة المادة؛ و t سمك الغشاء.

المجلد 5، العدد 2، 2012. ص ص. 89-103

المجلة الأردنية للفيزياء

ARTICLE

دراسة الخواص التركيبية والبصرية لأغشية (ZnO:Cu) المحضرة بطريقة APCVD

ميخائيل عيسى منصور

قسم الفيزياء، كلية التربية، جامعة الموصل، الموصل، العراق.

Received on: 11/10/2011; Accepted on: 22/4/2012

الملخص: في هذه الدراسة تم تحضير أغشية ZnO النقية والمطعمة بالنحاس بنسبة (3-9 %) باستخدام تقنية الترسيب البخاري الكيميائي عند الضغط الجوي الاعتيادي (APCVD) وعلى قواعد من الزجاج بدرجة حرارة أساس (500ºC)، تمت دراسة الخواص التركيبية والبصرية لهذه الأغشية. بينت نتائج التشخيص أن هذه الأغشية متعددة التبلور وذات تركيب سداسي مع اتجاه تفضيلي عند (002)، وتضمنت دراسة الخواص البصرية (طيف النفاذية، فجوة الطاقة، معامل الامتصاص، الانعكاسية، معامل الانكسار، معامل الخمود)، ووجد أن قيم فجوة الطاقة تتناقص من (3.25 – 3.15 eV)، وأن معدل النفاذية (90 %) ضمن منطقة الطيف المرئي.

Studying the Structural and Optical Properties of ZnO:Cu Prepared by APCVD Technique

Mekhaiel Manssor

Physics Department, College of Education, Mosul University, Iraq.

Abstract: Undoped and Cu-doped ZnO at (3-9 wt. %) thin films have been prepared by APCVD technique on glass substrates at 500ºC. The structural and optical properties of these films were studied. The results of the structural tests showed that these films are of a polycrystalline hexagonal structure with a preferred orientation in the (002) direction, the optical properties included transmittance, energy gap, absorption coefficient, reflectance, refractive index and extinction coefficient, the energy gap values were found to decrease from (3.25 to 3.15 eV) and the average transmittance was found about (90%) in the visible region.

Keywords: TCO; ZnO; APCVD; Optical properties.
PACS: 60:70

المقدمة

أوكسيد الخارصين أحد مركبات الخارصين الكيميائية، ذو تركيب بلوري سداسي (Hexagonal) من نوع (Wurtzite)، ويُعد أحد أشباه الموصلات واسعة الاستخدام لكونه يمتاز بفجوة طاقة مباشرة (3.37eV) عند درجة حرارة الغرفة وطاقة ربط عالية للإكسيتون (Exciton) قيمتها (60meV)، ينتمي إلى المجاميع (II-VI) في الجدول الدوري ومن النوع السالب (n-type)، ذو توصيلية عالية ناتجة من وجود فراغات الأوكسجين (Oxygen Vacancies)، وبذلك فهو مشابه في خواصه البصرية إلى حد كبير لمادة GaN [3-1]. ونظراً لنفاذيته العالية (High Transparency) في المنطقة المرئية والمنطقة تحت الحمراء القريبة فقد صُنف ضمن أكاسيد التوصيل الشفافة (Transparent Conducting Oxides) ذات التطبيقات الواسعة في النبائط الكهروبصرية، مثل الخلايا الشمسية، وشاشات العرض السائلة، والمتحسسات الغازية والكيميائية، ودايودات الانبعاث الضوئي [4]، وفي

Corresponding Author: Mekhaiel Manssor **Email**: mekhaiel53@yahoo.com

Authors Index

Subject Index

طرائق البحث (التجريبية / النظرية): يجب أن تكون هذه الطرائق موضحة بتفصيل كاف لإتاحة إعادة إجرائها بكفاءة، ولكن باختصار مناسب، حتى لا تكون تكرارا للطرائق المنشورة سابقا.

النتائج: يستحسن عرض النتائج على صورة جداول وأشكال حيثما أمكن، مع شرح قليل في النص ومن دون مناقشة تفصيلية.

المناقشة: يجب أن تكون موجزة وتركز على تفسير النتائج.

الاستنتاج: يجب أن يكون وصفا موجزا لأهم ما توصلت إليه الدراسة ولا يزيد عن صفحة مطبوعة واحدة.

الشكر والعرفان: الشكر والإشارة إلى مصدر المنح والدعم المالي يكتبان في فقرة واحدة تسبق المراجع مباشرة.

المراجع: يجب طباعة المراجع بأسطر مزدوجة ومرقمة حسب تسلسلها في النص. وتكتب المراجع في النص بين قوسين مربعين. ويتم اعتماد اختصارات الدوريات حسب نظام Wordlist of Scientific Reviewers.

الجداول: تعطى الجداول أرقاما متسلسلة يشار إليها في النص. ويجب طباعة كل جدول على صفحة منفصلة مع عنوان فوق الجدول. أما الحواشي التفسيرية، التي يشار إليها بحرف فوقي، فتكتب أسفل الجدول.

الرسوم التوضيحية: يتم ترقيم الأشكال والرسومات والرسومات البيانية (المخططات) والصور، بصورة متسلسلة كما وردت في النص.

تقبل الرسوم التوضيحية المستخرجة من الحاسوب والصور الرقمية ذات النوعية الجيدة بالأبيض والأسود، على ان تكون أصيلة وليست نسخة عنها، وكل منها على ورقة منفصلة ومعرفة برقمها بالمقابل. ويجب تزويد المجلة بالرسومات بحجمها الأصلي بحيث لا تحتاج إلى معالجة لاحقة، وألا تقل الحروف عن الحجم 8 من نوع Times New Roman، وألا تقل سماكة الخطوط عن 0.5 وبكثافة متجانسة. ويجب إزالة جميع الألوان من الرسومات ما عدا تلك التي ستنشر ملونة. وفي حالة إرسال الرسومات بصورة رقمية، يجب أن تتوافق مع متطلبات الحد الأدنى من التمايز (1200 dpi Resolution) لرسومات الأبيض والأسود الخطية، و 600 dpi للرسومات باللون الرمادي، و300 dpi للرسومات الملونة. ويجب تخزين جميع ملفات الرسومات على شكل (jpg)، وأن ترسل الرسوم التوضيحية بالحجم الفعلي الذي سيظهر في المجلة. وسواء أرسل المخطوط بالبريد أو عن طريق الشبكة (Online)، يجب أرسال نسخة ورقية أصلية ذات نوعية جيدة للرسومات التوضيحية.

مواد إضافية: تشجع المجلة الباحثين على إرفاق جميع المواد الإضافية التي يمكن أن تسهل عملية التحكيم. وتشمل المواد الإضافية أي اشتقاقات رياضية مفصلة لا تظهر في المخطوط.

المخطوط المنقح (المعدَل) والأقراص المدمجة: بعد قبول البحث للنشر وإجراء جميع التعديلات المطلوبة، فعلى الباحثين تقديم نسخة أصلية ونسخة أخرى مطابقة للأصلية مطبوعة بأسطر مزدوجة، وكذلك تقديم نسخة إلكترونية تحتوي على المخطوط كاملا مكتوبا على Microsoft Word for Windows 2000 أو ما هو استجد منه. ويجب إرفاق الأشكال الأصلية مع المخطوط النهائي المعدل حتى لو تم تقديم الأشكال إلكترونيا. وتخزن جميع ملفات الرسومات على شكل (jpg)، وتقدم جميع الرسومات التوضيحية بالحجم الحقيقي الذي ستظهر به في المجلة. ويجب إرفاق قائمة ببرامج الحاسوب التي استعملت في كتابة النص، وأسماء الملفات على قرص مدمج، حيث يعلَم القرص بالاسم الأخير للباحث، وبالرقم المرجعي للمخطوط للمراسلة، وعنوان المقالة، والتاريخ. ويحفظ في مغلف واقٍ.

الفهرسة: تقوم المجلة الأردنية للفيزياء بالإجراءات اللازمة لفهرستها وتلخيصها في جميع الخدمات الدولية المعنية.

حقوق الطبع

يُشكِّل تقديم مخطوط البحث للمجلة اعترافاً صريحاً من الباحثين بأنَ مخطوط البحث لم يُنْشَر ولم يُقَدَّم للنشر لدى أي جهَة أخرى كانت وبأي صيغة ورقية أو إلكترونية أو غيرها. ويُشترط على الباحثين ملء أنموذجٍ يَنُصُ على نقْل حقوق الطبع لتُصبح ملكاً لجامعة اليرموك قبل الموافقة على نشر المخطوط. ويقوم رئيس التحرير بتزويد الباحثين بإنموذج نقل حقوق الطبع مع النسخة المُرْسَلَة للتنقيح. كما ويُمنع إعادة إنتاج أيِّ جزء من الأعمال المنشورة في المجلّة من دون إذن خَطِّيٍّ مُسْبَق من رئيس التحرير.

إخلاء المسؤولية

إن ما ورد في هذه المجلة يعبر عن آراء المؤلفين، ولا يعكس بالضرورة آراء هيئة التحرير أو الجامعة أو سياسة اللجنة العليا للبحث العلمي أو وزارة التعليم العالي والبحث العلمي. ولا يتحمل ناشر المجلة أي تبعات مادية أو معنوية أو مسؤوليات عن استعمال المعلومات المنشورة في المجلة أو سوء استعمالها.

معلومات عامة

المجلة الأردنية للفيزياء هي مجلة بحوث علميّة عالمية مُحكمة تصدر عن اللجنة العليا للبحث العلمي، وزارة التعليم العالي والبحث العلمي، عمان، الأردن. وتقوم بنشر المجلة عمادة البحث العلمي والدراسات العليا في جامعة اليرموك، إربد، الأردن. وتنشر البحوث العلمية الأصيلة، إضافة إلى المراسلات القصيرة Short Communications، والملاحظات الفنية Technical Notes، والمقالات الخاصّة Feature Articles، ومقالات المراجعة Review Articles، في مجالات الفيزياء النظرية والتجريبية، باللغتين العربية والإنجليزية.

تقديم مخطوط البحث

تُرسَل نسخة أصلية وثلاث نسخٍ من المخطوط، مُرْفَقَةً برسالة تغطية من جانب الباحث المسؤول عن المراسلات، إلى رئيس التحرير:

أ.د. ابراهيم أبو الجرايش،
رئيس التحرير، المجلة الأردنية للفيزياء،
عمادة البحث العلمي والدراسات العليا،
جامعة اليرموك، إربد، الأردن.
هاتف : 111 11 72 2 962 00 / فرعي: 2075
فاكس : 121 11 72 2 962 00
بريد إلكتروني : jjp@yu.edu.jo

تقديم المخطوطات إلكترونيًا: اتبع التعليمات في موقع المجلة على الشبكة العنكبوتية.

ويجري تحكيمُ البحوثِ الأصيلة والمراسلات القصيرة والملاحظات الفنية من جانب مُحكِّمين اثنين في الأقل من ذوي الاختصاص والخبرة. وتُشَجِّع المجلة الباحثين على اقتراح أسماء المحكمين. أما نشر المقالات الخاصّة في المجالات الفيزيائية النَشِطَة، فيتم بدعوة من هيئة التحرير، ويُشار إليها كذلك عند النشر. ويُطلَب من كاتب المقال الخاص تقديم تقرير واضح يتّسم بالدقة والإيجاز عن مجال البحث تمهيداً للمقال. وتنشر المجلةُ أيضاً مقالات المراجعة في الحقول الفيزيائية النشطة سريعة التغيُّر، وتُشَجَّع كاتبي مقالات المراجعة أو مُستَكتبيها على إرسال مقترحٍ من صفحتين إلى رئيس التحرير. ويُرْفَق مع البحث المكتوب باللغة العربية ملخص (Abstract) وكلمات دالة (Keywords) باللغة الإنجليزية.

ترتيب مخطوط البحث

يجب أن تتم طباعة مخطوط البحث ببنط 12 نوعه Times New Roman، وبسطر مزدوج، على وجه واحد من ورق A4 (21.6 × 27.9 سم) مع حواشي 3.71 سم ، باستخدام معالج كلمات ميكروسوفت وورد 2000 أو ما اسْتَجَد منه. ويجري تنظيم أجزاء المخطوط وفق الترتيب التالي: صفحة العنوان، الملخص، رموز التصنيف (PACS)، المقدّمة، طرق البحث، النتائج، المناقشة، الخلاصة، الشكر والعرفان، المراجع، الجداول، قائمة بدليل الأشكال والصور والإيضاحات، ثَمَّ الأشكال والصور والإيضاحات. وتُكْتَب العناوين الرئيسة بخطٍّ **غامق**، بينما تُكْتَب العناوين الفرعية بخطٍّ *مائل*.

صفحة العنوان: وتشمل عنوان المقالة، أسماء الباحثين الكاملة وعناوين العمل كاملة. ويكتب الباحث المسؤول عن المراسلات اسمه مشارا إليه بنجمة، والبريد الإلكتروني الخاص به. ويجب أن يكون عنوان المقالة موجزا وواضحا ومعبرا عن فحوى (محتوى) المخطوط، وذلك لأهمية هذا العنوان لأغراض استرجاع المعلومات.

الملخص: المطلوب كتابة فقرة واحدة لا تزيد على مائتي كلمة، موضحة هدف البحث، والمنهج المتبع فيه والنتائج وأهم ما توصل إليه الباحثون.

الكلمات الدالة: يجب أن يلي الملخص قائمة من 4-6 كلمات دالة تعبر عن المحتوى الدقيق للمخطوط لأغراض الفهرسة.

PACS: يجب إرفاق الرموز التصنيفية، وهي متوافرة في الموقع http://www.aip.org/pacs/pacs06/pacs06-toc.html.

المقدمة: يجب أن توضّح الهدف من الدراسة وعلاقتها بالأعمال السابقة في المجال، لا أن تكون مراجعة مكثفة لما نشر (لا تزيد المقدمة عن صفحة ونصف الصفحة مطبوعة).

Subscription Form

Jordan Journal of

PHYSICS

An International Peer-Reviewed Research Journal

Published by the Deanship of Research & Graduate Studies, Yarmouk University, Irbid, Jordan

Name: .... :الأسم
Specialty:...:التخصص
Address: ....:العنوان
P.O. Box:... : صندوق البريد
City & Postal Code: ....:المدينة/الرمز البريدي
Country: .... :القطر
Phone: ....:رقم الهاتف
Fax No:.. :رقم الفاكس
E-mail:.. :البريد الإلكتروني
No. of Subscription: .... :عدد الإشتراكات
Method of Payment:.. :طريقة الدفع
Amount Enclosed:... :المبلغ المرفق
Signature: ....:التوقيع
Cheques should be paid to Deanship of Research and Graduate Studies - Yarmouk University.

I would like to subscribe to the Journal
For

- ☐ One Year
- ☐ Two Years
- ☐ Three Years

One Year Subscription Rates

	Inside Jordan	Outside Jordan
Individuals	JD 8	€ 40
Students	JD 4	€ 20
Institutions	JD 12	€ 60

Correspondence

Subscriptions and Sales:

Prof. Ibrahim O. Abu-AlJarayesh
Deanship of Research and Graduate Studies
Yarmouk University
Irbid – Jordan
Telephone: 00 962 2 711111 Ext. 2075
Fax No.: 00 962 2 7211121

المملكة الأردنية الهاشمية

جامعة اليرموك

المجلة الأردنية
للفيزياء

مجلة بحوث علمية عالمية محكّمة

المجلد (5)، العدد (2)، 2012م / 1433هـ

المجلة الأردنية

للفيزياء

مجلة بحوث علمية عالمية محكّمة

المجلد (5)، العدد (2)، 2012م / 1433هـ

المجلة الأردنية للفيزياء: مجلة بحوث علمية عالمية محكّمة أسستها اللجنة العليا للبحث العلمي، وزارة التعليم العالي والبحث العلمي، الأردن، وتصدر عن عمادة البحث العلمي والدراسات العليا، جامعة اليرموك، إربد، الأردن.

ترسل البحوث إلى العنوان التالي:

الأستاذ الدكتور إبراهيم عثمان أبو الجرايش
رئيس تحرير المجلة الأردنية للفيزياء
عمادة البحث العلمي والدراسات العليا، جامعة اليرموك
إربد ، الأردن
هاتف 00 962 2 7211111 **فرعي** 2075
E-mail: *jjp@yu.edu.jo*
Website: *http://Journals.yu.edu.jo/jjp*